11-10-2016 12:00 AM

Middle-Ear Imaging and Estimation of The Linear Elastic Properties of The Human Tympanic Membrane

Seyed Alireza Rohani
The University of Western Ontario

Supervisor
Dr. Hanif Ladak
The University of Western Ontario

Graduate Program in Biomedical Engineering
A thesis submitted in partial fulfillment of the requirements for the degree in Doctor of Philosophy

Abstract

Finite-element (FE) modeling of the human middle ear could improve diagnostic techniques, such as tympanometry. Accurate representation of the mechanical properties and geometry of the middle ear, especially of the soft tissues, are crucial for FE modeling of the middle ear. The objective of this work is to quantitatively evaluate the efficacy of iodine potassium iodide (IKI) solution as a contrast agent for imaging the middle-ear soft tissues and to estimate the linear elastic properties of the human tympanic membrane (TM).

In the imaging study, six human temporal bones were used, which were obtained in right-left pairs, from three cadaveric heads. All bones were fixed using formaldehyde. Only one bone from each pair was stained using IKI solution. Samples were scanned using a micro-computed tomography system. Contrast-to-noise ratios of eight middle-ear soft tissues were calculated for each temporal bone. Results from Welch's t-test indicate significant difference between the two soft tissues group, i.e., stained and unstained, at a 95% confidence interval. Results from a paired t-tests for each of the individual soft tissues also indicated significant improvement of contrast in all tissues after staining. The increase in contrast with IKI solution confirms its potential application in sample-specific FE modeling.

In the linear elasticity study, experiments were performed on three specimens with a custom-built pressurization unit at a quasi-static pressure of 500 Pa. The shape of each TM before and after pressurization was recorded using a Fourier transform profilometer. The samples were also imaged using micro-CT to create sample-specific FE models. For each

sample, the Young's modulus was then estimated by numerically optimizing its value in the FE model so simulated pressurized shapes matched experimental data. Also, the effects of incorporating two forms of spatial non-uniformity in the distribution of Young's modulus were studied, including partitioning the TM into 4 quadrants and 4 concentric rings. The estimated Young's modulus values were 2.2 MPa, 2.4 MPa and 2.0 MPa, which are similar to recent literature values using an alternative method. An improved fit between simulated and experimental data were obtained when spatial non-uniformity was incorporated.

Keywords: middle ear, tympanic membrane, micro-computed tomography, contrast, iodine potassium iodide, finite-element modeling, optimization, pressurization testing, Young's modulus, spatial non-uniformity

Co-Authorship Statement

This thesis is an integration of three articles, each presented in its own chapter. The publications listed in the following are either accepted for publication, under revision or in preparation.

Chapter 2: S.A. Rohani, S. Ghomashchi, J. Umoh, D.W. Holdsworth, S.K. Agrawal and H.M. Ladak, (2016) "Iodine potassium iodide improves the contrast-to-noise ratio of micro-computed tomography images of the human middle ear", *Journal of Microscopy*, 264(3), 334-338.

My contribution to this work included designing the study, preparing the samples, performing the staining, coordinating the imaging, analyzing the data and writing the manuscript. S. Ghomashchi performed the segmentations and the calculations. J. Umoh and D. W. Holdsworth performed the imaging. All authors reviewed and edited the manuscript. The work was performed under the supervision of S.K. Agrawal and H.M. Ladak.

Chapter 3: S.A. Rohani, S. Ghomashchi, S.K. Agrawal and H.M. Ladak, "Estimation of the Young's Modulus of the Human Pars Tensa Using In-Situ Pressurization and Inverse Finite-Element Analysis", was submitted to *Hearing Research* on June 15, 2016, and is currently under revision.

My contribution to this work included designing the study, preparing the samples, performing the experiments, developing the finite-element model, developing the optimization procedure, and writing the manuscript. S. Ghomashchi performed the segmentations and programming for optimization. All authors reviewed and edited the manuscript. The work was performed under the supervision of S.K. Agrawal and H.M. Ladak.

Chapter 4: S.A. Rohani, S. Ghomashchi, S.K. Agrawal and H.M. Ladak, "Spatial Non-Uniformity in the Young's Modulus of the Human Pars Tensa ", is under preparation for submission to *Journal of Biomechanics*.

My contribution to this work included designing the study, preparing the samples, performing the experiments, developing the finite-element model, developing the optimization procedure, and writing the manuscript. S. Ghomashchi performed the segmentations and programming for optimization. All authors reviewed and edited the manuscript. The work was performed under the supervision of S.K. Agrawal and H.M. Ladak.

This thesis is dedicated to memory of my brother,

Mohammadreza,

for his kindness, devotion and his endless support.

Acknowledgements

I would like to acknowledge my supervisor, Dr. Hanif Ladak, for his substantial support and guidance in my research. I would like to thank my joint supervisor, Dr. Sumit Agrawal, for his valuable clinical insight to this work. I also thank my advisory committee members, Dr. Prudence Allen and Dr. Abbas Samani for their insightful suggestions during my research. A special thanks to present and past members of the Auditory Biophysics Laboratory at Western University for creating such a friendly and professional environment.

I would like to express my deep gratitude to my family, my parents and siblings, and my beloved friends for their love and support.

Table of Contents

List of Tables

List of Figures

Chapter 1: Introduction

1.1 Motivation

Hearing loss is more widespread than many common diseases such as diabetes mellitus and all pediatric cancers (Morton, 1991). The prevalence of hearing loss is rapidly increasing. In 2008, the World Health Organization (WHO) estimated that more than 360 million (5.3% global population) individuals had a disabling hearing loss (Kaplan et al., 2013). This value increased to 414.5 million in 2013 (Vos et al., 2015). Also in 2013, the WHO listed hearing loss as a priority disease (Kaplan et al., 2013). As stated in the WHO report "hearing loss is an important health concern with substantial economic costs and social consequences" (Kaplan et al., 2013). Hearing loss in infants and young adults can significantly affect language development which is directly related to education, communication skills and psychological development (American Academy of Pediatrics, 2007). Fortunately, many of the lifelong consequences of hearing loss can be prevented if the loss is diagnosed properly at early stages.

Hearing loss can be conductive, sensorineural, or a combination of these two types. In conductive hearing loss, the outer and/or the middle ear are affected, while in sensorineural hearing loss the inner ear, nerves and brain are involved. The diagnosis of hearing loss involves finding the type of hearing loss since the treatment depends on the type of loss. The diagnostic process involves a series of otologic and audiologic examinations. Otologic examinations are initiated by family physicians and begin with visual inspection of the ear

canal and the eardrum for any pathologies. Suspicious cases are referred to audiologists. Audiologic tests often involve a series of pure-tone/speech audiometry and a combination of physiological measures. In the case that pure-tone/speech audiometry are not possible, for example in infants, audiologists rely only on non-behavioural responses and physiological measures (Stach, 2010). Tympanometry is a common non-behavioural test, in which the acoustic admittance of the middle ear is measured in response to an acoustic excitation over a range of quasi-static air pressures. In the cases that multiple pathologies exist in the middle ear, interpretation of tympanometric results becomes challenging (Shanks & Shelton, 1991).

One way to improve current diagnostic techniques, such as tympanometry, is to incorporate computer-based modeling and simulation (Daniel et al., 2001). With current developments in medical imaging, computers, software and measurement techniques, finite-element (FE) modeling has become a powerful technique to create detailed computer models of the ear. These models have been used to improve our understanding of the hearing mechanism, especially in the middle ear. Additionally, these FE models could potentially assist in interpreting clinical tests and diagnostic techniques by predicting pathologic conditions.

The accuracy of FE models of the middle ear is critically related to the accuracy of the representation of the geometry and mechanical properties of the middle-ear components. In recent years, many studies have focused on these two challenges in FE modeling. The geometry of the middle ear is usually reconstructed from 3D medical images. Computed tomography is often used because of the need to image bony structures, but the contrast of the soft tissues in the images has generally not been sufficient [e.g., (Sim et al., 2007; Homma et al., 2009; Lee et al., 2006; Lee et al., 2007)]. Also, the mechanical properties

have in recent years been estimated by inverse engineering to match simulation results to an experimental dataset. A wide variety of estimates are reported in the literature, further complicating modeling efforts. In this thesis, the application of a particular contrast agent to improve soft-tissue visualization with micro-computed tomography was studied. Furthermore, the technique was used to create sample-specific FE models for estimation of the mechanical properties of the eardrum. Following a brief review of ear anatomy and physiology, subsequent sections in this chapter review FE models of the middle ear in order to justify the objectives of this work.

1.2 Ear Anatomy and Physiology

In this section a brief review of human ear anatomy and physiology is provided. Overall, the ear is responsible for collecting sound waves in the environment and transducing them to neural signals that are sent to brain for processing. The human auditory system is conceptually divided into three main parts: the external ear, the middle ear, and the inner ear as shown in Figure 1-1.

Sound in the environment is collected by the auricle and focused down the ear canal. The sound waves vibrate the eardrum, also known as the tympanic membrane (TM). Vibrations of the TM in turn cause the middle-ear ossicular chain to vibrate. Vibrations of the most medial bone in the chain, the stapes, cause fluid to vibrate in the cochlea. In the cochlea, sound energy, now in the form of fluid vibrations, is transduced to neural signals that are sent to the brain for processing.

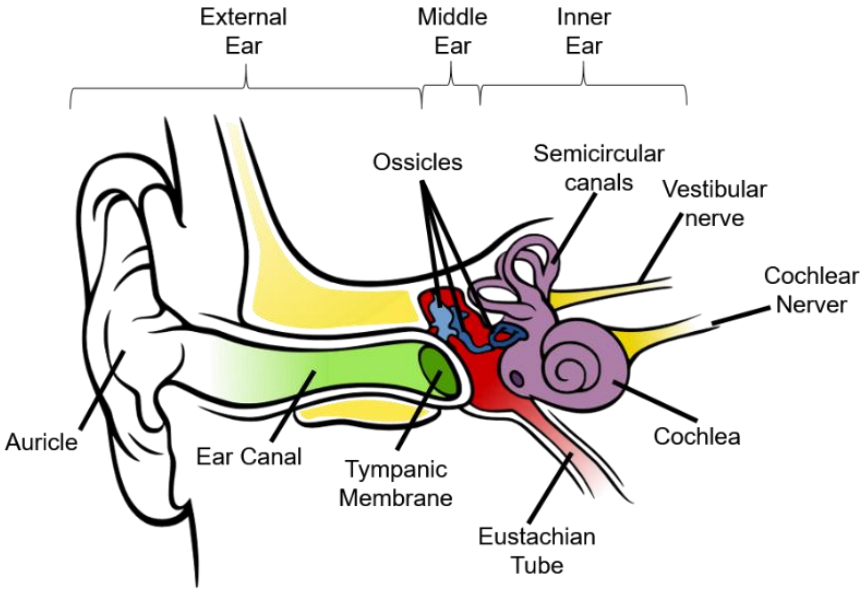

Figure 1-1: Anatomy of human ear. The ear is conceptually divided into three main parts: the external, middle and inner ears. Modified from (Chittka & Brockmann, 2009)

1.2.1 The External Ear

The external ear is the lateral part of the ear. It includes the auricle (also known as the pinna) and the ear canal (also known as the external acoustic meatus). The auricle is a cartilaginous organ, which its main function is to gather and direct the sound waves to the ear canal. The ear canal is a tube with one end closed by the TM. The ear canal connects the auricle to the middle ear and has a length of about 25 mm in adults (Standring, 2008). The lateral third of the ear canal is a continuation of the cartilaginous auricle while the medial two thirds are osseous; the entire ear canal is covered with skin (Standring, 2008).

1.2.2 The Middle Ear

The middle ear consists of the TM and three ossicles (i.e., malleus, incus and stapes). These tiny bones are suspended by several ligaments and tendons in the tympanic cavity, an air-filled space. The most medial bone in the middle ear, i.e., the stapes, connects the middle

ear to the cochlea of the inner ear. The main function of the middle ear is to amplify and transfer the sound from the ear canal to the cochlea.

The tympanic cavity is surrounded by the mastoid bone, which is a porous medium consisting of air cells. The ventilation of the tympanic cavity is controlled by the Eustachian tube, which connects the tympanic cavity to the nasopharynx (the part of the throat immediately behind the mouth). The tube is only opened during swallowing or yawning and closed most of the time. This allows for regulating the pressure difference between the tympanic cavity and the outside environment (Doyle, 2000).

Tympanic Membrane

The human TM is a fibrous conical-shaped membrane having an oval base with an apex pointing inward towards the tympanic cavity (Decraemer et al., 1991). The longest and shortest diameters are 9-10 mm and 8-9 mm, respectively (Standring, 2008). Peripherally it is connected to the ear canal at the tympanic ring, which is a ring of collagen fibres. It is connected to the malleus, the most lateral bone in the ossicular chain. The connection is made along the manubrium of the malleus in the centre of the TM. The TM consists of two parts; the pars tensa (PT) and pars flaccida (PF). A schematic diagram of the TM is given in Figure 1-2.

The mean thickness of the PT is about 79-97 μm in its central regions, and the thickness increases to 100-120 μm moving toward either the tympanic ring or the manubrium (Van der Jeught et al., 2013). The PF is a relatively thicker part with mean thickness of 230 μm (Lim, 1970). The PF covers only one-tenth of the entire TM (Lim, 1970).

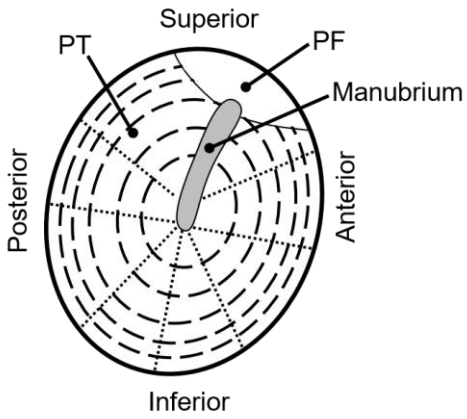

Figure 1-2: A schematic diagram of the human TM (right ear). The radial and circumferential directions of PT fibres are shown with dotted and dashed lines, respectively.

Histologically, both the PT and PF parts are composed of three layers: a lateral epidermal layer, an intermediate fibrous layer and an inner mucosal layer. The lateral layer is continuous with the skin of the ear canal. The mucosal layer is continuous with the mucosa of the tympanic cavity. The thickness of each of these two layers does not exceed 12 μm (Lim, 1970).

The PT and PF are different in the fibrous layer. The fibrous layer of the PT includes two sublayers of structured collagen fibres, one in the radial direction and one in the circumferential direction. These two fibrous layers in the PT are thought to be the main contributors to determining its mechanical properties, e.g., stiffness, On the other hand, the fibres in the PF lack organization and are randomly packed (Lim, 1968).

Ossicles, ligaments and tendons

As noted above, the middle-ear ossicular chain consists of three bones (the malleus, the incus and the stapes) which are suspended in the tympanic cavity by ligaments and acted upon by tendons. There is a disagreement among researchers on the naming and existence of certain ligaments in the middle ear [a comprehensive review is given on page 16 and

Table 2.1 in the thesis by C. Mikhael (Mikhael, 2005)]. In this work, only the most agreed upon ones are discussed when describing each of the ligaments and the ossicles they attach to. Figure 1-3 shows the ossicular chain.

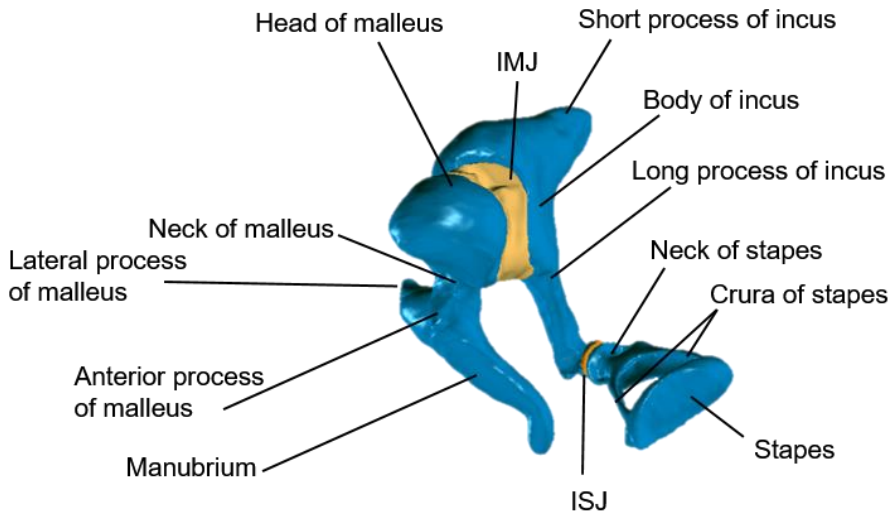

Figure 1-3: Ossicular chain. IMJ: incudo-mallear joint, ISJ: incudo-stapedial joint. This model is based on reconstruction of micro-computed tomography images as explained in Chapter 2.

The malleus is anatomically divided into 5 parts: the head, neck, manubrium, anterior process and lateral process. It is the largest ossicle in the middle ear and is 8-9 mm long (Standring, 2008). The malleus is attached to the TM along the length of the manubrium by a ligament. It is also supported by three suspensory ligaments at its anterior, superior and lateral sides. The ligaments are connected to the wall enclosing the tympanic cavity. The tensor tympani muscle is connected to the malleus by its tendon. The tendon is connected to the back of the manubrium, and its other end is attached to the muscle body which is housed in the anterior wall of the tympanic cavity.

The middle ossicle is the incus which is divided into 3 anatomical parts: body, short process and long process. There is a saddle-shaped cartilaginous joint on the anterior portion of its body for articulation with the head of the malleus; this articulation is called the incudo-

mallear joint. The short process, which is conical and projects posteriorly, is connected to the tympanic cavity wall by a ligament. The long process extends inferiorly in direction and bends medially. At its end, it has a rounded cartilaginous face to articulate with the stapes; this connection is called the incudo-stapedial joint.

The medial bone in the ossicular chain is the stapes. It is a stirrup-shaped bone having a head, neck, two legs and a footplate. The head is the most lateral part and articulates with the incus at the incudo-stapedial joint. The neck is a small part supporting the head. The tendon of the stapedius muscle connects to the posterior side of the neck; the muscle emanates from tympanic cavity wall. The footplate is attached to the cochlea and is supported by an annular ligament. The two legs (crura) connect the neck of stapes to the footplate on anterior and posterior sides.

1.2.3 The Inner Ear

The inner ear is a delicate sensory unit and is secured inside the dense temporal bone, the portion of the skull containing the ear. It includes two main parts: the semicircular canals and the cochlea. The semicircular canals are part of the balance system and communicate with the brain through vestibular nerves. The cochlea is a hearing organ and is connected to the stapes footplate. The vibrations of the middle ear are received by the inner ear through this connection. The cochlea is a bony snail-shaped structure filled with fluid. The transmitted vibrations move the fluid within the cochlea. These movements are then transduced to neural impulses by the sensory receptors in the cochlea and are sent by the cochlear nerve to the brain for processing and perception.

1.3 Structural Mechanics and Finite-Element Method

Generally, solid materials can be divided into two main categories; elastic and plastic. The differentiating factor is their response to an external load, e.g., applying pressure. Due to external loading, an elastic solid body will deform and returns to its initial shape upon unloading. This is in contrast to the response of a plastic solid body which will be permanently deformed. If the deformation is negligible, a solid body could be assumed as rigid. In elasticity theory, the response of an elastic solid body to an external load is described by a mathematical formulation between the internal forces (stress) and the deformation (strain). These mathematical formulations can only be solved for simply shaped objects, such as plates, cylinders, etc., and numerical techniques are required to apply them to objects with complex geometries such as the TM or middle-ear ossicles.

The finite-element (FE) method is a numerical technique which is capable of modeling systems with complex geometry. In this method, the geometry of the system is divided into a finite number of simpler objects, known as elements, and differential equations describing each element are solved using numerical techniques. The overall response of the system is then calculated by combining the results of the elements.

In this thesis, the mechanical properties of the TM as an elastic material are studied. Therefore, relevant fundamentals of elasticity theory and the FE method are briefly reviewed in this section.

1.3.1 Linear Elasticity

When an elastic material is deformed, the distances between the points in the body are changed. The work done by the applied loading will store energy in the body. This energy

is recoverable when the body returns to its initial configuration after it is unloaded. The energy is expressed in terms of the stresses and strains which are developed by the loading.

There are many treatises on elasticity theory and slightly different notations are used [e.g. (Mase & Mase, 1999; Ugural & Fenster, 2003)]. The formulations and terminologies used in following parts of this section are adapted from *"Elasticity: theory, applications, and numerics"* (Sadd, 2005).

Strain

In order to quantify the deformation of a body, the displacement of all points are needed. A general example of deformation is given in Figure 1-4. Let us consider P_0 and P which are two neighboring points in a 3D Cartesian coordinate system. They are separated by a distance $\boldsymbol{r}$ before deformation. After deformation the points will be transferred to P'_0 and P', respectively, with a separation distance of $\boldsymbol{r'}$.

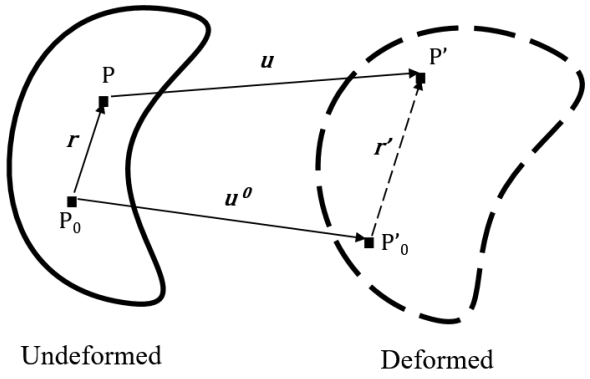

Figure 1-4: General deformation of two neighboring points.

In this chapter, the Cartesian index tensor notation is used in which the three orthogonal axes are labeled with x_1, x_2, x_3 and displacement vector $\boldsymbol{u}$ is expressed with u_1, u_2, u_3 . Also in this chapter, Einstein's summation notation is used in which repeated indices in a term indicates summation over all possible index values.

The displacement vector $\boldsymbol{u}$ of point P can be expressed using a Taylor series expansion around P_0. Since the relative position vector $\boldsymbol{r}(r_1, r_2, r_3)$ is assumed to have small components in the x_1, x_2 and x_3 directions, the higher-order terms of the Taylor series could be neglected and the series can be written as:

$$u_i = u_i^0 + \frac{\partial u_i}{\partial x_1} r_1 + \frac{\partial u_i}{\partial x_2} r_2 + \frac{\partial u_i}{\partial x_3} r_3 \qquad \text{Equation 1.1}$$

The change in the relative position vector $\boldsymbol{r}$ between the points after deformation can be written as

$$\Delta \boldsymbol{r} = \boldsymbol{r}' - \boldsymbol{r} = \boldsymbol{u} - \boldsymbol{u^0} \qquad \text{Equation 1.2}$$

Using Equations 1.1 and 1.2 gives:

$$\Delta r_i = \frac{\partial u_i}{\partial x_j} r_j \qquad \text{Equation 1.3}$$

The tensor $\partial u_i / \partial x_j$ or u_{ij} is called the *displacement gradient tensor* and has 9 components:

$$u_{ij} = \frac{\partial u_i}{\partial x_j} = \begin{bmatrix} \frac{\partial u_1}{\partial x_1} & \frac{\partial u_1}{\partial x_2} & \frac{\partial u_1}{\partial x_3} \\ \frac{\partial u_2}{\partial x_1} & \frac{\partial u_2}{\partial x_2} & \frac{\partial u_2}{\partial x_3} \\ \frac{\partial u_3}{\partial x_1} & \frac{\partial u_3}{\partial x_2} & \frac{\partial u_3}{\partial x_3} \end{bmatrix} \qquad \text{Equation 1.4}$$

Equation 1.4 could be decomposed into symmetric and antisymmetric tensors as

$$u_{ij} = e_{ij} + \omega_{ij} \qquad \text{Equation 1.5}$$

where

$$e_{ij} = \frac{1}{2}\left(u_{ij} + u_{ji}\right)$$
$$\omega_{ij} = \frac{1}{2}\left(u_{ij} - u_{ji}\right) \qquad \text{Equation 1.6}$$

The tensor e_{ij} is called the *strain tensor* and ω_{ij} is called the *rotation tensor*. Since it is initially assumed that the distances $\boldsymbol{r}$ and $\boldsymbol{r'}$ are infinitesimal and higher order terms of the Taylor series were neglected, these tensors are valid for small deformations only. Also, having these two tensors imply that the small deformation of an elastic body could be derived as sum of strain and rotation components.

The strain tensor, e_{ij}, has 9 components:

$$\boldsymbol{e}_{ij} = \begin{bmatrix} \dfrac{\partial u_1}{\partial x_1} & \dfrac{1}{2}\left(\dfrac{\partial u_1}{\partial x_2} + \dfrac{\partial u_2}{\partial x_1}\right) & \dfrac{1}{2}\left(\dfrac{\partial u_1}{\partial x_3} + \dfrac{\partial u_3}{\partial x_1}\right) \\ \dfrac{1}{2}\left(\dfrac{\partial u_2}{\partial x_1} + \dfrac{\partial u_1}{\partial x_2}\right) & \dfrac{\partial u_2}{\partial x_2} & \dfrac{1}{2}\left(\dfrac{\partial u_2}{\partial x_3} + \dfrac{\partial u_3}{\partial x_2}\right) \\ \dfrac{1}{2}\left(\dfrac{\partial u_3}{\partial x_1} + \dfrac{\partial u_1}{\partial x_3}\right) & \dfrac{1}{2}\left(\dfrac{\partial u_3}{\partial x_2} + \dfrac{\partial u_2}{\partial x_3}\right) & \dfrac{\partial u_3}{\partial x_3} \end{bmatrix} \quad \text{Equation 1.7}$$

where the strain tensor is symmetric with respect to the main diagonal. Taking this symmetry into account, 6 components remain for expressing the strain: three normal strains $(e_i = \varepsilon_i = \partial u_i/\partial x_i)$ and three shear strains $\left(e_{ij} = \gamma_{ij} = \partial u_i/\partial x_j + \partial u_j/\partial x_i\right)$.

Stress

Application of loading on a body generates internal forces that are distributed continuously within the body. These forces are quantified using *stress*, which is defined as the force over the unit area. The stress tensor $\boldsymbol{\sigma}$ is defined as

$$\boldsymbol{\sigma} = \begin{bmatrix} \sigma_1 & \tau_{12} & \tau_{13} \\ \tau_{21} & \sigma_2 & \tau_{23} \\ \tau_{31} & \tau_{32} & \sigma_3 \end{bmatrix} \quad \text{Equation 1.8}$$

where σ_1, σ_2 and σ_3 are referred to as *normal stresses* and the remaining 6 components are referred as *shear stresses*. These nine components are called Cauchy stress components.

Taking into account equilibrium, the shear stresses can be shown to be symmetric: $\tau_{12} = \tau_{21}, \tau_{23} = \tau_{32}, \tau_{31} = \tau_{13}$.

Hooke's Law

In the preceding sections, the stress and strain tensors are defined. The governing equation relating these two quantities is called a constitutive equation. In linear elasticity theory, this relation is linear, and can be written in matrix form:

$$\begin{bmatrix}\sigma_1\\ \sigma_2\\ \sigma_3\\ \tau_{12}\\ \tau_{23}\\ \tau_{31}\end{bmatrix} = \begin{bmatrix}C_{11} & C_{21} & C_{31} & C_{41} & C_{51} & C_{61}\\ C_{21} & . & . & . & . & .\\ . & . & . & . & . & .\\ . & . & . & . & . & .\\ . & . & . & . & . & .\\ C_{61} & . & . & . & . & C_{66}\end{bmatrix}\begin{bmatrix}\varepsilon_1\\ \varepsilon_2\\ \varepsilon_3\\ 2\gamma_{12}\\ 2\gamma_{23}\\ 2\gamma_{31}\end{bmatrix} \qquad \text{Equation 1.9}$$

or in index notation as:

$$\boldsymbol{\sigma} = C_{ij}\boldsymbol{e} \qquad \text{Equation 1.10}$$

where C_{ij} are elastic moduli and the factor of 2 in the shear strains arises because of the symmetry in the strains. The elastic modulus matrix C_{ij} expresses the elastic behaviour of a material, and it has the unit of stress (force/area). Its components depend on the nature of the material. An isotropic material has the same properties is all direction of applied forces.

For a linearly elastic isotropic solid, the matrix C_{ij} must be the same under all directions and all rotations of the coordinate system. The relation between stress and strain for such case is defined by g*eneralized Hooke's law*:

$$\sigma_{ij} = \lambda e_{kk}\delta_{ij} + 2\mu e_{ij} \qquad \text{Equation 1.11}$$

where δ_{ij} is the Kronecker delta, λ and μ are two constants and referred as Lame's constant and shear modulus, respectively. The stress-strain relation in Equation 1.11 can be inverted to express strain in terms of stress as:

$$e_{ij} = \frac{1}{2\mu}\left(\sigma_{ij} - \frac{\lambda}{3\lambda + 2\mu}\sigma_{kk}\delta_{ij}\right) \quad \text{Equation 1.12}$$

where $\sigma_{kk} = (3\lambda + 2\mu)e_{kk}$, or can be written in the form of

$$e_{ij} = \frac{1+\nu}{E}\sigma_{ij} - \frac{\nu}{E}\sigma_{kk}\delta_{ij} \quad \text{Equation 1.13}$$

where $E = \mu(3\lambda + 2\mu)/(\lambda + \mu)$ and $\nu = \lambda/[2(\lambda + \mu)]$. In this notation E is called the *modulus of elasticity* or *Young's modulus* and ν is referred as Poisson's ratio. Therefore, a linearly elastic isotropic material can be expressed using two parameters: Young's modulus and Poisson's ratio.

In the case that the stress is uniaxial, e.g., in the x_1 direction, the stress tensor in Equation 1.8 becomes:

$$\boldsymbol{\sigma} = \begin{bmatrix} \sigma_1 & 0 & 0 \\ 0 & 0 & 0 \\ 0 & 0 & 0 \end{bmatrix} \quad \text{Equation 1.14}$$

Substituting Equation 1.14 in Hooke's law (Equation 1.13) gives:

$$\boldsymbol{e}_{ij} = \begin{bmatrix} \frac{\sigma_1}{E} & 0 & 0 \\ 0 & -\frac{\upsilon}{E}\sigma_1 & 0 \\ 0 & 0 & -\frac{\upsilon}{E}\sigma_1 \end{bmatrix} \quad \text{Equation 1.15}$$

Therefore,

$$E = \sigma_1/e_1 \quad \text{Equation 1.16}$$

and

$$\upsilon = -\frac{e_2}{e_1} = -\frac{e_3}{e_1} \quad \text{Equation 1.17}$$

In solid mechanics, in order to estimate the Young's modulus of a material, tensile testing is often used. In this test, a block of material with standard shape and size undergoes

uniaxial testing and a stress-strain curve is plotted. Using Equations 1.16 and 1.17, the two parameters needed for expressing the mechanical behaviour is obtained. This technique is also applied on biological tissues, such as TM, which is discussed later in this chapter and Chapter 3.

Strain Energy

The problems in solid mechanics are generally involves in finding stress or strain of a body, over certain a domain, caused by a particular loading condition. The solution procedure generally starts with writing static equilibrium equations: summation of force and moments are zero for the entire body and any subdomain. This usually results in partial differential equations that need to be solved. Analytical solutions for such problems are achieved for objects having relatively simple geometry and boundary shape. For objects with complex geometries the numerical techniques are developed to approximate the solution is based on the energy stored in the object.

This energy is equal to the net work done by the forces:

$$U = \frac{1}{2}(\sigma_1 e_1 + \sigma_2 e_2 + \sigma_3 e_3 + \tau_{12}\gamma_{12} + \tau_{23}\gamma_{23} + \tau_{31}\gamma_{31}) = \frac{1}{2}\sigma_{ij}e_{ij} \qquad \text{Equation 1.18}$$

Based on Hooke's law, for a linear elastic isotropic material, Equation 1.18 can be written solely in terms of strain:

$$\begin{aligned} U(\boldsymbol{e}) &= \frac{1}{2}\lambda e_{jj}e_{kk} + \mu e_{ij}e_{ij} \\ &= \frac{1}{2}\lambda(e_1 + e_2 + e_3)^2 + \mu\left(e_1^2 + e_2^2 + e_3^2 + \frac{1}{2}\gamma_{12}^2 + \frac{1}{2}\gamma_{23}^2 + \frac{1}{2}\gamma_{31}^2\right) \end{aligned} \qquad \text{Equation 1.19}$$

1.3.2 Finite-Element Method

The fundamental concept of the FE method is based on dividing the geometry of the system into a finite number of elements. Elements are simple geometric subdomains, e.g., triangles

and tetrahedra, defined with nodes (vertices of the element), edges and faces. Then based on particular assumptions, the variation of the unknown variables on each node is quantified as an algebraic system of equations. In this formulation, the elasticity equations are reformulated to minimize the energy of the system. With the advantage of adjustable element size and shape, the FE method can handle problems of complicated shape. In this section, a brief introduction of this method is provided for modeling a solid continuum having linear elastic properties.

There are three main steps in FE modeling:

1. Pre-processing:
    a. Reconstructing object geometry
    b. Mesh generation (breaking the system into elements)
    c. Assigning material properties
    d. Assigning boundary conditions, and
    e. Mathematical formulation.
2. Processing: Solving the mathematical formulation in step 1.
3. Post-processing:
    a. Analyzing the outputs of the processing step, and
    b. Validating the results.

In FE modeling of a solid continuum, the geometry of the object being considered is required. The object could be imaged using any of various imaging technologies that are available. Object boundaries can then be segmented from the image to reconstruct the surface geometry of the object. The interior of the reconstructed geometry is then

subdivided into a mesh of small components such as hexahedral and tetrahedral elements, each of which consists of nodes and faces. The number of nodes of the mesh defines the degree of freedom (DOF) of the system.

Based on the characteristics of the model, the material properties and boundary conditions are assigned for each element. As discussed before, the material properties are defined with parameters such as Young's modulus and Poisson's ratio. The boundary conditions include the initial loading, external or internal forces, the constraints on displacements and rotations and the interaction of the objects in the system. For example, constraints could include specifying which faces or nodes of the mesh that are not moving (or fixed), which are pre-stressed or which are in contact with other objects. Furthermore, the constitutive equations describing the system are selected.

The total work done by the forces is zero. For one element it can be stated as:

$$\delta W = \int_V \sigma_{ij} \delta e_{ij} dV = 0 \qquad \text{Equation 1.20}$$

where σ_{ij} is the stresses and δe_{ij} is the strain. In Equation 1.20, the strain component, e_{ij}, can be written in terms of displacement components u_i. With the benefit of having small element dimensions, this formulation can be linearized for each element, resulting in a system of linear equations. Solving the resulting system of linear equations provides the response of the system. More details on the numerical techniques for FE method are available in typical textbooks on FE method such as (Bathe, 1996) and (Zienkiewicz & Taylor, 2000a).

There are many software packages, both commercial and free, for the FE method. Examples of commercial packages that perform all three steps are ANSYS (ANSYS, Inc., Canonsburg, PA, USA), ABAQUS (Dassault Systèmes Americas Corp., Waltham, MA, USA), COMSOL Multiphysics (COMSOL, Inc., Burlington, MA, USA). Free software packages for FE method are developed for specific steps. For example, the FEBio Software Suite (www.febio.org, accessed on 07 July, 2016) has three separate components, PreView, FEBio, and PostView for pre-processing, processing, and post-processing steps, respectively. The are some technical considerations needed to be taken in to account in FE analysis, which are explained in following.

Geometry

The geometry of the model is significant in the FE method. In structural and mechanical engineering, the geometry is reconstructed using computer aided design (CAD) software packages, such as SolidWorks (Dassault Systèmes SolidWorks Corporation, Waltham, MA, USA). In biomedical problems, however, the geometry cannot be drawn and must be imported from reconstructed datasets from medical imaging modalities, such as computed tomography (CT), magnetic resonance imaging (MRI) and ultrasound imaging. Therefore, the accuracy of the geometry depends on the resolution and accuracy of these modalities as well as image segmentation and surface reconstruction steps.

Mesh

Currently, software packages allow users to select a variety of mesh types and sizes. A coarse mesh (larger elements) generates a small system of equations, which reduces the processing time, but the accuracy of the results may not be high enough. On the other hand, a very fine mesh (small elements), results in a high computational cost. A systematic mesh

analysis, including mesh convergence tests and adaptive refinement, should be performed to obtain an appropriate mesh that balances accuracy and computational cost [more details on Chapter 15 of Zienkiewicz & Taylor, 2000b].

Material properties

Based on the nature of the system that is under study, appropriate simplifications and assumptions need to be taken into account in FE modeling. This may not only reduce the computational cost but could also result in more accurate simulations. For example, modelling a quasi-static linear condition with a non-linear representation not only increases the computational cost, but may result in numerical errors. Also, accurate parameters of material properties are important for the FE method.

Boundary conditions

In general, the interactions between the components of the system and with the environment (boundaries and external loads) could be very complicated. A successful FE model should include those interactions in a simplified, but accurate enough manner. For example, instead of modelling the air cells in the tympanic cavity, the reduction of acoustic admittance is taken into account in the post processing.

Validation

In most FE modeling problems, there is a physical phenomenon/experimental dataset which can be compared to the modeling results. Model validation refers to the verification of every step of the FE method earlier in this section. For example: How accurately is the geometry represented? How optimized is the mesh in terms of element size and type? Are

the assumptions on boundary conditions representative of the experimental situation? Is the model over-simplified? Is the mathematical formulation suitable for this experiment?

1.4 Finite-Element Modeling of the Middle Ear

1.4.1 Overview

Over the past few decades, different modeling techniques have been applied to model the physics of the human/animal ear, leading to lumped parameter circuit models (Parent & Allen, 2010; Zwislocki, 1962), physical models (Stieger et al., 2007; Taschke et al., 2000) or multi-body models (Eiber & Schiehlen, 1996). Although the overall acoustical behavior of the ear is modeled in these approaches, they provide limited information regarding geometrical and biological complexities because for some approaches such as lumped parameter models, the continuum is idealized as a point. For example, the effects of local scarring of the TM cannot be modeled, although scarring can lead to masking of more medial pathologies, resulting in poor interpretation of audiological tests. The FE method can mitigate such limitations because it models the continuum.

FE modeling of the middle ear was introduced by Funnell and Laszlo in the 1970s by modeling the cat eardrum (Funnell & Laszlo, 1978). Subsequently, FE models of the entire middle ear have been developed for different purposes during the last four decades. Improving the knowledge of the complex biological structure of the hearing system was the main objective for most published models, including understanding TM mechanics (Funnell, 1983; Aernouts et al., 2010; Aernouts & Dirckx, 2011; Akache et al., 2006; Hesabgar et al., 2010; Ladak et al., 2004; Ladak et al., 2006), mechanics of the ossicles and of the joints (Decraemer et al., 2003; Funnell et al., 2005; Homma et al., 2009; Chou et al., 2010; Zhang & Gan, 2011), biomechanical effects of the ligaments (Huber et al., 2003;

Gentil et al., 2011; Gan et al., 2011; Dai et al., 2007) and understanding sound transmission (Gan et al., 2007). In addition, there are multiple studies performed related to modeling and optimization of middle-ear prostheses (Kelly et al., 2003; Bance et al., 2004; Neudert et al., 2007; Kim et al., 2006; Gan et al., 2010).

The accuracy of FE models is determined by the accuracy of the underlying geometrical representation and of the material models. A review of the representation of the geometry and material properties used in FE modeling of the middle ear is provided in this section.

1.4.2 Geometry of The Middle Ear

The first step in creating an FE model of the middle ear is obtaining the geometry. As mentioned earlier in Section 1.3.2, the geometry of the middle ear should be imported as 3D reconstructed models. For the TM only, it is possible to import its geometry as a surface model with thickness derived from measurements. In this work, three common techniques used to acquire TM geometry including Moiré profilometry, histological sectioning and computed tomography are briefly explained and discussed.

Moiré Profilometry

Moiré profilometry is an optical measurement technique to measure the shape of a surface. In this method, a grating consisting of parallel straight lines is projected onto the surface of an object. Due to the object's geometry, the projection of the grating lines appears deformed. The deformation encodes the height of the surface measured relative to the plane of the physical grating. The deformed projection is imaged and is numerically processed to decode the object's height, yielding a dense matrix of height values that define the object's surface shape.

This technique has been widely used for FE modeling of the TM [e.g., (Aernouts et al., 2010; Ladak et al., 2006; Fay et al., 2006; Elkhouri et al., 2006; Buytaert et al., 2009)]. The main advantage of this technique is the ability to record the shape of both the undeformed and deformed TM shapes in a relatively short time. Therefore, this technique is suitable for investigation of material properties when the shape in both conditions is required for inverse modeling as described later. One limitation of this technique is that it can only be applied to the TM and cannot be used to obtain the geometry of the ossicles or ligaments in the middle ear.

Histological Sectioning

In histological sectioning, the geometry is obtained by reconstruction of images obtained through physical micro-slices of a temporal bone. In order to prepare the temporal bone for sectioning, it undergoes a series of intensive chemical and physical processing steps. As described by Gan *et al.*, after fixation of the bone in 10% formalin solution, it is immersed in 10% nitric acid solution for 2 weeks for decalcification (Gan et al., 2002). Furthermore, the bone is dehydrated using an ethanol alcohol series before being embedded in celloidin for 3 weeks. Celloidin is a concentrated form of nitro-cellulose which is commonly used for histological sectioning. After embedding, the specimen is sectioned into approximately 600 slices with 20 μm thickness; these values are most suitable for middle-ear studies. Usually, every tenth slide is scanned into a computer for processing. Finally, each component of the middle ear is outlined manually on the 60 digitized slices and the geometry of the middle ear is reconstructed in 3D.

Histological sectioning provides accurate representation of the details of the middle-ear components. The disadvantages of this technique are that it is destructive, labor intensive

and may cause shearing of the TM. Also, it cannot be performed to capture the deformation of the TM, as with Moiré profilometry.

Computed Tomography

Two types of computed tomography are used in the development of middle-ear FE models: *ex-vivo* micro-computed tomography (micro-CT) (Tuck-Lee et al., 2008; Sim & Puria, 2008; Kelly et al., 2003) and *in-vivo* high-resolution computed tomography (Lee et al., 2006; Chou et al., 2010).

The resolution of *in-vivo* CT is too coarse to image most middle-ear structures with sufficient fidelity. For instance, several studies use scanners with resolutions of about 600 μm which is many times the thickness of the TM; therefore, micro-CT imaging has become the common technique for obtaining the geometry because of its much higher resolution. Although micro-CT is widely used because of its ability to image bony structures of the middle ear, it is difficult to visualize soft tissues because of low contrast.

There is relatively little work done on contrast enhancement of the middle-ear soft tissues when using micro-CT. One method to improve the contrast involves staining the specimen with contrast agents. Three common contrast agents for staining soft tissues when using micro-CT imaging are osmium tetroxide, phosphotungstic acid (PTA) and iodine potassium iodide (IKI) (Metscher, 2009). PTA has been used to visualize middle-ear morphology when using micro-CT (Buytaert et al., 2014; Aerts et al., 2012; De Greef et al., 2015). Chapter 2 of this thesis quantifies the contrast improvement of soft tissues in the middle ear using IKI as a contrast agent.

An alternative approach to staining is combining data from two imaging modalities. Buytaert et al. (Buytaert et al., 2011) combined data from high-resolution micro-CT recordings with data from high-resolution orthogonal-plane fluorescence optical-sectioning microscopy (OPFOS). OPFOS is an optical technique with very high resolution. It can be used to visualize both soft tissues and bone if the structures can be made transparent. This particular combination is challenging to use and requires substantial amount of chemical processing to make all tissues transparent for OPFOS imaging. These processing steps can significantly alter the geometry of the tissues.

1.4.3 Material Properties of the Middle-Ear Components

As mentioned earlier, the mechanical properties of the elements in an FE model are assigned based on the assumptions considered when forming the model, including consideration of the loading condition. The material properties of the components of the middle ear are reviewed in this section with particular emphasis on the TM.

Ossicles, Ligaments and Tendons

Ossicles are commonly considered to be isotropic linear elastic materials with Young's modulus of 14.1 GPa and Poisson's ratio of 0.3 [e.g., (Gan et al., 2004; Gan et al., 2002; Gan et al., 2006; Lee et al., 2006; Sun et al., 2002)]. In the case that inertial effects are also considered, i.e., where dynamic analysis is involved, the ossicles are not considered as uniform in terms of density. For example, densities of the malleus head, neck and manubrium are taken as 2.55 g/cm^3, 4.53 g/cm^3 and 3.7 g/cm^3, respectively [e.g., (Gan et al., 2006; Lee et al., 2010; Sun et al., 2002; Wen et al., 2006; Chou et al., 2010; Lee et al., 2006)].

Non-linear hyperelastic models are shown to be suitable to represent the mechanical properties of middle-ear ligaments and tendons [e.g., (Gan et al., 2011; Cheng & Gan, 2007; Cheng & Gan, 2008)]. But they are usually modelled as linear elastic materials with low Young's modulus values [e.g., (Gan & Sun, 2002; Sun et al., 2002; Gentil et al., 2011; Lee et al., 2006)]. A more detailed tabulation of the parameters used for the ossicles, ligaments, tendons and joints in the middle ear are provided in the work by Volandri *et al.* (Volandri et al., 2012).

Tympanic Membrane

The mechanical properties of the TM are affected by its ultrastructure and loading condition. As mentioned earlier, the ultrastructure of the PT and PF are not the same, which results in the PT being the stiffer part.

The PT has been modelled as a linear elastic isotropic material in many FE models [e.g., (Gan & Sun, 2002; Elkhouri et al., 2006; Mikhael et al., 2004; Koike et al., 2005; Takuji et al., 2001; Daniel et al., 2001; Funnell & Laszlo, 1978; Ladak et al., 2006; Lesser & Williams, 1988)]. It has also been modelled as a linear elastic orthotropic material, where the elasticity of the PT is defined using two moduli: one for the radial direction and one for the circumferential direction [e.g., (Gan et al., 2006; Sun et al., 2002; Gan et al., 2004; Lee et al., 2010; Lee et al., 2006)]. In cases where large deformation of the PT is considered, it has been modeled as a non-linear hyperelastic material, such as a five-parameter Mooney-Rivilin model (Wang et al., 2007) or two-parameter Ogden model (Cheng et al., 2007).

Because of the PF ultrastructure, it has commonly been modelled as a linear elastic isotropic material in FE models; it is usually taken to have a lower Young's modulus value

with respect to the PT [e.g., (Gan & Sun, 2002; Elkhouri et al., 2006; Ladak et al., 2006; Koike et al., 2002)]. The exceptions are the works by Cheng *et al.* and Aernouts & Dirckx, where the PF was modelled as a hyperelastic material (Cheng et al., 2007; Aernouts & Dirckx, 2011) because of the large loads being considered in those works.

The mechanical properties of the human TM are obtained through mechanical testing techniques, such as tensile testing and indentation testing. Such techniques follow an inverse engineering method where parameters indicating the material properties (e.g., Young's modulus) are mathematically optimized to match the experimental data (e.g., indentation) to the FE model which was developed from the sample being tested. A review of the methods of estimating mechanical properties of the TM is provided in Section 3.1. The literature values for PT Young's modulus has a wide range from ~0.5 MPa (Cheng et al., 2007) to 300 MPa (Fay et al., 2005). A detailed review of estimated values is provided in Section 3.4 of this thesis.

1.5 Optimization

In general, an optimization problem consists of finding the parameter(s) which are maximizing or minimizing an objective function. In problems focusing on the estimation of material properties (e.g., Young's modulus of TM), the objective function is defined based on comparing the output of a model (e.g., an FE model) with the results of experimental data. In such a model, the input is a value representing the material properties and the output is the parameter which was measured in the experiment (e.g., displacement, strain, etc.). Therefore, the aim is to systematically modify the inputs (also known as control variables) of the model to match the output of the model with the experimental data.

The objective function needs to be minimized to obtain a match between the simulation and experimental datasets. In such cases, the objective function is also called as "cost function". In material estimation cases, there is a constraint on the control variables. For example, Young's modulus values cannot be negative, or Poisson's ratio should be within the range of 0 to 0.5.

An objective function could have various shapes, depending on the nature of the optimization problem and the number of variables. For a univariable optimization problem, a unimodal objective function is a function with only one global minimum/maximum. For a unimodal objective function $f(x)$ with a minimum at x_m for $-\infty < x < +\infty$, this means that $f(x)$ is decreasing when moving from $-\infty$ toward x_m, and it increases when moving from x_m toward $+\infty$. Figure 1-5 shows an example of such a function.

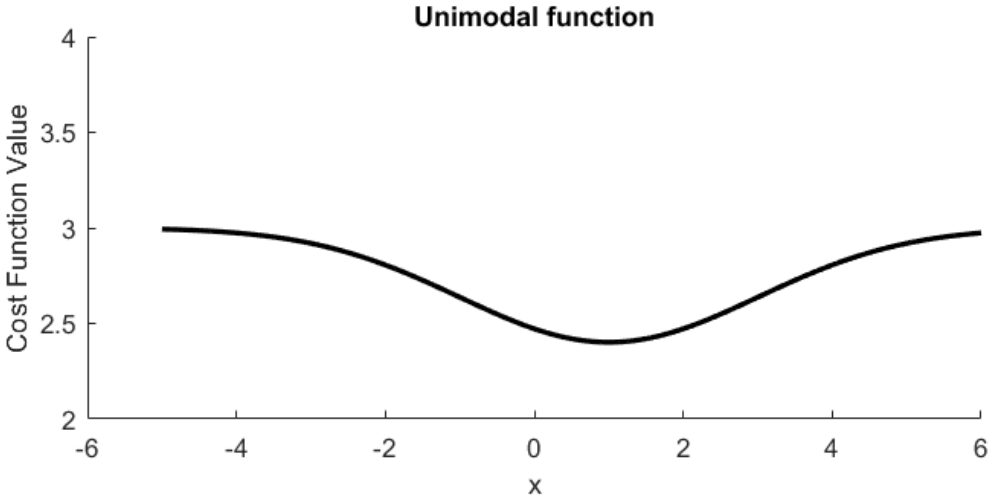

Figure 1-5: An example of unimodal function. Only one global minimum is attained for all values of *x* at *x* = 1.

The alternative to a unimodal is multimodal function which has multiple local minima/maxima while could have a unique global minimum/maximum. An example of a multimodal is given in Figure 1-6.

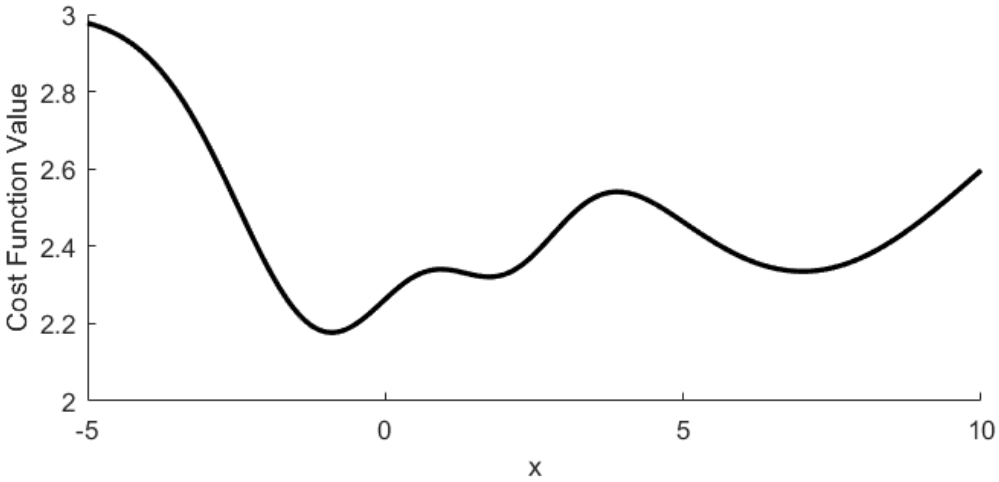

Figure 1-6: An example of multimodal function. Only one global minimum is attained (at x = -1) for all values of x, while there are two local minima (x = 2 and x = 7).

Depending on the type of optimization problem (unimodal vs multimodal) and the number of control variables (single-variable vs multivariable), the optimization approach varies. Optimization techniques can generally be divided into two categories: derivative-based and derivative-free.

In derivative-based methods, the algorithm calculates the gradient of the objective function at a point (using numerical techniques) and tries to reach the point where the gradient is equal to zero, which is the local extremum of the objective function. In general, these methods are fast and accurate, but if the objective function is affected by noise, e.g., as a result of an experimental procedure, the gradient-based may not converge to the extremum.

For the cases where the derivative of the objective function is either unavailable or unreliable, derivative-free optimization techniques are used. The accuracy of these techniques are relatively less than derivative-based options due to the absence of the gradient at the extremum, so they are used when the objective function evaluations are noisy and/or computationally expensive (Conn et al., 2009). Since the pointwise behavior

(e.g., gradient) of the objective function is not used, then these algorithms are based on sampling the objective function at different control variable values to search for the next step toward the minima/maxima. This results in a more expensive but more robust algorithm since it does not follow a path based on the derivative of the objective function at a single point.

The derivative-free solvers can further be divided into local-optimizer or global-optimizer methods. In local optimization, the algorithm starts at a point (initial guess) and attempts to improve the objective function in an iteratively stepwise manner. On the other hand, in the global optimization methods, the objective function is mapped over a global range of control variable values and it is refined until a global extremum is achieved.

In this thesis, two optimization algorithms were used. In Chapter 3, a univariable cost function was minimized using "golden-section search with parabolic interpolation". In Chapter 4, a multi-variable cost function was minimized using "Nelder-Mead simplex method". Therefore, these two methods are explained in the following sections.

Golden-section search with parabolic interpolation algorithm is a univariable optimizer for strictly unimodal functions when the extremum is within a known range. The algorithm refines the range iteratively toward the extremum until the range becomes smaller than the defined tolerance (Forsythe et al., 1977; Brent, 1973). This is a fast and robust technique for unimodal objective functions.

The Nelder-Mead simplex method is a multivariable local optimizer which uses a simplex of $n+1$ points for an n-dimensional objective function. The algorithm requires an initial guess for the vertices of the initial simplex. Then by a series of rules this simplex is

reshaped and moved in the *n*-dimensional space until the simplex is small enough that all vertices are within tolerance range from each other. The details of the rules for reshaping the initial simplex are described in the literature [e.g., (Lagarias et al., 1998)].

1.6 Objectives

The long-term objective of the Auditory Biophysics Laboratory at Western University is to develop accurate sample-specific FE models of the middle ear to simulate audiological hearing tests, such as tympanometry. As mentioned before, these models could assist in diagnosis of hearing disorders. In order to develop such models, accurate material properties of the middle-ear components are required, especially for the TM. One way to obtain such information is through inverse engineering, which involves mechanical testing and optimization of the parameters of an FE model to match experimental measurements. In this process accurate representation of the geometry of the middle-ear components is required. Therefore, the specific objectives of this thesis are:

1. Quantify the effect of IKI as a contrast agent for improving contrast of soft tissues in micro-CT images of the human middle ear. The aim of this study is to develop a technique which could be used for creating the geometry of FE models in a sample-specific manner.
2. Estimate the Young's modulus of the PT. Knowing that the behaviour of TM varies based on the loading condition, the focus of this study is to perform the estimation in a situation similar to tympanometry, i.e., quasi-static pressurization.

3. Investigate the spatial non-uniformity in Young's modulus of the PT. The benefit of this study is to examine whether adding such complexity (i.e., spatial non-uniformity) to the FE model increases the accuracy.

1.7 Thesis Outline

This thesis is based on three manuscripts presented in the following chapters. Chapter 2 presents a study on efficacy of using IKI as a contrast agent for micro-CT imaging of the middle ear. The study in that Chapter involves comparing images of stained and unstained samples. In the study presented in Chapter 3, the Young's modulus of the human PT is estimated through inverse engineering based on data from an *in-situ* pressurization experiment. In Chapter 4 the study of Chapter 3 is extended to include the spatial non-uniformity of the PT Young's modulus. In Chapter 5, the thesis is summarized and future directions are suggested.

1.8 References

Aernouts, J. & Dirckx, J.J.J. (2011) Elastic characterization of the gerbil pars flaccida from in situ inflation experiments. *Biomechanics and Modeling in Mechanobiology*. **10**(**5**), 727–741.

Aernouts, J., Soons, J. a M. & Dirckx, J.J.J. (2010) Quantification of tympanic membrane elasticity parameters from in situ point indentation measurements: Validation and preliminary study. *Hearing Research*. **263**(**1**–**2**), 177–182.

Aerts, J.A.N., Dirckx, J.J.J., Dierick, M. & Van Hoorebek, L. (2012) High-resolution 3D surface model of bone and soft tissue structures in the human middle ear. In *ARO mid-winter meeting*. San Diego, California, USA.

Akache, F., Funnell, W.R.J. & Daniel, S.J. (2006) An experimental study of tympanic membrane and manubrium vibrations in rats. *Audiology and Neurotology*. **12**(**1**), 49–58.

American Academy of Pediatrics (2007) Year 2007 Position Statement: Principles and Guidelines for Early Hearing Detection and Intervention Programs. *Pediatrics*. **120**(**4**), 898–921.

Bance, M.L., Morris, D.P., Vanwijhe, R.G., Kiefte, M. & Funnell, W.R.J. (2004) Comparison of the mechanical performance of ossiculoplasty using a prosthetic malleus-to-stapes head with a tympanic membrane-to-stapes head assembly in a human cadaveric middle ear model. *Otology & neurotology*. **25**(**6**), 903–909.

Bathe, K.-J. (1996) *Finite Element Procedures*, New Jersey, USA: Prentice-Hall.

Brent, R.P. (1973) *Algorithms for Minimization without Derivatives*, Englewood Cliffs, New Jersey, USA: Prentice-Hall.

Buytaert, J.A.N., Salih, W.H.M., Dierick, M., Jacobs, P. & Dirckx, J.J.J. (2011) Realistic 3D computer model of the gerbil middle ear, featuring accurate morphology of bone and soft tissue structures. *Journal of the Association for Research in Otolaryngology*. **12**(**6**), 681–696.

Buytaert, J., Aernouts, J. & Dirckx, J. (2009) Indentation measurements on the eardrum with automated projection moiré profilometry. *Optics and Lasers in Engineering*. **47**(**3**), 301–309.

Buytaert, J., Goyens, J., De Greef, D., Aerts, P. & Dirckx, J. (2014) Volume Shrinkage of Bone, Brain and Muscle Tissue in Sample Preparation for Micro-CT and Light Sheet Fluorescence Microscopy (LSFM). *Microscopy and Microanalysis*. **20**(**4**), 1208–1217.

Cheng, T., Dai, C. & Gan, R.Z. (2007) Viscoelastic properties of human tympanic membrane. *Annals of Biomedical Engineering*. **35**(**2**), 305–314.

Cheng, T. & Gan, R.Z. (2008) Experimental measurement and modeling analysis on mechanical properties of tensor tympani tendon. *Medical engineering & physics*. **30**(**3**), 358–366.

Cheng, T. & Gan, R.Z. (2007) Mechanical properties of stapedial tendon in human middle ear. *Journal of biomechanical engineering*. **129**(**6**), 913–918.

Chittka, L. & Brockmann, A. (2009) Anatomy of the Human Ear. Available at: https://commons.wikimedia.org/wiki/File:Anatomy_of_the_Human_Ear_en.svg [Accessed August 3, 2016].

Chou, C.F., Yu, J.F. & Chen, C.K. (2010) The natural vibration characteristics of human ossicles. *Chang Gung medical journal*. **34**(**2**), 160–165.

Conn, A.R., Scheinberg, K. & Vicente, L.N. (2009) *Introduction to Derivative-Free Optimization*, Philadelphia, PA, USA: Society for Industrial and Applied Mathematics and the Mathematical Programming Society.

Dai, C., Cheng, T., Wood, M.W. & Gan, R.Z. (2007) Fixation and detachment of superior and anterior malleolar ligaments in human middle ear: Experiment and modeling. *Hearing Research*. **230**(**1**–**2**), 24–33.

Daniel, S.J., Funnell, W.R.J., Zeitouni, A.G., Melvin, D., Daniel, S.J., Funnell, W.R.J., Zeitouni, A.G., Schloss, M.D. & Rappaport, J. (2001) Clinical Application of a Finite-Element Model of the Human Middle Ear. *The Journal of Otolaryngology*. **30**(**6**), 340.

Decraemer, W.F., Dirckx, J.J.J. & Funnell, W.R.J. (1991) Shape and derived geometrical parameters of the adult, human tympanic membrane measured with a phase-shift moire interferometer. *Hearing Research*. **51**(**1**), 107–121.

Decraemer, W.F., Dirckx, J.J.J. & Funnell, W.R.J. (2003) Three-dimensional modelling of the middle-ear ossicular chain using a commercial high-resolution X-ray CT scanner. *JARO - Journal of the Association for Research in Otolaryngology*. **4**(**2**), 250–263.

Doyle, W.J. (2000) Middle ear pressure regulation. In J. J. ; Rosowski & S. N. ; Merchant, eds. *The Function and Mechanics of Normal, Diseased and Reconstructed Middle Ears - Google Books*. Amsterdam, The Netherlands: Kugler Publications, pp. 3–21.

Eiber, A. & Schiehlen, W. (1996) Reconstruction of hearing by mechatronical devices. *Robotics and Autonomous Systems*. **19**(**2**), 199–204.

Elkhouri, N., Liu, H. & Funnell, W.R.J. (2006) Low-frequency finite-element modeling of the gerbil middle ear. *Journal of the Association for Research in Otolaryngology*. **7**(**4**), 399–411.

Fay, J., Puria, S., Decraemer, W.F. & Steele, C. (2005) Three approaches for estimating the elastic modulus of the tympanic membrane. *Journal of Biomechanics*. **38**(**9**), 1807–1815.

Fay, J.P., Puria, S. & Steele, C.R. (2006) The discordant eardrum. *Proceedings of the National Academy of Sciences of the United States of America*. **103**(**52**), 19743–19748.

Forsythe, G.E., Malcolm, M.A. & Moler, C.B. (1977) *Computer Methods for Mathematical Computations*, New Jersey, USA: Prentice-Hall.

Funnell, W.R.J. (1983) On the undamped natural frequencies and mode shapes of a finite-element model of the cat eardrum. *The Journal of the Acoustical Society of America*. **73**(**5**), 1657–1661.

Funnell, W.R.J., Heng Siah, T., McKee, M.D., Daniel, S.J. & Decraemer, W.F. (2005) On the coupling between the incus and the stapes in the cat. *JARO - Journal of the Association for Research in Otolaryngology*. **6**(**1**), 9–18.

Funnell, W.R.J. & Laszlo, C.A. (1978) Modeling of the cat eardrum as a thin shell using the finite-element method. *The Journal of the Acoustical Society of America*. **63**(**5**), 1461–1467.

Gan, R. & Sun, Q. (2002) Finite element modeling of human ear with external ear canal and middle ear cavity. *Engineering in Medicine and Biology, 2002.*

Gan, R.Z., Dai, C., Wang, X., Nakmali, D. & Wood, M.W. (2010) A totally implantable hearing system - Design and function characterization in 3D computational model and temporal bones. *Hearing Research*. **263**(**1**–**2**), 138–144.

Gan, R.Z., Feng, B. & Sun, Q. (2004) Three-dimensional finite element modeling of human ear for sound transmission. *Annals of Biomedical Engineering*. **32**(**6**), 847–859.

Gan, R.Z., Reeves, B.P. & Wang, X. (2007) Modeling of sound transmission from ear canal to cochlea. *Annals of Biomedical Engineering*. **35**(**12**), 2180–2195.

Gan, R.Z., Sun, Q., Dyer, R.K., Chang, K.-H. & Dormer, K.J. (2002) Three-dimensional modeling of middle ear biomechanics and its applications. *Otology & neurotology*. **23**(**3**), 271–280.

Gan, R.Z., Sun, Q., Feng, B. & Wood, M.W. (2006) Acoustic-structural coupled finite element analysis for sound transmission in human ear--pressure distributions. *Medical engineering & physics*. **28**(**5**), 395–404.

Gan, R.Z., Yang, F., Zhang, X. & Nakmali, D. (2011) Mechanical properties of stapedial annular ligament. *Medical Engineering and Physics*. **33**(**3**), 330–339.

Gentil, F., Parente, M., Martins, P., Garbe, C., Jorge, R.N., Ferreira, A. & Tavares, J.M.R.S. (2011) The influence of the mechanical behaviour of the middle ear ligaments: a finite element analysis. *Proceedings of the Institution of Mechanical Engineers. Part H, Journal of engineering in medicine*. **225**(**1**), 68–76.

De Greef, D., Buytaert, J.A.N., Aerts, J.R.M., Van Hoorebeke, L., Dierick, M. & Dirckx, J. (2015) Details of human middle ear morphology based on micro-CT imaging of phosphotungstic acid stained samples. *Journal of Morphology*. **276**(**9**), 1025–1046.

Hesabgar, S.M., Marshall, H., Agrawal, S.K., Samani, A. & Ladak, H.M. (2010) Measuring the quasi-static Young's modulus of the eardrum using an indentation technique. *Hearing Research*. **263**(**1**–**2**), 168–176.

Homma, K., Du, Y., Shimizu, Y. & Puria, S. (2009) Ossicular resonance modes of the human middle ear for bone and air conduction. *The Journal of the Acoustical Society of America*. **125**(**2**), 968–979.

Huber, A., Koike, T., Wada, H., Nandapalan, V. & Fisch, U. (2003) Fixation of the anterior mallear ligament: Diagnosis and consequences for hearing results in stapes surgery. *Annals of Otology, Rhinology and Laryngology*. **112**(**4**), 348–355.

Van der Jeught, S., Dirckx, J.J.J., Aerts, J.R.M., Bradu, A., Podoleanu, A.G.H. & Buytaert, J.A.N. (2013) Full-field thickness distribution of human tympanic membrane

obtained with optical coherence tomography. *Journal of the Association for Research in Otolaryngology : JARO*. **14**(**4**), 483–94.

Kaplan, W., Wirtz, V.J., Mantel-Tweeuwisse, A., Stolk, P., Duthey, B. & Laing, R. (2013) Priority Medicines for Europe and the World - 2013 Update. Available at: http://www.who.int/medicines/areas/priority_medicines/MasterDocJune28_FINAL_Web.pdf?ua=1 [Accessed July 28, 2016].

Kelly, D.J., Prendergast, P.J. & Blayney, A.W. (2003) The effect of prosthesis design on vibration of the reconstructed ossicular chain: a comparative finite element analysis of four prostheses. *Otology & neurotology*. **24**(**1**), 11–19.

Kim, M.K., Yoon, Y.H., Park, I.Y. & Cho, J.H. (2006) Design of differential electromagnetic transducer for implantable middle ear hearing device using finite element method. *Sensors and Actuators, A: Physical*. **130**–**131**(**SPEC. ISS.**), 234–240.

Koike, T., Shinozaki, M., Murakami, S., Homma, K., Kobayashi, T. & Wada, H. (2005) Effects of Individual Differences in Size and Mobility of the Middle Ear on Hearing. *JSME International Journal Series C*. **48**(**4**), 521–528.

Koike, T., Wada, H. & Kobayashi, T. (2002) Modeling of the human middle ear using the finite-element method. *The Journal of the Acoustical Society of America*. **111**(**3**), 1306–1317.

Ladak, H.M., Decraemer, W.F., Dirckx, J.J.J. & Funnell, W.R.J. (2004) Response of the cat eardrum to static pressures: mobile versus immobile malleus. *The Journal of the Acoustical Society of America*. **116**(**5**), 3008–3021.

Ladak, H.M., Funnell, W.R.J., Decraemer, W.F. & Dirckx, J.J.J. (2006) A geometrically nonlinear finite-element model of the cat eardrum. *The Journal of the Acoustical Society of America*. **119**(**5 Pt 1**), 2859–2868.

Lagarias, J., Reeds, J., Wright, M. & Wright, P. (1998) Convergence properties of the Nelder--Mead simplex method in low dimensions. *SIAM Journal on optimization*. **9**(**1**).

Lee, C.F., Chen, J.H., Chou, Y.F., Hsu, L.P., Chen, P.R. & Liu, T.C. (2007) Optimal graft thickness for different sizes of tympanic membrane perforation in cartilage myringoplasty: a finite element analysis. *The Laryngoscope*. **117**(**4**), 725–730.

Lee, C.F., Chen, P.R., Lee, W.J., Chou, Y.F., Chen, J.H. & Liu, T.-C. (2010) Computer aided modeling of human mastoid cavity biomechanics using finite element analysis. *Eurasip Journal on Advances in Signal Processing*. **2010**.

Lee, C.L., Hsu, L.P., Chen, P.R. & Lee, C.F. (2006) Computer aided design for three-dimensional visualization and modeling of middle ear biomechanics. *Tzu Chi Medical Journal*. **18**(**6**), 416–422.

Lesser, T.H. & Williams, K.R. (1988) The tympanic membrane in cross section: a finite element analysis. *The Journal of laryngology and otology*. **102**(**3**), 209–214.

Lim, D.J. (1970) Human tympanic membrane: an ultrastructural observation. *Acta Oto-laryngologica*. **70**(**3**), 176–186.

Lim, D.J. (1968) Tympanic Membrane Part II.: Pars Flaccida. *Acta Oto-Laryngologica*. **66**(**1**–**6**), 515–532.

Mase, G.T. & Mase, G.E. (1999) *Continuum Mechanics for Engineers*, CRC Press.

Metscher, B.D. (2009) MicroCT for developmental biology: A versatile tool for high-contrast 3D imaging at histological resolutions. *Developmental Dynamics*. **238**(**3**), 632–640.

Mikhael, C. (2005) *Finite-Element Modeling of The Human Middle Ear*. McGill University.

Mikhael, C.S., Funnell, W.R.J. & Bance, M. (2004) Middle-ear finite-element modelling with realistic geometry and a priori material-property estimates. In *Proceeding of Canadian Medical and Biological Engineering Society*. p. 126–129.

Morton, N.E. (1991) Genetic epidemiology of hearing impairment. *Annals of the New York Academy of Sciences*. **630**, 16–31.

Neudert, M., Berner, M., Bornitz, M., Beleites, T., Ney, M. & Zahnert, T. (2007) Osseointegration of prostheses on the stapes footplate: Evaluation of the biomechanical feasibility by using a finite element model. *JARO - Journal of the Association for Research in Otolaryngology*. **8**(**4**), 411–421.

Parent, P. & Allen, J.B. (2010) Time-domain "wave" model of the human tympanic membrane. *Hearing Research*. **263**(**1**–**2**), 152–167.

Sadd, M.H. (2005) *Elasticity - Theory, applications, and numerics*, Burlington, MA, USA: Elsevier Butterworth–Heinemann.

Shanks, J. & Shelton, C. (1991) Basic principles and clinical applications of tympanometry. *Otolaryngologic clinics of North America*. **24**(**2**), 299–328.

Sim, J.H. & Puria, S. (2008) Soft tissue morphometry of the malleus-incus complex from micro-CT imaging. *Journal of the Association for Research in Otolaryngology*. **9**(**1**), 5–21.

Sim, J.H., Puria, S. & Steele, C. (2007) Calculation of inertial properties of the malleus-incus complex from micro-CT imaging. *Journal of Mechanics of Materials and Structures*. **2**(**8**), 1515–1524.

Stach, B.A. (2010) *Clinical Audiology: An Introduction*, Clifton Park, NY, USA: Delmar, Cengage Learning.

Standring, S. (2008) *Gray's anatomy : the anatomical basis of clinical practice*, Edinburgh: Churchill Livingstone/Elsevier.

Stieger, C., Bernhard, H., Waeckerlin, D., Kompis, M., Burger, J. & Haeusler, R. (2007) Human temporal bones versus mechanical model to evaluate three middle ear transducers. *Journal of rehabilitation research and development*. **44**(**3**), 407–415.

Sun, Q., Gan, R.Z., Chang, K.H. & Dormer, K.J. (2002) Computer-integrated finite element modeling of human middle ear. *Biomechanics and modeling in mechanobiology*. **1**(**2**), 109–122.

Takuji, K., Wada, H. & Kobayashi, T. (2001) Effect of depth of cnical-shaped tympanic membrane on middle-ear sound. *JSME International Journal*. **44**, 1097–1102.

Taschke, H., Weistenhöfer, C. & Hudde, H. (2000) A full-size physical model of the human middle ear. *Acta Acustica united with*. **86**(**1**), 103–116.

Tuck-Lee, J.P., Pinsky, P.M., Steele, C.R. & Puria, S. (2008) Finite element modeling of acousto-mechanical coupling in the cat middle ear. *The Journal of the Acoustical Society of America*. **124**(**1**), 348–362.

Ugural, A.C. & Fenster, S.K. (2003) *Advanced strength and applied elasticity*, Pearson Education.

Volandri, G., Di Puccio, F., Forte, P. & Manetti, S. (2012) Model-oriented review and multi-body simulation of the ossicular chain of the human middle ear. *Medical Engineering and Physics*. **34**(**9**), 1339–1355.

Vos, T., Barber, R.M., Bell, B., Bertozzi-Villa, A. & Biryukov, S. (2015) Global, regional, and national incidence, prevalence, and years lived with disability for 301 acute and chronic diseases and injuries in 188 countries, 1990–2013: a. *The Lancet*. **386**(**9995**), 743–800.

Wang, X., Cheng, T. & Gan, R.Z. (2007) Finite-element analysis of middle-ear pressure effects on static and dynamic behavior of human ear. *The Journal of the Acoustical Society of America*. **122**(**2**), 906–917.

Wen, Y. hsuan, Hsu, L. ping, Chen, P. rong & Lee, C. fone (2006) Design Optimization of Cartilage Myringoplasty using Finite Element Analysis. *Tzu Chi Medical Journal*. **18**(**5**), 370–377.

Zhang, X. & Gan, R.Z. (2011) Experimental measurement and modeling analysis on mechanical properties of incudostapedial joint. *Biomechanics and Modeling in Mechanobiology*. **10**(**5**), 713–726.

Zienkiewicz, O.C. & Taylor, R.L. (2000a) *The Finite Element Method: Solid Mechanics* 5th ed., Butterworth-Heinemann.

Zienkiewicz, O.C. & Taylor, R.L. (2000b) *The Finite Element Method: The Basis* 5th ed., Butterworth-Heinemann.

Zwislocki, J. (1962) Analysis of the Middle-Ear Function . Part I : Input Impedance. *The Journal of the Acoustical Society of America*. **34**(**8**), 1514–1523.

Chapter 2:
Contrast Improvement of Middle Ear Soft Tissues

The content of this chapter has been adapted from: "Iodine potassium iodide improves the contrast-to-noise ratio of micro-computed tomography images of the human middle ear", published in Journal of Microscopy, 264(3), 334-338, 2016, by S.A. Rohani, S. Ghomashchi, J. Umoh, D.W. Holdsworth, S.K. Agrawal and H. M. Ladak.

2.1 Introduction

The human middle ear includes the tympanic membrane and three bones (malleus, incus and stapes). These bones are suspended by ligaments in an air-filled cavity and are acted upon by two muscles, the tensor tympani and the stapedius muscle. The middle ear efficiently transfers sound energy collected by the outer ear to the cochlea. A list of abbreviations of anatomical features which are referred to in this work is provided in Table 2-1.

Table 2-1: List of frequently used abbreviations.

AML	Anterior mallear ligament
IMJ	Incudomallear joint
LML	Lateral mallear ligament
PIL	Posterior incudal ligament
SAL	Stapedial annular ligament
SM	Stapedius muscle and tendon
TM	Tympanic membrane
TTM	Tensor tympani muscle and tendon

Over the past few decades, several groups have been investigating the mechanics of the middle ear using computational modeling techniques such as finite-element modeling. Well-validated finite-element models of the human middle ear could improve our

understanding of the complex mechanism of hearing and could be utilized for optimizing methods for diagnosis or treatment of hearing losses *in silico* (Daniel et al., 2001). To define finite-elements models, the geometry of the middle ear must be acquired. Because of the small size of structures in the middle ear, it is difficult to image.

There are mainly two sources used for obtaining the geometry of the middle ear: serial histological sectioning (Sun et al., 2002; Gan et al., 2004; Wang et al., 2007) and micro-imaging techniques. In histological sectioning, the specimen is chemically processed to form a hard composite of the temporal bone in a medium, which can then be sectioned. This process is destructive, time-consuming and requires extensive labour. The advantages of the cumbersome serial sectioning are that cells and osteoids can be identified.

Because of technical challenges and disadvantages of sectioning, imaging modalities have been used for micro-imaging of the middle ear. Imaging modalities mainly used for this purpose are *ex-vivo* micro-computed tomography (micro-CT) (Sim & Puria, 2008; Tuck-Lee et al., 2008; Homma et al., 2009; Buytaert et al., 2011; Elkhouri et al., 2006) and *in-vivo* computed tomography (Wen et al., 2006; Lee et al., 2006). The resolution that *in-vivo* CT can currently reach is about 600 µm which is at least three times the thickness of the TM (at its thickest region); therefore, micro-CT imaging has become the more common technique for obtaining the geometry of the middle ear. Although micro-CT is widely used for imaging the middle ear, it is difficult to visualize soft tissues because of low contrast.

One way to improve the contrast of soft tissues in micro-CT is by using contrast agents. The most common contrast agents for staining soft tissues when using micro-CT imaging are osmium tetroxide, phosphotungstic acid (PTA), iodine in ethanol (I2E) and iodine

potassium iodide (IKI) (Metscher, 2009b). Since osmium tetroxide has low penetration rate and depth, is toxic and is hard to dispose of (Metscher, 2009a) other contrast agents are often preferred. PTA has been used to visualize middle-ear morphology when using micro-CT (Buytaert et al., 2014; De Greef et al., 2015). To the best knowledge of the authors, there is no work *quantifying* the effect of staining agents on the contrast of middle-ear soft tissues.

The objective of this work is to quantify the contrast-to-noise ratio of middle-ear soft tissues in micro-CT images after staining with IKI. In this study, IKI is selected because it is readily available, cost effective, not potentially corrosive like PTA and has better staining results than I2E (Metscher, 2009b).

2.2 Materials and Methods

2.2.1 Sample Preparation

Three pairs of fresh-frozen adult cadaveric temporal bones were used in this study. Cadaveric materials were donated to Western University for the purposes of medical education and research. Permission was granted for the use of the cadaveric temporal bones in the present study. The micro-CT device which has been used in this study can only be applied to small samples; therefore, following thawing, a cylindrical cutter having a 40 mm diameter and 60 mm length was used to harvest the middle ear from the temporal bones. Using this cutter had the added benefit of keeping sample dimensions consistent, which is important in terms of reagents used for fixation and staining. A sample harvested middle ear is shown in Figure 2-1.

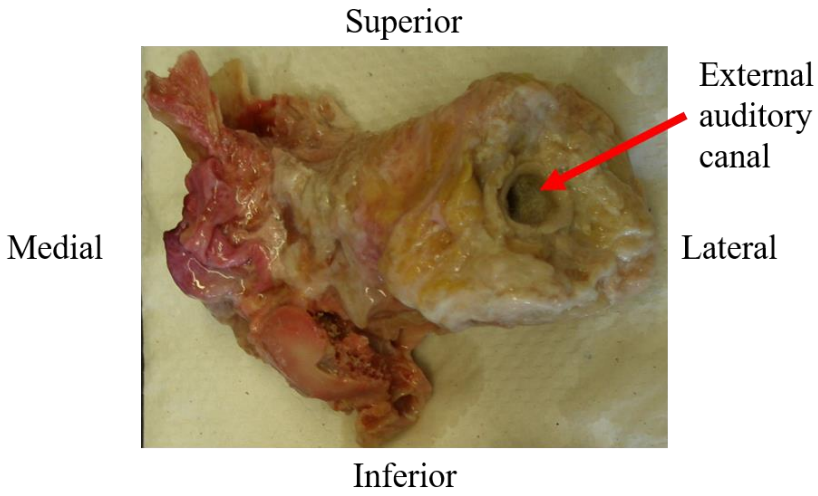

Figure 2-1: Left ear sample. A cylindrical sample was cut from the temporal bone. The sample includes the bony part of ear canal, the middle ear and the inner ear.

All 6 samples were first fixed in a 4F1G (3.7% formaldehyde + 1% gluteraldehyde in phosphate buffer) bath for 5 days to avoid decomposition. 4F1G was used as fixative in this study because of the combined advantages of faster penetration of formaldehyde and rapid fixing action of gluteraldehyde (Metscher, 2009a). Furthermore, one ear from each pair (total of 3 samples) was stained using commercially available 1% IKI solution (Sigma Aldrich, St Louis, MO, USA) for 2 days. The other ear of each pair was kept unstained. A hole with 2 mm diameter was drilled into the middle-ear cavity to ensure maximum stain uptake by soft tissues. For proper fixation and staining of samples, 1 L of solution was used for each sample to maintain the suggested 20:1 volume ratio (Skinner & Hickmon, 1997). The samples were rinsed twice, and to ensure no IKI residue remained on the soft tissues, all bones were dehydrated using an ethanol series consisting of 8 stages (50%, 60%, 70%, 80%, 90%, 95%, 100% and 100%). At each stage, the sample was immersed in 300 mL of solution for 30 minutes.

2.2.2 Imaging

All samples, 3 stained and 3 unstained, were imaged using an eXplore Locus micro-CT scanner (GE Healthcare Biosciences, London, Ontario, Canada) at the Robarts Research Institute in London, ON. The samples were scanned in air in order to improve the contrast-to-noise ratio of the soft tissues in the middle ear since air has lower intensity than ethanol or saline. The scanner operated with an x-ray voltage of 80 kV and a current of 0.45 mA. Using an angular increment of 0.4 degrees, 900 views of data were acquired. At each view, the object was exposed for about 4.5 s per frame and an average of 5 frames was taken to increase the signal-to-noise ratio. A modified conebeam algorithm (Feldkamp et al., 1984) was used to reconstruct the data into a 3D image volume at an isotropic voxel size of 20 μm. In order to make comparison of the images easier, the image of each stained sample (left ear) was mirrored against the mid-sagittal plane. All image datasets were aligned to have similar orientation. A volume of interest consisting of 500 slices was selected to span the entire middle ear.

2.2.3 Post-processing

Images of the stained and unstained samples were compared by computing contrast-to-noise ratios (CNRs) of the soft tissues of interest. The raw grey-scale values were linearly mapped to lie in the range of 0 to 255. Each mapped value was treated as a floating point number. We focused on the AML, IMJ, LML, PIL, SAL, SM, TM and TTM because these structures are of interest in finite-element models. The CNR of each soft tissue was calculated for each image using the following formulae (Bushberg et al., 2003):

$$CNR = \frac{\bar{I}_{\text{soft tissue}} - \bar{I}_{\text{space}}}{\sigma_{\text{space}}} \qquad \text{Equation 2.1}$$

where $\bar{I}_{\text{soft tissue}}$ is the mean grey-scale value for the soft tissue of interest, $\bar{I}_{\text{space}}$ is the mean grey-scale value for air in the middle-ear space and σ_{space} is the corresponding standard deviation. The voxels which were used for calculating $\bar{I}_{\text{soft tissue}}$ and $\bar{I}_{\text{space}}$ were segmented in the MIPAV (Medical Image Processing, Analysis, and Visualization**)** software (National Institutes of Health, USA). The segmentations were performed using a combination of automatic and manual techniques. First, air was segmented by manually selecting a threshold from the image histogram and classifying all pixels below the threshold as air. The threshold was taken be between the first histogram peak and the second peak. Soft tissues were then segmented using the "paint-grow" tool in MIPAV. In a few instances, the paint-grow tool resulted in a non-smooth boundary because of misclassification errors. Since these errors occurred infrequently (<10% of boundary pixels were misclassified), the boundaries were adjusted manually in these areas.

In order to compare the two datasets, i.e. stained and unstained, two statistical tests were performed. First, a Welch's t-test was used to compare the CNRs of the stained and unstained soft tissues. For this comparison, a total of n = 24 stained soft-tissue samples (3 specimens x 8 tissues types as listed in Table 2-1) were compared to n = 24 unstained samples, i.e., all of the tissue types were grouped together as either stained or unstained. Second, for *each* soft tissue, a paired t-test was used to check the effect of staining on CNR values. For this test, there are n = 3 stained samples of any one tissue type as listed in Table 2-1 and n = 3 unstained samples. In this work $p < 0.05$ was considered to indicate a significant difference between stained and unstained samples.

2.3 Results

A quantitative comparison of grey-scale values of the soft tissues in the stained and unstained samples is given in Table 2-2. "Space" refers to air in the middle ear. Mean grey-scale values for all soft tissues were higher in the stained sample when compared to the corresponding unstained sample. The highest increase was observed in larger components such as the TM and TTM while the smallest changes were found for smaller soft tissues such as the SAL.

Table 2-2: Mean and standard deviation of grey-scale values for middle-ear space and soft tissues for unstained and stained samples. Note that the raw grey-scale values were linearly mapped to lie in the range of 0 to 255. Each mapped value was treated as a floating point number. The increase in contrast of all soft tissues in the stained samples relative to their unstained counterparts is significant at the $p < 0.05$ level.

	Pair 1		Pair 2		Pair 3	
	Unstained	*Stained*	*Unstained*	*Stained*	*Unstained*	*Stained*
Space	39.9 ± 10.4	40.2 ± 10.8	39.1 ± 10.9	44.7 ± 10.2	37.7 ± 9.7	37.1 ± 10.2
AML	98.3 ± 16.1	120.1 ± 21.4	96.7 ± 16.7	135.3 ± 24.0	125.3 ± 28.7	164.5 ± 20.6
IMJ	128.7 ± 31.8	138.8 ± 22.9	154.1 ± 31.7	162.3 ± 35.1	171.2 ± 27.3	183.5 ± 29.4
LML	91.2 ± 10.5	107.7 ± 15.9	79.3 ± 10.2	107.3 ± 18.6	77.9 ± 9.2	105.0 ± 17.0
PIL	105.0 ± 15.2	114.8 ± 19.2	104.0 ± 11.8	117.6 ± 16.3	107.6 ± 21.8	126.2 ± 17.9
SAL	127.9 ± 25.3	141.9 ± 23.6	154.6 ± 26.4	173.9 ± 16.2	141.8 ± 26.3	159.4 ± 19.3
SM	87.5 ± 10.3	99.6 ± 13.4	79.8 ± 8.4	100.7 ± 19.8	83.1 ± 15.8	105.7 ± 30.1
TM	68.5 ± 14.8	96.6 ± 22.1	69.2 ± 15.5	89.4 ± 21.3	63.7 ± 12.6	91.2 ± 22.3
TTM	81.1 ± 12.9	105.9 ± 16.3	79.7 ± 13.5	131.7 ± 29.1	73.3 ± 9.1	120.6 ± 40.3

The contrast of all soft tissues in the unstained and stained images is visually illustrated in Figure 2-2. The contrast improvement was visually easiest to observe in large soft tissues, such as the TM or the TTM, in which the highest increase of mean grey-scale value was found.

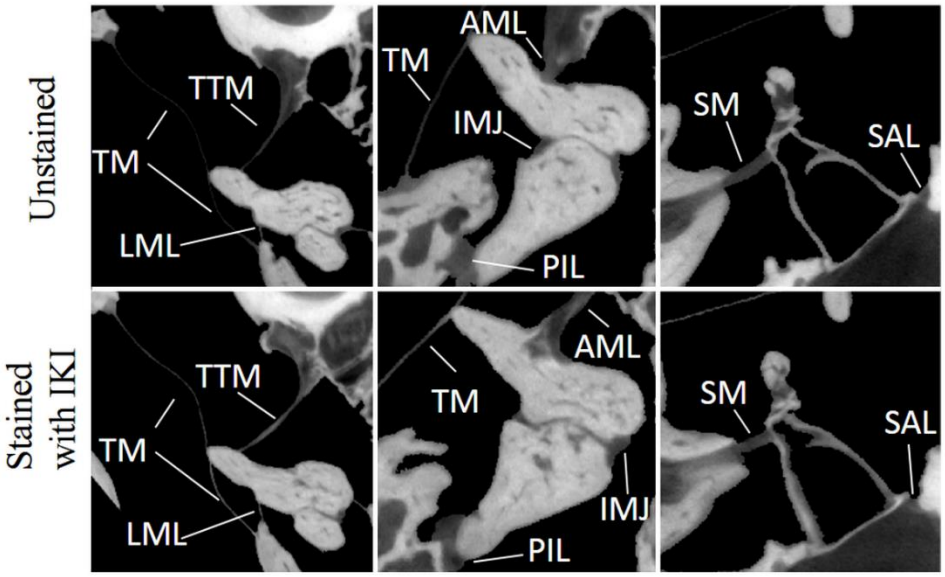

Figure 2-2: Micro-CT image slices of unstained and stained samples. The contrast of all soft tissues were increased by staining, but the effect is easiest to distinguish for larger soft tissues such as the TM and the TTM.

Corresponding CNRs were computed based on the data in Table 2-2. The pool of 24 stained soft tissues had a CNR of 8.1 ± 2.7, whereas the unstained pool had a CNR of 6.1 ± 3.0; the increase in CNR after staining was statistically significant. Also, the results from the paired t-tests for each soft tissue are given in Figure 2-3. In all soft tissues, the increase in the CNRs after staining was statistically significant.

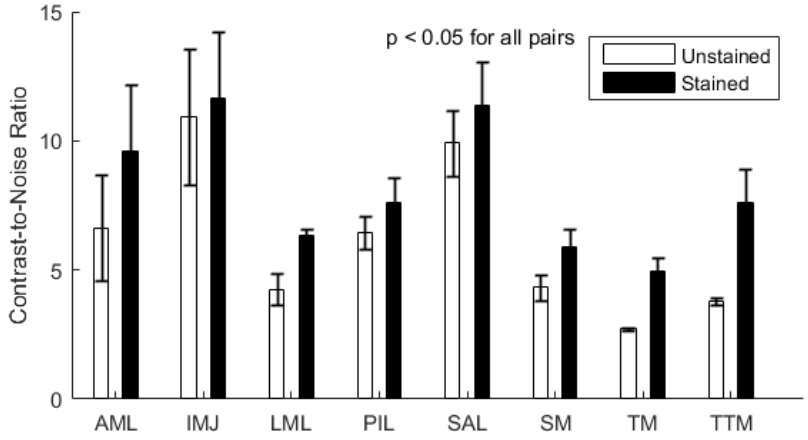

Figure 2-3: Mean and standard deviation of CNRs for soft tissues in the middle ear. A paired t-test was used to compare the CNRs of soft tissues in stained and unstained samples (n = 3).

2.4 Discussion

After staining, the numerical CNR values of all middle-ear soft tissues were improved, and these changes were statistically significant ($p < 0.05$). The statistical power analysis study is provided in Appendix A. This improvement was more easily visualized in larger soft tissues such as the TM and the TTM. The lower numerical and visual change of CNR in the SM, PIL, IMJ and SAL could be because of their smaller size which results in less contact area with the IKI solution that could affect the absorption of IKI. In addition, we observed a general increase of standard deviation of soft-tissue grey-scale values in the stained images. This could indicate variability of IKI binding.

Although the visual effect of one staining agent (PTA) on the middle-ear soft tissues has been studied in the literature, no study has reported the CNRs and/or grey-scale values in stained and unstained samples, making quantitative comparisons impossible. Such numerical data would be important for guiding algorithms for automated model generation from images such as those proposed in the literature (Ferreira et al., 2014).

An alternative approach to staining for simultaneously visualizing soft tissues and bones involves combining data from two imaging modalities. Buytaert et al. combined data from high-resolution micro-CT recordings with data from high-resolution orthogonal-plane fluorescence optical-sectioning microscopy (OPFOS) (Buytaert et al., 2011). OPFOS is an optical technique with very high resolution and can be used to visualize both soft tissues and bone if the structures can be made transparent. This particular combination is challenging to use and requires substantial amount of chemical processing to make all tissues transparent for OPFOS imaging which may not be suitable for developing sample-

specific finite-element models because such processing can result in morphological changes (Buytaert et al., 2014).

One possible disadvantage of using IKI as a staining agent is the potential for tissue shrinkage. In rabbits, it has been shown that an unconstrained block of thigh muscle shrinks after staining, with the effect being more pronounced for IKI staining compared to PTA staining (Buytaert et al., 2014). In the intact middle ear, the soft tissues are constrained by bones and one might expect this to have a smaller effect on overall morphology. Indeed, it has been shown that PTA changes the configuration of middle-ear joints by only 1° (De Greef et al., 2015).

2.5 Conclusion

The efficacy of IKI as a contrast-enhancement agent for micro-CT imaging of the human middle ear was quantitatively investigated in this study. Comparison of CNRs of middle-ear soft tissues in stained and unstained samples demonstrated significant improvement of contrast in the stained samples. IKI staining is not corrosive and is less toxic than other staining methods, which are important features when handling IKI. Moreover, IKI staining could potentially aid the automation of image-based model generation algorithms that require high contrast; moreover, quantification of mean grey-scale values and variations in them provides necessary parameters for the successful application of such algorithms.

2.6 Acknowledgements

Financial support was provided by the Natural Sciences and Engineering Research Council of Canada (NSERC), Medtronic of Canada Ltd., and the Ontario Research Fund (ORF).

2.7 References

Bushberg, J.T., Seibert, J.A., Leidholdt, E.M., Boone, J.M. & Goldschmidt, E.J. (2003) Image Quality. In The Essential Physics of Medical Imaging. Philadelphia, PA, USA: Lippincott Williams & Wilkins, p. 91.

Buytaert, J.A.N., Salih, W.H.M., Dierick, M., Jacobs, P. & Dirckx, J.J.J. (2011) Realistic 3D computer model of the gerbil middle ear, featuring accurate morphology of bone and soft tissue structures. Journal of the Association for Research in Otolaryngology. 12(6), 681–696.

Buytaert, J., Goyens, J., De Greef, D., Aerts, P. & Dirckx, J. (2014) Volume Shrinkage of Bone, Brain and Muscle Tissue in Sample Preparation for Micro-CT and Light Sheet Fluorescence Microscopy (LSFM). Microscopy and Microanalysis. 20(4), 1208–1217.

Daniel, S.J., Funnell, W.R.J., Zeitouni, A.G., Melvin, D., Daniel, S.J., Funnell, W.R.J., Zeitouni, A.G., Schloss, M.D. & Rappaport, J. (2001) Clinical Application of a Finite-Element Model of the Human Middle Ear. The Journal of Otolaryngology. 30(6), 340.

Elkhouri, N., Liu, H. & Funnell, W.R.J. (2006) Low-frequency finite-element modeling of the gerbil middle ear. Journal of the Association for Research in Otolaryngology. 7(4), 399–411.

Feldkamp, L.A., Davis, L.C. & Kress, J.W. (1984) Practical cone-beam algorithm. Journal of the Optical Society of America A. 1(6), 612–619.

Ferreira, A., Gentil, F. & Tavares, J.M.R.S. (2014) Segmentation algorithms for ear image data towards biomechanical studies. Computer Methods in Biomechanics and Biomedical Engineering. 17(8), 888–904.

Gan, R.Z., Feng, B. & Sun, Q. (2004) Three-dimensional finite element modeling of human ear for sound transmission. Annals of Biomedical Engineering. 32(6), 847–859.

De Greef, D., Buytaert, J.A.N., Aerts, J.R.M., Van Hoorebeke, L., Dierick, M. & Dirckx, J. (2015) Details of human middle ear morphology based on micro-CT imaging of phosphotungstic acid stained samples. Journal of Morphology. 276(9), 1025–1046.

Homma, K., Du, Y., Shimizu, Y. & Puria, S. (2009) Ossicular resonance modes of the human middle ear for bone and air conduction. The Journal of the Acoustical Society of America. 125(2), 968–979.

Lee, C.L., Hsu, L.P., Chen, P.R. & Lee, C.F. (2006) Computer aided design for three-dimensional visualization and modeling of middle ear biomechanics. Tzu Chi Medical Journal. 18(6), 416–422.

Metscher, B.D. (2009a) MicroCT for comparative morphology: simple staining methods allow high-contrast 3D imaging of diverse non-mineralized animal tissues. BMC physiology. 9(11).

Metscher, B.D. (2009b) MicroCT for developmental biology: A versatile tool for high-contrast 3D imaging at histological resolutions. Developmental Dynamics. 238(3), 632–640.

Sim, J.H. & Puria, S. (2008) Soft tissue morphometry of the malleus-incus complex from micro-CT imaging. Journal of the Association for Research in Otolaryngology. 9(1), 5–21.

Skinner, R.A. & Hickmon, S.G. (1997) Decalcified bone: twenty years of successful specimen management. Journal of …. 20(3), 267–277.

Sun, Q., Gan, R.Z., Chang, K.H. & Dormer, K.J. (2002) Computer-integrated finite element modeling of human middle ear. Biomechanics and modeling in mechanobiology. 1(2), 109–122.

Tuck-Lee, J.P., Pinsky, P.M., Steele, C.R. & Puria, S. (2008) Finite element modeling of acousto-mechanical coupling in the cat middle ear. The Journal of the Acoustical Society of America. 124(1), 348–362.

Wang, X., Cheng, T. & Gan, R.Z. (2007) Finite-element analysis of middle-ear pressure effects on static and dynamic behavior of human ear. The Journal of the Acoustical Society of America. 122(2), 906–917.

Wen, Y. hsuan, Hsu, L. ping, Chen, P. rong & Lee, C. fone (2006) Design Optimization of Cartilage Myringoplasty using Finite Element Analysis. Tzu Chi Medical Journal. 18(5), 370–377.

Chapter 3:
Estimation of Human Pars Tensa Young's Modulus

The contents of this chapter are submitted to: Hearing Research, as "Estimation of the Young's Modulus of the Human Pars Tensa Using In-Situ Pressurization and Inverse Finite-Element Analysis", by S. A. Rohani, S. Ghomashchi, S. K. Agrawal, H.M. Ladak, on July 15, 2016.

3.1 Introduction

The human middle ear plays a significant role in the complex hearing mechanism by transmitting sound from the environment to the cochlea. The tympanic membrane (TM) is a key component in efficiently transferring sound energy. It is anatomically divided into two major parts: the pars tensa (PT) and the pars flaccida (PF). In humans, the PT is a thin fibrous conical membrane that represents most of the surface area of the TM and is thought to play a larger role in sound transmission than the PF. By contrast, the PF is a thicker but more compliant portion of the TM with minor effects on sound transmission (Aritomo et al., 1988).

In addition to responding to dynamic acoustic stimuli in the frequency range of [20, 20k] Hz, the human ear responds to quasi-static pressure variations. Often the pressure changes at frequencies lower than 20 Hz are termed quasi-static (Dirckx et al., 2013). Quasi-static pressure changes often occur in daily life such as when using an elevator or an airplane. Quasi-static pressures are also intentionally applied in hearing tests such as tympanometry. In one form of this diagnostic procedure, the acoustic admittance of the middle ear is

measured at the TM using a probe tone of a fixed frequency (e.g., 226 Hz) while the pressure in the ear canal is quasi-statically swept in the range of -3 kPa to +2 kPa. The interpretation of tympanometric data is difficult when multiple diseases affect the middle ear (Fowler & Shanks, 2002). High fidelity finite-element (FE) models of the middle ear could be utilized to interpret and even improve such auditory tests (Daniel et al., 2001). However, accurate values for the mechanical properties of middle-ear structures are crucial for FE modelling. As the PT covers almost the entire TM in humans (Volandri et al., 2011), this work focuses on the Young's modulus of the PT as it is significant contributor to the function of the middle ear.

The mechanical properties of the human PT have been estimated using three major approaches: (1) applying tensile or bending tests on strips of the tissue cut from the PT [e.g. (Cheng et al., 2007)], (2) inverse FE modeling of experimental data obtained using indentation techniques [e.g. (Daphalapurkar et al., 2009; Aernouts et al., 2012)] and (3) by estimating the properties using measured TM collagen fibre density and size [e.g. (Fay et al., 2005)]. Note that the third approach reports on the collagen fibre layers only. Recently published values for the human PT Young's modulus [e.g., (Aernouts et al., 2012)] are smaller than previously reported estimates, motivating further investigation of the effects of modeling assumptions on estimates obtained using inverse methods.

An alternative to the approaches mentioned above has been developed in our laboratory and has been validated on phantoms but has only been applied to the rat PT (Ghadarghadar et al., 2013), not the human PT. In this technique, the TM shape is acquired before and after pressurization. An FE model specific to the TM is then generated from the shape imaged before pressurization and the model Young's modulus is numerically optimized

until the simulated deformed shape of the PT portion of the TM matches the experimentally acquired shape.

The objective of this work is to apply the pressurization approach to estimate the Young's modulus of the human PT. The intent in this work is to test the fit of FE models with geometric nonlinearity but with linearly elastic PT for low static pressures where such assumptions may be reasonable (Ladak et al., 2006). This work contributes to the body of literature on this topic in three ways. First, the inverse FE modelling approach using pressurization data has never been applied to the *human* PT. Second, it provides additional estimates of the Young's modulus under quasi-static conditions and differing loading conditions that could potentially be used to understand the large range of Young's moduli values published in the literature. Third, it demonstrates that a spatially varying Young's modulus in FE models can improve their fit to measured data.

3.2 Methods

3.2.1 Sample Preparation

Three fresh-frozen adult cadaveric temporal bones, TB1, TB2, TB3, with healthy TMs were used in this study. Cadaveric materials were donated to Western University for the purposes of medical education and research. Permission was granted for the use of the cadaveric temporal bones in the present study. Following thawing using saline, a cylindrical cutter having a 40 mm diameter and 60 mm length was used to harvest the middle ear from the temporal bones. This sample size was necessary for further imaging and provided convenient handling for the pressurization experiment.

As one of the imaging techniques used in this work (see Section 3.2.2) requires a view of the TM, the cartilaginous ear canal was resected and most of the bony external ear canal was drilled away to expose the TM as much as possible. As the middle ear is pressurized in this experiment (see Section 3.2.2), care must be taken not to accidentally create air leaks; hence, when drilling away the ear canal, 2 mm of the bony part of the ear canal, including soft tissues, were untouched. Then, an opening was made into the middle-ear air space through the superior middle-ear wall leaving the entire ossicular chain and cochlea intact. This opening was made to first immobilize the mallear head using dental cement (Prime Dental Man. Inc., IL, USA) and second to insert a pressurization tube. The former was done to isolate the deformation of the TM from the rest of the middle ear (Ladak et al., 2006; Liang et al., 2016). The latter involved inserting a tube with 1.57-mm inside diameter into the middle-ear cavity through this hole. To seal possible air leakage from the air cells in the temporal bone which changes the middle-ear pressure, dental plaster (K-Dental Inc., ON, Canada) was used to cover the air cells. During sample preparation and pressurization testing, samples were kept moist with an ultrasonic humidifier (AIR-O-SWISS, Widnau, Switzerland).

3.2.2 Experimental Procedure

In this study, the shape of each sample TM before and after pressurization was imaged. The experimental setup includes a custom-built pressurization unit (Figure 3-1) and a Fourier transform profilometer (FTP) (model MM-25D from Opton Company Limited, Seto, Aichi, Japan), a non-contacting optical device for imaging the surface shape of an object. In contrast to previous studies, no coating was applied to the TM in this study as the TM has adequate reflection for optical imaging (Das et al., 2015).

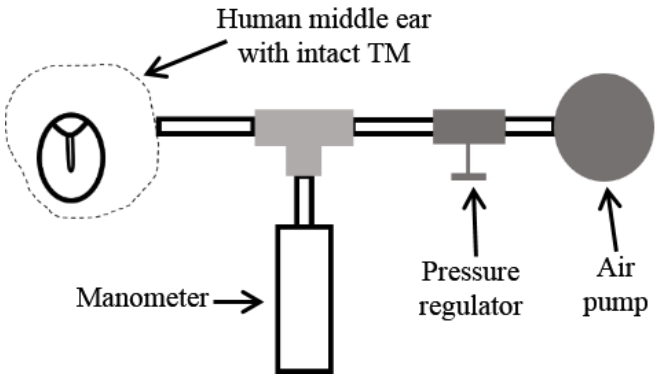

Figure 3-1: Schematic of the set-up used to apply static pressure on human TM.

Each prepared specimen was secured in a holder, and the TM's shape was measured before applying pressure. In order to obtain repeatable shape measurements, three cycles of pressurization going from rest (0 Pa) to 500 Pa and back to rest were applied to precondition the TM. Each pressurization cycle was applied in approximately 10 seconds. The shape measured at 500 Pa in the third cycle was used for subsequent analysis. In this study the response to negative pressures was not modelled because of TM mechanical instability in the mallear fixation case as discussed in previous work (Ladak et al., 2006). A pressure of 500 Pa in the middle-ear cavity can cause an area change in the PT of up to about -1.5% (Dirckx & Decraemer, 1992). At such strain, the PT can be modeled as a linearly elastic material that can be characterised by a Young's modulus and Poisson's ratio.

The profilometer used in this study has a height measurement accuracy of 10 µm and an in-plane resolution of 27 µm. Its output is a dense cloud of points in 3D space that represents the shape of the surface being measured. The deformation of the TM measured using FTP ($\Delta Z_{x,y}^{FTP}$) is calculated using the equation:

$$\Delta Z_{x,y}^{FTP} = Z_{x,y}^{FTP,P} - Z_{x,y}^{FTP,0} \qquad \text{Equation 3.1}$$

where $Z_{x,y}^{FTP,P}$ is the height of the TM surface at the point (x, y) when pressurized and $Z_{x,y}^{FTP,0}$ is the height of the TM surface at the same (x,y) while the sample is at rest (i.e.,

unpressurized). All heights were measured relative to the XY-plane defined by the plane of the TM boundary.

3.2.3 Contrast-Enhanced Imaging

Since the TM periphery and malleus are not fully visible in FTP, each sample was scanned using micro-computed tomography (micro-CT) after the pressurization experiment. The samples were first fixed using formaldehyde solution to avoid degradation, and to improve the contrast of the TM in the micro-CT images, they were then stained using iodine potassium iodide prior to imaging; details of the fixation and staining procedure are given elsewhere (Rohani et al., 2016). To avoid deformation of the soft tissues in the middle ear, the samples were kept moist during the scan by holding them in a plastic container with a layer of water at the bottom (De Greef et al., 2015).

All samples were imaged using an eXplore Locus micro-CT scanner (GE Healthcare Biosciences, London, Ontario, Canada) at the Robarts Research Institute in London, ON. The scanner operated with an x-ray voltage of 80 kV and a current 92 of 0.45 mA. Using an angular increment of 0.4 degrees, 900 views of data were acquired. At each view, the sample was exposed for about 4.5 s per frame and an average of 5 frames was taken to increase the signal-to-noise ratio. A modified conebeam algorithm (Feldkamp et al., 1984) was used to reconstruct the data into a 3D image volume at an isotropic voxel size of 20 μm. A volume of interest consisting of 500 slices was selected to span the entire middle ear. A sample 2D image slice from the 3D image volume is shown in Figure 3-2.

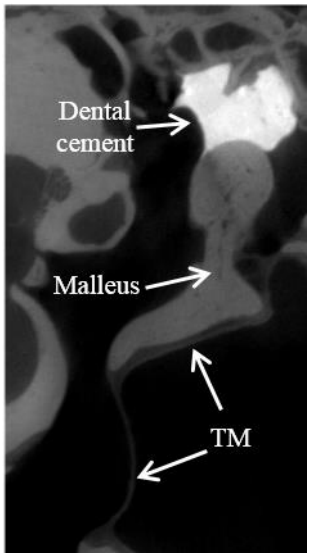

Figure 3-2: Representative 2D image slice from 3D micro-CT image volume of TB1. The malleus, TM and dental cement are clearly visible in the images.

3.2.4 FE Model Generation

For each sample, the geometry of the TM was modeled from FTP data recorded at its resting position (unpressurized). As mentioned before, ossicular chain and the boundaries of the TM including annular ring are not visible in FTP. Therefore, the TM boundary, malleus and dental cement were manually segmented from micro-CT volumes using the MIPAV (Medical Image Processing, Analysis, and Visualization) software from the National Institutes of Health, USA (mipav.cit.nih.gov). In order to add the TM boundary and malleus to the model from FTP, the micro-CT model was aligned to FTP data using least-square landmark-based registration. The landmarks used in registration were situated along the manubrium, including umbo and lateral process.

This resulted in one triangulated mesh for the TM, one for the malleus and one for the dental cement. Furthermore, for the TM and the malleus, NURBS (non-uniform rational B-spline) patches were fitted in Geomagic Studio (3D Systems Inc., SC, USA) as this representation is required for the FE meshing procedure. The dental cement was not

converted to NURBS and was only segmented to provide the exact location of where to apply the boundary condition for FE modeling as discussed below.

All models were imported into COMSOL Multiphysics (COMSOL Inc., MA, USA) for meshing and FE analysis. For each sample, the malleus was meshed using tetrahedral solid elements while the TM was meshed using triangular shell elements. The TM annular ring was taken to be fully clamped. For the mallear head, the FE mesh nodes contacting the dental cement were taken to be fully clamped to simulate the experimental condition of malleus immobilization. These nodes could be identified because a triangulated surface of the dental cement was available for each specimen. The dental cement surface was only used for identifying which mallear nodes to constrain for simulation. A sample FE model is shown in Figure 3-3.

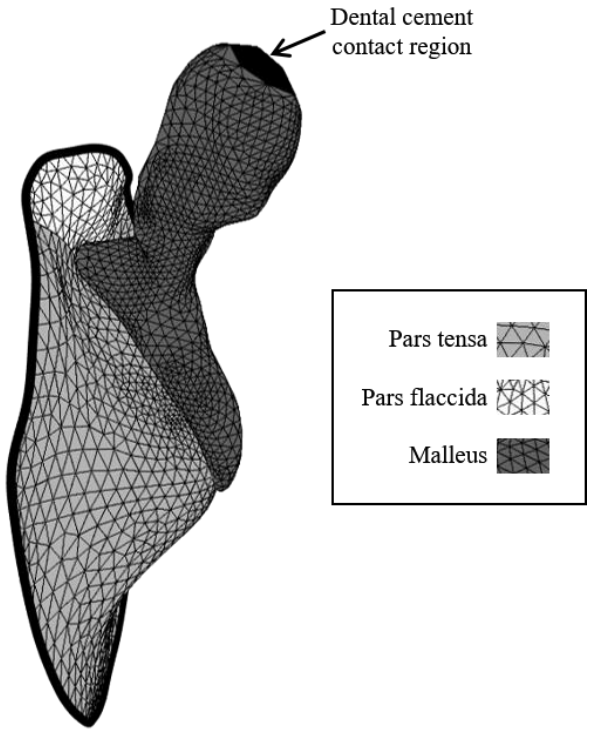

Figure 3-3: FE mesh for TB1. The tympanic ring and the portion of the mallear head in contact with dental cement were taken to be fully clamped in the FE analysis.

In this study, the FE models of the TM and malleus were considered to be isotropic, linear elastic materials. As mentioned earlier, such materials can be characterized by a Young's modulus and a Poisson's ratio. The Young's modulus of the PF was constrained to be ½ of the Young's modulus of the PT, while that of the PT was optimized. This ratio of ½ has been used in previous studies (Sun et al., 2002; Lee et al., 2010; Lee et al., 2006; Mikhael et al., 2004). The Poisson's ratio of the PT and PF were taken to be 0.49 to model incompressibility (Aernouts et al., 2010; Daphalapurkar et al., 2009; Huang et al., 2008; Elkhouri et al., 2006). The Young's modulus and Poisson's ratio of the malleus were assumed to be 14.1 GPa and 0.3, respectively as has been used in many previous studies (Gan et al., 2002; Gan et al., 2006; Lee et al., 2010; Gan & Sun, 2002; Zhang & Gan, 2011; Gentil et al., 2011; Lee et al., 2006; Wen et al., 2006). Note that viscoelastic behaviour was not considered and is a limitation of our models that requires future consideration.

In this study, standard mesh refinement and convergence procedure were followed to assure the quality of the mesh. Also, geometric nonlinearity was included in this study which is necessary when modeling thin objects such as TM that undergo large displacements.

For shell elements, like those representing the TM, thickness also needs to be specified. A constant thickness of 110 μm was used for the PT in keeping with a recent study (Aernouts et al., 2012). For the PF, a constant thickness of 220 μm was used (Lim, 1970).

3.2.5 Optimization

For each specimen the Young's modulus of the PT, denoted E_{PT}, was estimated by minimizing a cost function, $C(E_{PT})$, with respect to E_{PT}. The cost function is defined so

that a minimal value results when the deformed shape computed using the FE model for a particular specimen matches the corresponding measured shape:

$$C(E_{PT}) = \sum_{i=1}^{n} \left(Z_i^{FTP,P} - Z_i^{FE,P}(E_{PT})\right)^2 \qquad \text{Equation 3.2}$$

where $Z_i^{FTP,P}$ and $Z_i^{FE,P}$ denote the measured and simulated Z coordinates, respectively, for point i in the pressurized state. Only the n points defining the PT that are visible in FTP were taken into account in Equation 3.2.

Optimization was performed using golden section search with parabolic interpolation using the function 'fminbnd' in MATLAB R2015a (Natick, MA). This algorithm finds the minimum of a single-variable unimodal cost function given lower and upper search bounds; the unimodal nature of the cost function is shown in Appendix B. The lower search bound for optimization was set to 1 MPa and the upper bound to 300 MPa. This is a large bound that covers the range of potential values that have been used or estimated in published studies. The optimization was terminated if values of C changed by less than 0.01% between successive iterations. To ensure that a unique optimum value is reached in the given range, the initialization of the optimization algorithm was varied over two orders of magnitude. Figure 3-4 shows a schematic representation of the optimization technique.

To assess the quality, the FE model with an optimal value of E_{PT}, simulated TM deformation ($\Delta Z_{x,y}^{FE}$) was computed using the following equation and compared to measured deformation ($\Delta Z_{x,y}^{FTP}$):

$$\Delta Z_{x,y}^{FE} = Z_{x,y}^{FE,P} - Z_{x,y}^{FE,0}. \qquad \text{Equation 3.3}$$

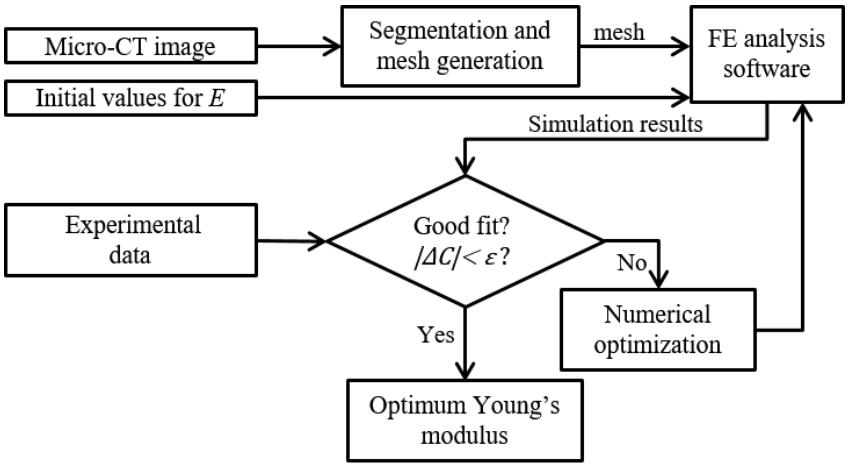

Figure 3-4: Flowchart for estimation algorithm. C is the cost function to be minimized and ε is the optimization convergence parameter.

In Equation 3.3, $Z_{x,y}^{FE,P}$ is the simulated height of the TM surface at the point (x, y) when pressurized and $Z_{x,y}^{FE,0}$ is the height of the TM surface at the same (x,y) while the sample is at rest (i.e., unpressurized). Deformations are compared instead of pressurized shapes to highlight differences between simulated results and experimental data. The differences are small relative to height values and are difficult to discern when viewing pressurized shapes, but become more apparent when viewing deformation patterns.

3.3 Results

The area changes of the PT for TB1, TB2 and TB3 due to pressurization were -0.25%, -0.31% and -1.47% based on the FTP measurement. This is in agreement with the assumption of linear elasticity which was taken into account in this study. The E_{PT} values for TB1, TB2 and TB3 estimated from sample-specific FE models were 2.2 MPa, 2.4 MPa and 2.0 MPa, respectively. Varying the initialization only caused less than 1% variation in the results. The deformations predicted by the corresponding FE models using the estimated values are shown in the top panel of Figure 3-5 for a quasi-static pressure of 500 Pa. Maximum deformation occurred in the posterior PT and was centred in the infero-

superior directions in TB1 and TB2. In TB3, the maximum also occurred in the posterior PT but was located slightly inferior to the locations in TB1 and TB2. For comparison, the corresponding measured deformations are shown in the central panel of Figure 3-5.

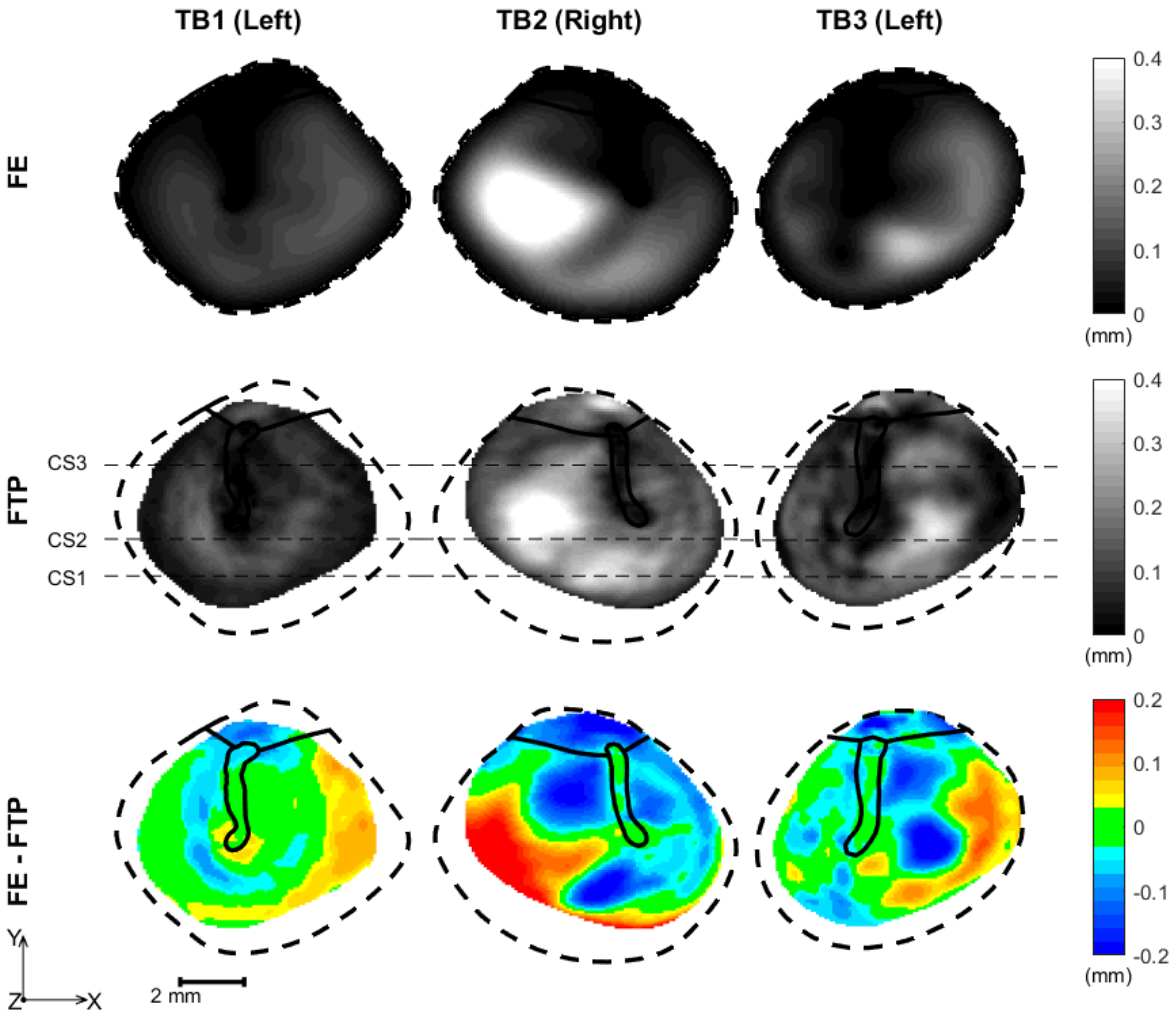

Figure 3-5: Deformation patterns at 500 Pa and error maps for samples TB1, TB2 and TB3. Top row: FE-simulated deformations. Middle row: FTP-measured deformation. Bottom row: Error maps defined as $Z^{FE,P}$ - $Z^{FTP,P}$. Anatomical directions: positive Y axis is superior direction for all three samples. Positive X axis is posterior direction for samples TB1 and TB3 and anterior direction for TB2. The dashed boundary is the annular ring which is not observed using FTP because of the overhanging ear canal. The boundary was found using micro-CT and was used to define the FE models. The dashed lines CS1, CS2, CS3 show location of cross sections given in Figure 3-6.

Qualitatively, the measured and simulated deformation patterns are similar with the maximum deformation generally occurring in approximately the same location. However,

there are differences in the magnitude of the deformations. To highlight these spatial differences in deformation magnitude, errors maps were computed between the FE simulated pressurized height ($Z^{FE,P}$) and the FTP measured height ($Z^{FTP,P}$) as $Z^{FE,P} - Z^{FTP,P}$ and are shown in the bottom panel of Figure 3-5. Positive errors indicate that the PT deformed more in the FE model than in the experiment, whereas negative errors indicate that the PT deformed less in the FE model than in the experiment. The spatial distribution of the differences varies in a specimen-specific manner.

In addition to the error maps, the differences are shown on 3 cross sections in each sample. The location of the cross sections is shown in the middle panel of Figure 5 and the cross sections are given in Figure 3-6.

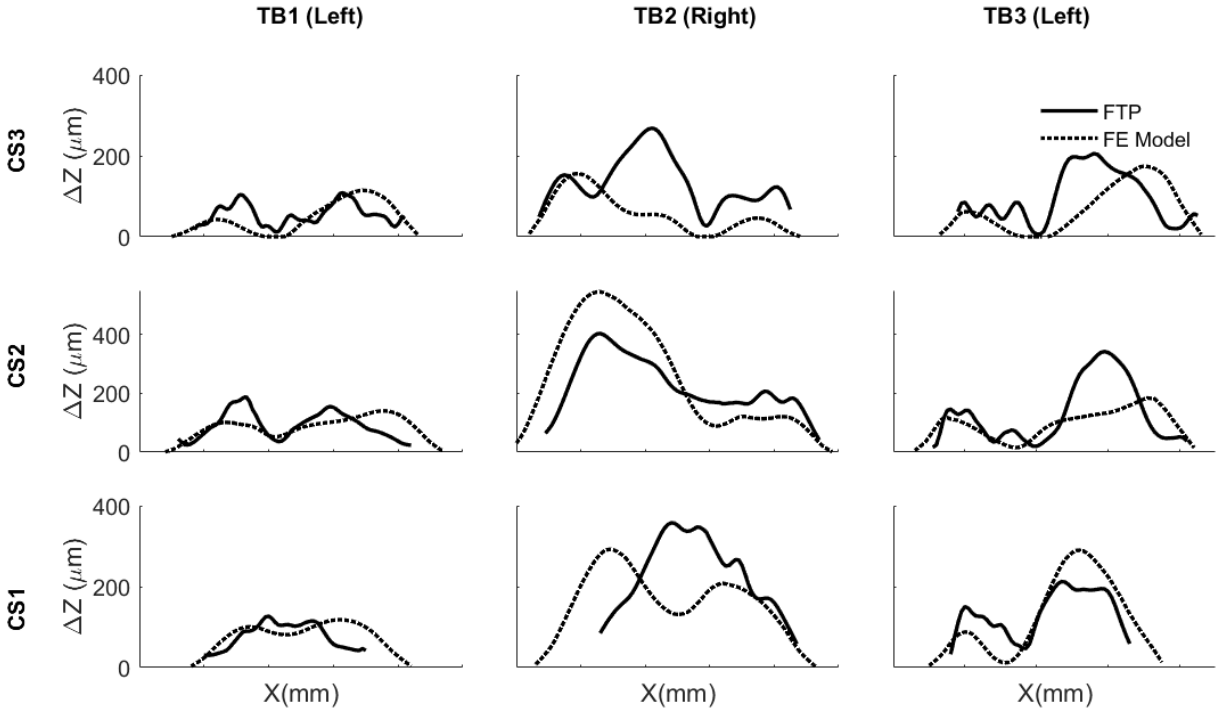

Figure 3-6: Cross sections comparing the fit of simulated FE models to experimental FTP measurements. The solid line shows the height difference calculated from FTP measurement ($Z^{FTP,P} - Z^{FTP,0}$). The dashed line shows the height difference calculated in FE model ($Z^{FE,P} - Z^{FE,0}$). The ticks along the X axis are 2 mm apart.

3.4 Discussion

3.4.1 Comparison with other studies

The estimated average value for E_{PT} in this study is 2.2±0.2 MPa which compares well with the value of 2.9±1.3 MPa that has recently been reported (Aernouts et al., 2012). In that report, *in-situ* quasi-static indentation and inverse FE modeling were used. The pressurization approach used here is similar to the indentation technique in that experiments are conducted on the intact TM and involve optimization of a subject-specific FE model. However, pressurization is simpler to apply and model than indentation for two major reasons (Ghadarghadar et al., 2013). First, during an indentation experiment, great care needs to be taken to avoid slippage between the indenter and the TM. Second, simulating the indentation experiment involves complex contact modeling. Neither slippage nor contact modeling are required when conducting a pressurization experiment.

A study that also involves experimentation on the intact TM is that by Gaihede *et al* .in which quasi-static pressures were applied to the ear canal of live subjects and volume displacements of the TM were measured (Gaihede et al., 2007). Using a model of the TM, its Young's modulus was estimated to be 10.33 ± 1.35 and 6.88 ± 0.53 MPa in younger and older populations, respectively. Although their approach can be applied *in vivo*, only a simplified model of the TM was used to estimate the Young's modulus. In particular, the TM was modeled as a flat circular membrane and the manubrium was not considered. Both the curved conical shape of the TM and ossicular/cochlear loading of the TM via the manubrium affect TM mechanics (Funnell & Laszlo, 1978; Fay et al., 2006). For comparison with other estimates, Table 3-1 summarizes the literature on human PT Young's moduli estimated by others. As noted in the introduction, there are considerable

differences between reported values. These may be due to differences in the TM thickness used when calculating the Young's modulus, differences in the experimental procedures and inter-specimen variation. Indeed, results of the current study do not agree with our previous estimates of 22.8 ± 1.5 MPa for the rat PT Young's modulus (Ghadarghadar et al., 2013; Hesabgar et al., 2010). It is not clear if this represents an inter-species difference.

Table 3-1: Summary of studies estimated mechanical properties of human PT.

Author	Approach	Thickness (μm)	Estimated Values (MPa)
Studies on tissue strips/sections			
Von Békésy & Wever, 1960	Static bending test on tissue strips as cantilevered beam	50	20
Kirikae, 1960	Longitudinal tensile testing at 890 Hz	75	40
Decraemer et al., 1980a	Longitudinal tensile testing at 300 Hz at strain rates higher than 8%	46	22.8
Cheng et al., 2007	Longitudinal tensile testing for stresses up to 1 MPa	80	0.4-22
Huang et al., 2008	Nanoindentation testing on anterior and posterior regions	70	Posterior: 17.4 Anterior: 19.0
Daphalapurkar et al., 2009	Nanoindentation testing on four anatomical quadrants of TM	60	25.7-37.8
Luo et al., 2009	Longitudinal tensile testing of tissue strips along radial and circumferential directions at strain rates 300-2000 Hz	62.5–75.4	Radial: 45.2–58.9 Circumferential: 34.1–56.8
Studies on intact TM			
Fay et al., 2005	Dynamic measurements and inverse modeling using a composite shell model (Also estimated bounds using constitutive modeling and re-interpretation of published bending and tensile tests.)	37	100-300
Gaihede et al., 2007	Estimation from *in vivo* volume-displacement data measured at 0.14 Hz	90	10.33 ± 1.35 MPa (Younger group) 6.88 ± 0.53 (older)
Aernouts et al., 2012	*in-situ* indentation of TM at single location	97-110	2.1-4.4

3.4.2 Sensitivity Analysis

The sensitivity of PT Young's modulus estimates to multiple FE modeling assumptions were investigated. This includes sensitivity to optimization initialization, PT thickness, PF Young's modulus, FTP measurement error, TM element type, inclusion of a manubrial fold, and possible spatial non-uniformity in the PT. R2-9: Changing the initial parameters

used by the optimization algorithm by two orders of magnitude only caused a 1% variation in the results.

In order to investigate the sensitivity of E_{PT} estimates to PT thickness used in our models, the thickness was varied from 37 to 110 in one model to span the range of values used in the literature. The variation of optimal E_{PT} with PT thickness is given in Figure 3-7. The estimated value of E_{PT} decreases/increases as PT thickness increases/decreases which is consistent with past studies (Aernouts et al., 2012).

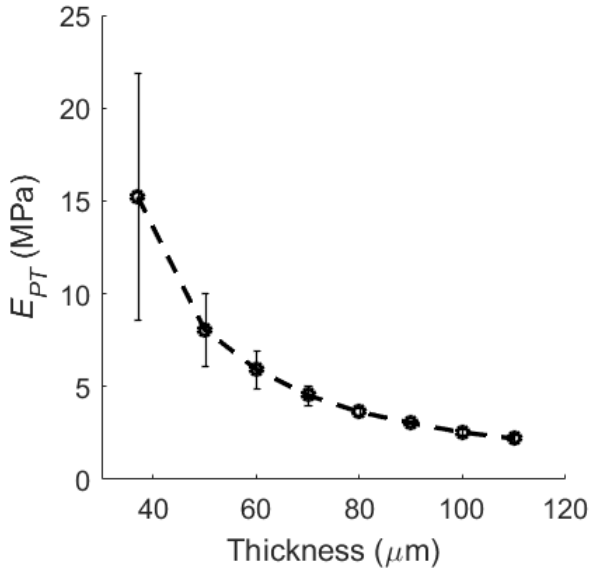

Figure 3-7: Sensitivity of E_{PT} to PT thickness.

In the optimization algorithm, the measured pressurized height values ($Z_i^{FTP,P}$) are constant and the algorithm systematically adjusts E_{PT} so simulated pressurized height values ($Z_i^{FE,P}$) match measured ones. When thickness is increased/decreased, the algorithm must adjust E_{PT} downward/upward to match the constant measured values. This observation is congruent with previous FE modeling studies which demonstrate that increasing/decreasing E_{PT} or PT thickness, decreases/increases deformation magnitude, with thickness having a more pronounced effect than E_{PT} (Funnell & Laszlo, 1978).

However, even for a model thickness value of 37 μm, the estimated E_{PT} values for TB1, TB2 and TB3 are only 10 MPa, 13 MPa and 22.7 MPa, respectively. These are smaller than some previous studies on tissue strips and for studies using dynamic stimuli.

In our previous work on the *rat* TM, it was shown that choice of PF Young's modulus does not appreciably change the estimation of PT Young's modulus (Salamati et al., 2012). As the focus in this study is on *human* TM, the effect of lowering the PF Young's modulus on estimation of PT Young's modulus was investigated. Decreasing the PF Young's modulus from the current 50% of PT Young's modulus to 5% to make it more flexible resulted in less than 2% change in the estimate of the PT Young's modulus.

Also, the possible effects of FTP measurement error were investigated. Specifically, a spatially uniform error of 10 μm in FTP height measurement ($Z_i^{FTP,P}$) was added to the original pressurized FTP data, and the PT Young's modulus was re-estimated. This resulted in an average decrease of 8% in the estimated PT Young's modulus. At the other extreme, 10 μm was subtracted from each $Z_i^{FTP,P}$ value, and this resulted in an increase in the estimated PT Young's modulus of 11%. We note that although computed PT deformation is smooth (Figure 3-6), measured deformations are not. This is caused by systematic errors in profilometry approaches and is noticeable for small deformations [e.g., (Ladak et al., 2000)]. Although this affects visualization of deformation, the cost function in Equation (3.2) is based on measured heights, not deformations.

In published studies, both shell and solid elements have been used to model the TM. Hence, the sensitivity of the estimation of PT Young's modulus to the TM element type (i.e., solid

vs shell elements) was investigated in this study. The estimated values of the PT Young's modulus changed slightly from 2.2 ± 0.2 MPa to 2.4 ± 0.1 MPa when using solid elements.

In the models, the PT is assumed to be tightly coupled to the manubrium; however, this is not the case in humans (De Greef et al., 2014; Graham et al., 1977). To investigate the effects of including the manubrial fold coupling the PT to the manubrium on estimation of the PT Young's modulus, four modeling cases were compared: wide manubrial fold and three cases of narrower manubrial folds with widths of 300 µm, 100 µm and 50 µm (see Figure 3-8). The Young's modulus of the manubrial fold was assumed to be 10% of the PT Young's modulus as suggested in the literature (De Greef et al., 2014). With a wide manubrial fold, the average estimated PT Young's modulus increased by 23% relative to a tight connection. For narrower manubrial folds, the estimates increased on average by 34%, 63% and 87% relative to the tightly coupled case when the width was set to be 300 µm, 100 µm and 50 µm, respectively.

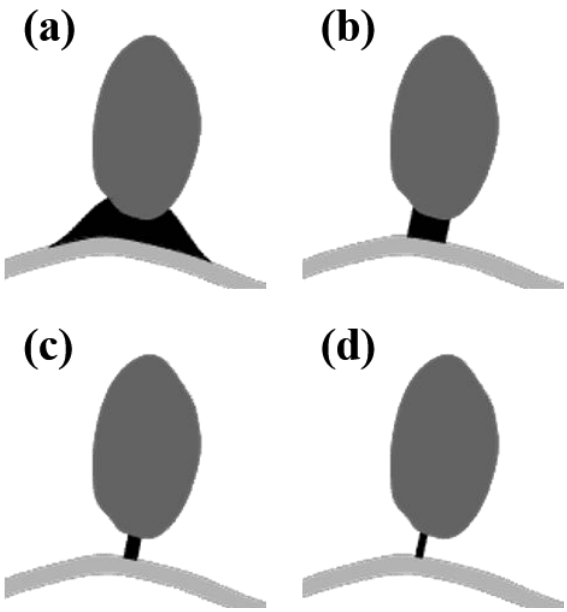

Figure 3-8: Illustration of manubrial fold connection types. (a) Wide, (b) 300 µm, (c) 100 µm, (d) 50 µm.

Table 3-1 groups the various studies into those performed on tissue strips/sections cut from the PT or those performed on intact PTs. The use of PT strips/sections could compromise the tissue's structural integrity, thus altering its mechanical properties. The orientation of the strip (radial versus circumferential) also affects results as the PT is anisotropic (Luo et al., 2009). Moreover, due to spatial non-uniformity in both PT thickness (Van der Jeught et al., 2013; Kuypers et al., 2006) and fiber distribution (Lim, 1994), E_{PT} could vary based on the location on the PT from which the strip/section was cut. Indeed, variations in E_{PT} with location have previously been demonstrated [e.g. (Daphalapurkar et al., 2009; Huang et al., 2008)]. The pressurization approach used here assumes that the eardrum is uniform across its surface, thus the estimated value of E_{PT} does not vary spatially and represents a global average. Moreover, we have assumed that the PT is isotropic. The assumptions of uniformity and isotropy have been used in other FE modeling studies [e.g. (Funnell & Laszlo, 1978; Volandri et al., 2011; Wang et al., 2007; Aernouts et al., 2012; Huang et al., 2008; Luo et al., 2009; Wada et al., 1992; Gan et al., 2002)].

Interestingly, the error maps shown in the lower panel of Figure 3-5 suggest that non-uniformity may be present in the PT. Specifically, there are regions where the FE results do not match the experimental data well using a single value of E_{PT}, even when though the optimal value is used. These poorly matched areas are where the difference $Z^{FE,P} - Z^{FTP,P}$ is non-zero. One way to improve the mismatch between simulation results and measurements is to incorporate spatial non-uniformity in parameter values, either in the PT Young's modulus or in its thickness. Model responses and therefore PT Young's modulus estimates are sensitive to thickness as noted above. Here, we investigate the effects of PT Young's modulus variations. Variations in PT Young's modulus are a possibility because

of spatial non-uniformity in the ultrastructure of the PT. For instance, transverse fibers only appear to be present in the inferior region (Shimada & Lim, 1971). For instance, for TB2 we arbitrarily increased the Young's modulus of the elements in the postero-inferior quadrant to test the effects of this change on $Z^{FE,P} - Z^{FTP,P}$. Specifically, the Young's modulus of these elements was changed to 7.2 MPa (3 times higher than the estimate of 2.4 MPa for this sample); the "optimal" value of 2.4 MPa was retained for the other elements. With this change, there is a reduction in $Z^{FE,P} - Z^{FTP,P}$ towards zero in this region as evidenced by the error map transitioning from white in the postero-inferior quadrant (see Figure 3-9a) to light grey (see Figure 3-9b).

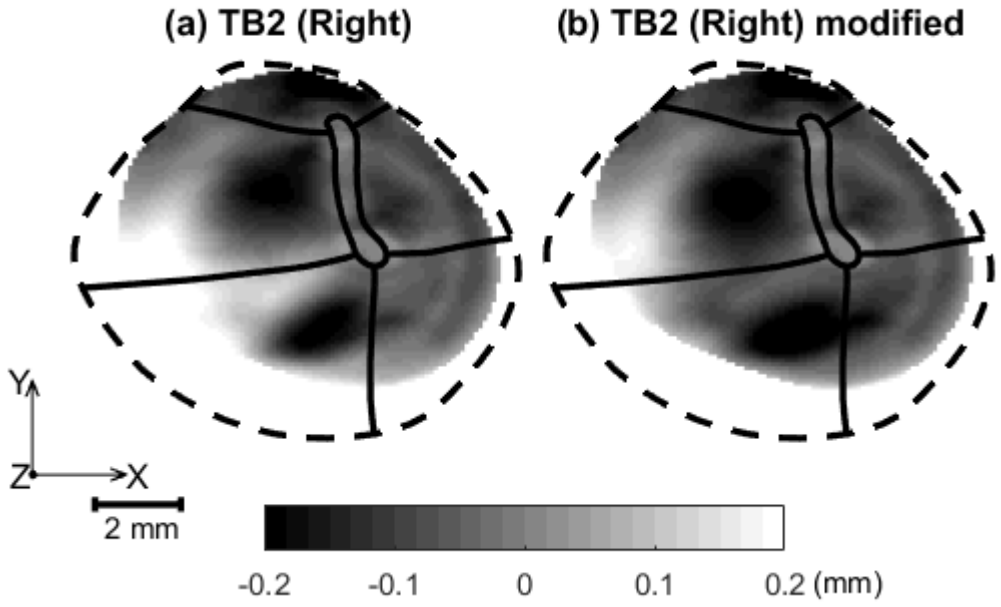

Figure 3-9: Effect of spatial non-uniformity in E_{PT} on error map, $Z^{FE,P}$ - $Z^{FTP,P}$. (a) Error map for TB2 using uniform "optimal" E_{PT} of 2.4 MPa. (b) Error map after increasing E_{PT} in postero-inferior quadrant to 7.2 MPa with all other elements remaining at 2.4 MPa. Anatomical directions: positive Y is superior direction. Positive X is anterior direction.

One could of course also vary PT thickness spatially to achieve a better match between simulated deformations and experimental data. However, in healthy ears, PT thickness

appears to be approximately uniform, but there is thickening near the manubrium and annular ring (Van der Jeught et al., 2013). This thickening is neglected in our model, since it occurs in a very narrow region of 100-300 μm, which might not affect the PT Young's modulus estimation. By contrast, there is experimental evidence of spatial non-uniformity in E_{PT} (Daphalapurkar et al., 2009).The spatial variation in E_{PT} could be estimated by allowing E_{PT} to vary spatially (e.g., from one element to the next) within the optimization framework represented by the flowchart in Figure 3-4. This would require optimization of multiple parameters which is numerically challenging (Samani et al., 2001).

On further examination of the studies in Table 3-1, we note that experimental/theoretical approaches greatly affect E_{PT} estimation. In dynamic experiments, E_{PT} varies with strain rate; specifically, E_{PT} increases with increases in strain rate as demonstrated through tensile tests in which the strain rate was systematically varied (Luo et al., 2009). This is also reflected in the higher E_{PT} values reported at 300 Hz (Decraemer et al., 1980b) and 890 Hz (Kirikae, 1960) as compared to ours, even after accounting for thickness differences. Therefore, the values reported in the current work should only be applied to quasi-static simulations.

Furthermore, our estimates are confined to the linear regime of TM function where the mechanical stresses and strains are small. At higher levels which would be induced by larger pressures, material nonlinearity becomes important and the stress-strain relationship of the PT is better characterized by hyperelastic models (Liang et al., 2016; Qi et al., 2008).

As a final note, the estimated values of E_{PT} are of use in FE models in which the PT is considered to be homogeneous and isotropic. These assumptions have been used to successfully model experimental data (Maftoon et al., 2015).

3.5 Conclusions

The Young's modulus of the human pars tensa was estimated using *in situ* quasi-static pressurization and inverse FE modeling, yielding an average value of 2.2 ± 0.2 MPa assuming a linearly elastic, uniform and isotropic pars tensa with a thickness of 110 μm. These values are similar to those estimated using *in situ* quasi-static indentation testing and inverse FE modeling under identical assumptions, but they are smaller than most published values obtained on tissue strips and/or using dynamic stimuli. Estimates of PT Young's modulus are sensitive to the PT thickness and inclusion of the manubrial fold. However, they do not appear to be sensitive to optimization initialization, FTP height measurement error, PF Young's modulus, and TM element type (shell versus solid). A locally improved match between simulation results and experimental data was shown to be achieved by incorporating spatial non-uniformity in the Young's modulus, providing impetus for developing algorithms to estimate such non-uniformities in an inverse modeling framework.

3.6 Acknowledgements

Funding for this work was provided by the Natural Sciences and Engineering Research Council of Canada.

3.7 References

Aernouts, J., Aerts, J.R.M. & Dirckx, J.J.J. (2012) Mechanical properties of human tympanic membrane in the quasi-static regime from in situ point indentation measurements. *Hearing Research*. **290**(**1**–**2**), 45–54.

Aernouts, J., Soons, J. a M. & Dirckx, J.J.J. (2010) Quantification of tympanic membrane elasticity parameters from in situ point indentation measurements: Validation and preliminary study. *Hearing Research*. **263**(**1**–**2**), 177–182.

Aritomo, H., Goode, R.L. & Gonzalez, J. (1988) The role of pars flaccida in human middle ear sound transmission. *Otolaryngology--Head and Neck Surgery*. **98**(**4**), 310–314.

Von Békésy, G. & Wever, E.G. (1960) *Experiments in hearing*, McGraw-Hill New York.

Cheng, T., Dai, C. & Gan, R.Z. (2007) Viscoelastic properties of human tympanic membrane. *Annals of Biomedical Engineering*. **35**(**2**), 305–314.

Daniel, S.J., Funnell, W.R.J., Zeitouni, A.G., Melvin, D., Daniel, S.J., Funnell, W.R.J., Zeitouni, A.G., Schloss, M.D. & Rappaport, J. (2001) Clinical Application of a Finite-Element Model of the Human Middle Ear. *The Journal of Otolaryngology*. **30**(**6**), 340.

Daphalapurkar, N.P., Dai, C., Gan, R.Z. & Lu, H. (2009) Characterization of the linearly viscoelastic behavior of human tympanic membrane by nanoindentation. *Journal of the Mechanical Behavior of Biomedical Materials*. **2**(**1**), 82–92.

Das, A.J., Estrada, J.C., Ge, Z., Dolcetti, S., Chen, D. & Raskar, R. (2015) A compact structured light based otoscope for three dimensional imaging of the tympanic membrane. In *SPIE*. p. 93031F.

Decraemer, W., Maes, M. & Vanhuyse, V. (1980a) A non-linear viscoelastic constitutive equation for soft biological tissues, based upon a structural model. *Journal of*.

Decraemer, W., Maes, M. & Vanhuyse, V. (1980b) An elastic stress-strain relation for soft biological tissues based on a structural model. *Journal of biomechanics*.

Dirckx, J.J.J. & Decraemer, W.F.S. (1992) Area change and volume displacement of the human tympanic membrane under static pressure. *Hearing Research*. **62**(**1**), 99–104.

Dirckx, J.J.J., Marcusohn, Y. & Gaihede, M.L. (2013) Quasi-static Pressures in the Middle Ear Cleft. In pp. 93–133.

Elkhouri, N., Liu, H. & Funnell, W.R.J. (2006) Low-frequency finite-element modeling of the gerbil middle ear. *Journal of the Association for Research in Otolaryngology*. **7**(**4**), 399–411.

Fay, J., Puria, S., Decraemer, W.F. & Steele, C. (2005) Three approaches for estimating the elastic modulus of the tympanic membrane. *Journal of Biomechanics*. **38**(**9**), 1807–1815.

Fay, J.P., Puria, S. & Steele, C.R. (2006) The discordant eardrum. *Proceedings of the National Academy of Sciences of the United States of America*. **103**(**52**), 19743–19748.

Feldkamp, L.A., Davis, L.C. & Kress, J.W. (1984) Practical cone-beam algorithm. *Journal of the Optical Society of America A*. **1**(**6**), 612–619.

Fowler, C.G. & Shanks, J.E. (2002) Tympanometry. In J. Katz, ed. *Handbook of Clinical Audiology*. Philadelphia, PA, USA: Lippincott Williams & Wilkins, pp. 175–204.

Funnell, W.R.J. & Laszlo, C.A. (1978) Modeling of the cat eardrum as a thin shell using the finite-element method. *The Journal of the Acoustical Society of America*. **63**(**5**), 1461–1467.

Gaihede, M., Liao, D. & Gregersen, H. (2007) In vivo areal modulus of elasticity estimation of the human tympanic membrane system: modelling of middle ear mechanical function in normal young and aged ears. *Physics in medicine and biology*. **52**(**3**), 803–814.

Gan, R. & Sun, Q. (2002) Finite element modeling of human ear with external ear canal and middle ear cavity. *Engineering in Medicine and Biology, 2002.*

Gan, R.Z., Sun, Q., Dyer, R.K., Chang, K.-H. & Dormer, K.J. (2002) Three-dimensional modeling of middle ear biomechanics and its applications. *Otology & neurotology*. **23**(**3**), 271–280.

Gan, R.Z., Sun, Q., Feng, B. & Wood, M.W. (2006) Acoustic-structural coupled finite element analysis for sound transmission in human ear--pressure distributions. *Medical engineering & physics*. **28**(**5**), 395–404.

Gentil, F., Parente, M., Martins, P., Garbe, C., Jorge, R.N., Ferreira, A. & Tavares, J.M.R.S. (2011) The influence of the mechanical behaviour of the middle ear ligaments: a finite element analysis. *Proceedings of the Institution of Mechanical Engineers. Part H, Journal of engineering in medicine*. **225**(**1**), 68–76.

Ghadarghadar, N., Agrawal, S.K., Samani, A. & Ladak, H.M. (2013) Estimation of the quasi-static Young ' s modulus of the eardrum using a pressurization technique. *Computer Methods and Programs in Biomedicine*. **110**(**3**), 231–239.

Graham, M.D., Reams, C. & Perkins, P. (1977) Human Tympanic Membrane - Malleus Attachment. Preliminary Study. *The Annals of otology, rhinology, and laryngology*, 426–431.

De Greef, D., Aernouts, J., Aerts, J., Cheng, J.T., Horwitz, R., Rosowski, J.J. & Dirckx, J.J.J. (2014) Viscoelastic properties of the human tympanic membrane studied with stroboscopic holography and finite element modeling. *Hearing Research*. **312**, 69–80.

De Greef, D., Buytaert, J.A.N., Aerts, J.R.M., Van Hoorebeke, L., Dierick, M. & Dirckx, J. (2015) Details of human middle ear morphology based on micro-CT imaging of phosphotungstic acid stained samples. *Journal of Morphology*. **276**(**9**), 1025–1046.

Hesabgar, S.M., Marshall, H., Agrawal, S.K., Samani, A. & Ladak, H.M. (2010) Measuring the quasi-static Young's modulus of the eardrum using an indentation technique. *Hearing Research*. **263**(**1**–**2**), 168–176.

Huang, G., Daphalapurkar, N.P., Gan, R.Z. & Lu, H. (2008) A method for measuring linearly viscoelastic properties of human tympanic membrane using nanoindentation. *Journal of biomechanical engineering*. **130**(**1**), 14501.

Van der Jeught, S., Dirckx, J.J.J., Aerts, J.R.M., Bradu, A., Podoleanu, A.G.H. & Buytaert, J.A.N. (2013) Full-field thickness distribution of human tympanic membrane obtained with optical coherence tomography. *Journal of the Association for Research in Otolaryngology : JARO*. **14**(**4**), 483–94.

Kirikae, I. (1960) *The Structure and Function of the Middle Ear*, University of Tokyo Press.

Kuypers, L.C., Decraemer, W.F. & Dirckx, J.J.J. (2006) Thickness distribution of fresh and preserved human eardrums measured with confocal microscopy. *Otology & neurotology*. **27**(**2**), 256–264.

Ladak, H.M., Decraemer, W.F., Dirckx, J.J. & Funnell, W.R. (2000) Systematic errors in small deformations measured by use of shadow-moiré topography. *Applied optics*. **39**(**19**), 3266–75.

Ladak, H.M., Funnell, W.R.J., Decraemer, W.F. & Dirckx, J.J.J. (2006) A geometrically nonlinear finite-element model of the cat eardrum. *The Journal of the Acoustical Society of America*. **119**(**5 Pt 1**), 2859–2868.

Lee, C.F., Chen, P.R., Lee, W.J., Chou, Y.F., Chen, J.H. & Liu, T.-C. (2010) Computer aided modeling of human mastoid cavity biomechanics using finite element analysis. *Eurasip Journal on Advances in Signal Processing*. **2010**.

Lee, C.L., Hsu, L.P., Chen, P.R. & Lee, C.F. (2006) Computer aided design for three-dimensional visualization and modeling of middle ear biomechanics. *Tzu Chi Medical Journal*. **18**(**6**), 416–422.

Liang, J., Luo, H., Yokell, Z., Nakmali, D., Gan, R. & Lu, H. (2016) Characterization of the nonlinear elastic behavior of chinchilla tympanic membrane using micro-fringe projection. *Hearing research*.

Lim, D. (1994) Structure and function of the tympanic membrane: a review. *Acta oto-rhino-laryngologica Belgica*. **49**(**2**), 101–115.

Lim, D.J. (1970) Human tympanic membrane: an ultrastructural observation. *Acta Oto-laryngologica*. **70**(**3**), 176–186.

Luo, H., Dai, C., Gan, R.Z. & Lu, H. (2009) Measurement of young's modulus of human tympanic membrane at high strain rates. *Journal of biomechanical engineering*. **131**(**6**), 64501.

Maftoon, N., Funnell, W.R.J., Daniel, S.J. & Decraemer, W.F. (2015) Finite-Element Modelling of the Response of the Gerbil Middle Ear to Sound. *JARO - Journal of the Association for Research in Otolaryngology*. **16**(**5**), 547–567.

Mikhael, C.S., Funnell, W.R.J. & Bance, M. (2004) Middle-ear finite-element modelling with realistic geometry and a priori material-property estimates. In *Proceeding of Canadian Medical and Biological Engineering Society*. p. 126–129.

Qi, L., Funnell, W.R.J. & Daniel, S.J. (2008) A nonlinear finite-element model of the newborn middle ear. *The Journal of the Acoustical Society of America*. **124**(**1**), 337–347.

Rohani, S.A., Ghomashchi, S., Umoh, J.U., Holdsworth, D.W., Agrawal, S.K. & Ladak, H.M. (2016) Iodine potassium iodide improves the contrast-to-noise ratio of micro-computed tomography images of the human middle ear. *Journal of Microscopy*. Available at: http://doi.wiley.com/10.1111/jmi.12447.

Salamati, E., Agrawal, S.K., Samani, A. & Ladak, H.M. (2012) Estimation of the orthotropic elastic properties of the rat eardrum. *Journal of Medical and Biological Engineering*. **32**(**4**), 225–234.

Samani, A., Bishop, J. & Plewes, D.B. (2001) A constrained modulus reconstruction technique for breast cancer assessment. *IEEE Transactions on Medical Imaging*. **20**(**9**), 877–885.

Shimada, T. & Lim, D.J. (1971) The fiber arrangement of the human tympanic membrane. scanning electron microscopic observation. *The Annals of otology, rhinology, and laryngology*. **80**(**2**), 210–217.

Sun, Q., Gan, R.Z., Chang, K.H. & Dormer, K.J. (2002) Computer-integrated finite element modeling of human middle ear. *Biomechanics and modeling in mechanobiology*. **1**(**2**), 109–122.

Volandri, G., Di Puccio, F., Forte, P. & Carmignani, C. (2011) Biomechanics of the tympanic membrane. *Journal of Biomechanics*. **44**(**7**), 1219–1236.

Wada, H., Metoki, T. & Kobayashi, T. (1992) Analysis of dynamic behavior of human middle ear using a finite-element method. *The Journal of the Acoustical Society of America*. **92**(**6**), 3157–3168.

Wang, X., Cheng, T. & Gan, R.Z. (2007) Finite-element analysis of middle-ear pressure effects on static and dynamic behavior of human ear. *The Journal of the Acoustical Society of America*. **122**(**2**), 906–917.

Wen, Y. hsuan, Hsu, L. ping, Chen, P. rong & Lee, C. fone (2006) Design Optimization of Cartilage Myringoplasty using Finite Element Analysis. *Tzu Chi Medical Journal*. **18**(**5**), 370–377.

Zhang, X. & Gan, R.Z. (2011) Experimental measurement and modeling analysis on mechanical properties of incudostapedial joint. *Biomechanics and Modeling in Mechanobiology*. **10**(**5**), 713–726.

Chapter 4:
Spatial Non-Uniformity of Human Pars Tensa

The content of this chapter are in preparation to be submitted to: Journal of Biomechanics, as "Spatial Non-Uniformity in the Young's Modulus of the Human Pars Tensa", by S. A. Rohani, S. Ghomashchi, S. K. Agrawal, H. M. Ladak.

4.1 Introduction

Finite-element (FE) models of the tympanic membrane (TM) are sensitive to the Young's modulus of the pars tensa (PT) (Funnell & Laszlo, 1978). Recently, methods have been developed to estimate the PT Young's modulus with an *in situ* TM (Ghadarghadar et al., 2013; Aernouts et al., 2012; Hesabgar et al., 2010), thus avoiding the potential for structural damage caused by approaches that require cutting of strips from the PT (Von Békésy & Wever, 1960; Kirikae, 1960; Decraemer et al., 1980; Cheng et al., 2007; Huang et al., 2008; Daphalapurkar et al., 2009; Luo et al., 2009). With *in situ* methods, a stimulus is applied to the TM under test and its mechanical response is measured. An FE model is then constructed for the TM being tested and a numerical optimization framework is used to adjust the PT Young's modulus so that computed response matches measured response, and the optimal value is taken to be the Young's modulus of the actual PT. Since the properties of the PT vary with frequency (Decraemer et al., 1980; Luo et al., 2009), estimates are usually reported for the quasi-static regime with stimuli frequencies of less than 20 Hz and for the dynamic regime with stimuli frequencies generally from 20 Hz to 20 kHz.

All existing *in situ* estimation techniques assume that the PT is uniform across its surface, so only one global value of the Young's modulus is reported. However, the spatially-varying ultrastructure of the PT (Lim, 1970) suggests that its Young's modulus may vary along its surface.

The objective of this work is to extend an existing *in situ* estimation technique based on pressurization and inverse FE modeling (Ghadarghadar et al., 2013) to estimate spatial variations in the PT Young's modulus. As noted, the previous implementation of this technique assumes that the PT is uniform and estimates one global Young's modulus value. Relative to the literature on TM biomechanics, this study makes two important contributions. First, it extends an *in situ* technique to allow for modeling of a spatially varying Young's modulus. Second, it tests two spatially-constrained Young's modulus variations to determine if there is an improved fit between simulated human PT deformation patterns and measured ones.

4.2 Methods

4.2.1 Experimental Procedure

Three fresh-frozen adult cadaveric temporal bones, TB1, TB2, TB3, were used in this study which were donated to Western University for the purposes of medical education and research. In this study, the shape of each sample TM before and after pressurization was imaged using a Fourier transform profilometer (FTP). The details of preparation of cadaveric materials and the experimental setup are given previously in Section 3.2.1 and Section 3.2.2, respectively.

The output of FTP measurement is a dense cloud of points in 3D space that represents the shape of the surface being measured. The deformation of the TM measured using FTP ($\Delta Z_{x,y}^{FTP}$) is calculated using the equation:

$$\Delta Z_{x,y}^{FTP} = Z_{x,y}^{FTP,P} - Z_{x,y}^{FTP,0} \qquad \text{Equation 4.1}$$

where $Z_{x,y}^{FTP,P}$ is the height of the TM surface at the point (x, y) when pressurized and $Z_{x,y}^{FTP,0}$ is the height of the TM surface at the same point (x, y) while the sample is at rest (i.e., unpressurized). All heights were measured relative to the XY-plane defined by the plane of the TM boundary.

4.2.2 Contrast-Enhanced Imaging

Since the TM periphery and malleus are not fully visible in FTP, each sample was scanned using micro-computed tomography (micro-CT) after the pressurization experiment. The samples were first fixed using formaldehyde solution to avoid degradation, and to improve the contrast of the TM in the micro-CT images, they were then stained using iodine potassium iodide prior to imaging; details of the fixation, staining and imaging procedure are given elsewhere (Rohani et al., 2016).

4.2.3 FE Model Generation

For each sample, the geometry of the TM was modeled from FTP data recorded at its resting position (unpressurized). As mentioned before, ossicular chain and the boundaries of the TM including annular ring are not visible in FTP. Therefore, the TM boundary, malleus and dental cement were manually segmented from micro-CT volumes using the MIPAV (Medical Image Processing, Analysis, and Visualization) software from the National Institutes of Health, USA (mipav.cit.nih.gov). In order to add the TM boundary

and malleus to the model from FTP, the micro-CT model was aligned to FTP data using least-square landmark-based registration. The landmarks used in registration were situated along the manubrium, including umbo and lateral process.

This resulted in one triangulated mesh for the TM, one for the malleus and one for the dental cement. Furthermore, for the TM and the malleus, NURBS (non-uniform rational B-spline) patches were fitted in Geomagic Studio (3D Systems Inc., SC, USA) as this representation is required for the FE meshing procedure. The dental cement was not converted to NURBS and was only segmented to provide the exact location of where to apply the boundary condition for FE modeling as discussed below.

All models were imported into COMSOL Multiphysics (COMSOL Inc., MA, USA) for meshing and FE analysis. For each sample, the malleus was meshed using tetrahedral solid elements while the TM was meshed using triangular shell elements. The TM annular ring was taken to be fully clamped. For the mallear head, the FE mesh nodes contacting the dental cement were taken to be fully clamped to simulate the experimental condition of malleus immobilization. These nodes could be identified because a triangulated surface of the dental cement was available for each specimen. The dental cement surface was only used for identifying which mallear nodes to constrain for simulation.

In order to incorporate spatial non-uniformity, two types of spatial partitioning schemes were considered for the PT. First, the PT was divided into 4 anatomical quadrants (i.e. anterior-superior, anterior-inferior, posterior-superior and posterior-inferior). Second, the PT was divided into 4 concentric rings (R1, R2, R3, and R4). For comparison, a uniform

PT was also considered. Sample FE models are shown in Figure 4-1 to illustrate the uniform case and the two partitioning schemes.

The two schemes used in this study are based on the literature. As already noted, the quadrant-based scheme was utilized in previous work to experimentally characterize PT Young's modulus (Daphalapurkar et al., 2009). The ring-based scheme has been used in FE modeling of the forward problem of simulating mechanical response to a stimulus given *a priori* knowledge of the material properties (Ferris & Prendergast, 2000), but it has not been used in an optimization-based estimation framework as presented here.

In this study, the FE models of the TM and malleus were considered to be isotropic, linear elastic materials. As mentioned earlier, such materials can be characterized by a Young's modulus and a Poisson's ratio. The PT Young's modulus was optimized as described in Section 4.2.4.

In this study, standard mesh refinement and convergence procedure were followed to assure the quality of the mesh. Also, geometric nonlinearity was included in this study which is necessary when modeling thin objects such as TM that undergo large displacements.

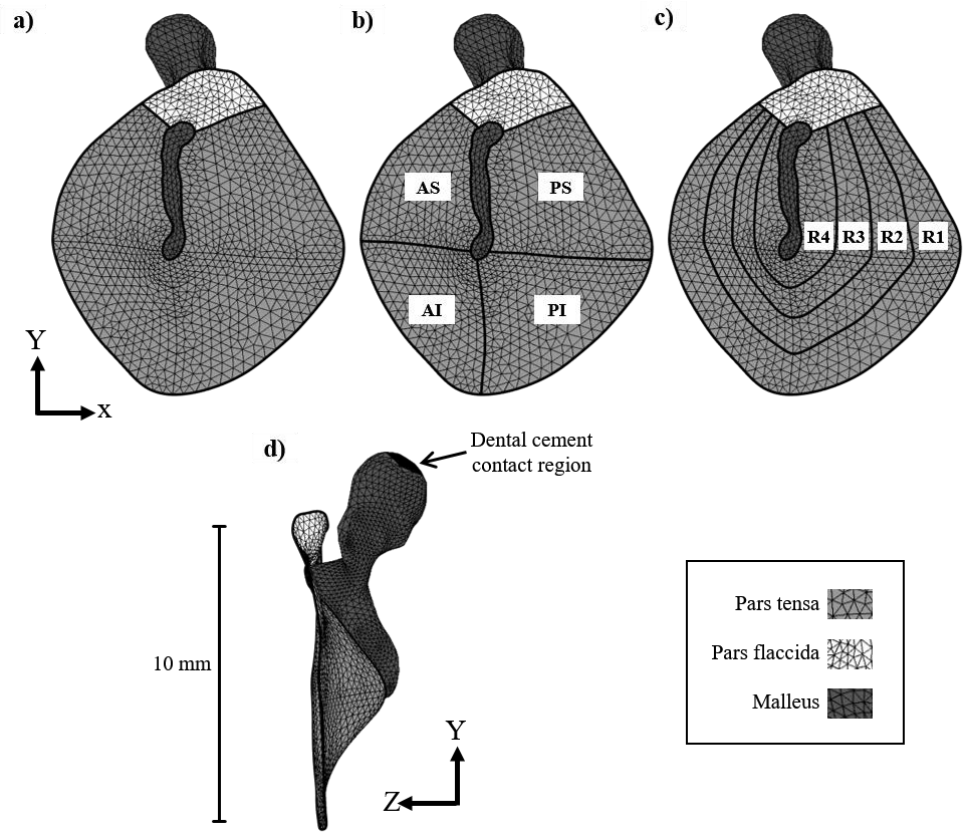

Figure 4-1: FE mesh for TB1. The tympanic ring and the portion of the mallear head in contact with dental cement were taken to be fully clamped in the FE analysis. a) Uniform PT (i.e., not partitioned), b) PT partitioned into 4 quadrants, c) PT partitioned into 4 concentric rings, d) coronal view of the FE mesh showing the dental cement contact region.

During each iteration of the optimization procedure, the PF Young's modulus was constrained to be ½ of the PT Young's modulus for the uniform case and ½ of the smallest Young's modulus values amongst the partitions for the two spatially-varying cases. This ratio of ½ has been used in previous studies for a uniform PT (Sun et al., 2002; Lee et al., 2010; Lee et al., 2006; Qi et al., 2004). The Poisson's ratio of the PT and PF were taken to be 0.49 to model incompressibility (Aernouts et al., 2010; Daphalapurkar et al., 2009; Huang et al., 2008; Elkhouri et al., 2006). The Young's modulus and Poisson's ratio of the malleus were assumed to be 14.1 GPa and 0.3, respectively as has been used in many

previous studies (Gan et al., 2002; Gan et al., 2006; Lee et al., 2010; Sun et al., 2002; Zhang & Gan, 2011; Gentil et al., 2011; Lee et al., 2006; Wen et al., 2006).

For shell elements, like those representing the TM, thickness also needs to be specified. A constant thickness of 110 μm was used for the PT in keeping with a recent study (Aernouts et al., 2012). For the PF, a constant thickness of 220 μm was used (Lim, 1970).

4.2.4 Optimization

For each sample, the PT Young's modulus was estimated separately for the uniform PT model and for the two partitioning schemes. For the uniform PT case, only one Young's modulus is required, and in the optimization framework, it is denoted E_U. For the quadrant-based scheme, the Young's modulus is constant over the surface of each quadrant, but may vary from quadrant to quadrant. Hence, four Young's modulus values must be estimated, one for each quadrant, and these are denoted as E_{AS}, E_{AI}, E_{PS} and E_{PI}. For the ring-based approach, each ring is assumed to be uniform but the Young's modulus is allowed to vary from one ring to the next; hence, four values need to be estimated again and are denoted E_{R1}, E_{R2}, E_{R3} and E_{R4}.

The PT Young's modulus is estimated by minimizing a cost function that defined so that a minimal value results when the deformed shape computed using the FE model for a particular specimen matches the corresponding measured shape. For the uniform case, the cost function is:

$$C(E_U) = \sum_{i=1}^{n} \left(Z_i^{FTP,P} - Z_i^{FE,P}(E_U) \right)^2 \qquad \text{Equation 4.2a}$$

where $Z_i^{FTP,P}$ and $Z_i^{FE,P}$ denote the measured and simulated Z coordinates, respectively, for point i in the pressurized state. The notation $Z_i^{FE,P}(E_U)$ means that the deformed shape is computed using the current estimate for E_U. Only the n points defining the PT that are visible in FTP were taken into account in Equation 4.2a.

For the non-uniform cases, the deformations computed using the FE model are a function of either E_{AS}, E_{AI}, E_{PS} and E_{PI} for quadrant-based partitioning or E_{R1}, E_{R2}, E_{R3} and E_{R4} for ring-based partitioning. Hence, the cost function for quadrant-based partitioning is:

$$C(E_{AS}, E_{AI}, E_{PS}, E_{PI}) = \sum_{i=1}^{n} \left(Z_i^{FTP,P} - Z_i^{FE,P}(E_{AS}, E_{AI}, E_{PS}, E_{PI})\right)^2 \qquad \text{Equation 4.2b}$$

For ring-based partitioning, the cost function is:

$$C(E_{R1}, E_{R2}, E_{R3}, E_{R4}) = \sum_{i=1}^{n} \left(Z_i^{FTP,P} - Z_i^{FE,P}(E_{R1}, E_{R2}, E_{R3}, E_{R4})\right)^2 \qquad \text{Equation 4.2c}$$

Optimization was performed using a variant of the Nelder-Mead simplex method (Lagarias et al., 1998) in MATLAB R2015a (Natick, MA). This algorithm finds the minimum of a single/multi-variable cost function given lower and upper search bounds. The lower search bound on the Young's modulus values was set to 1 MPa, and the upper bound was set to 300 MPa. This is a large bound that covers the range of potential values that have been used or estimated in published studies. The optimization was terminated if values of C changed by less than 0.01% between successive iterations. To ensure that a unique optimum value is reached in the given range, the initialization of the optimization algorithm was varied over an order of magnitude (results from two cases of initialization are provided in the Appendix C). Figure 4-2 shows a schematic representation of the optimization technique.

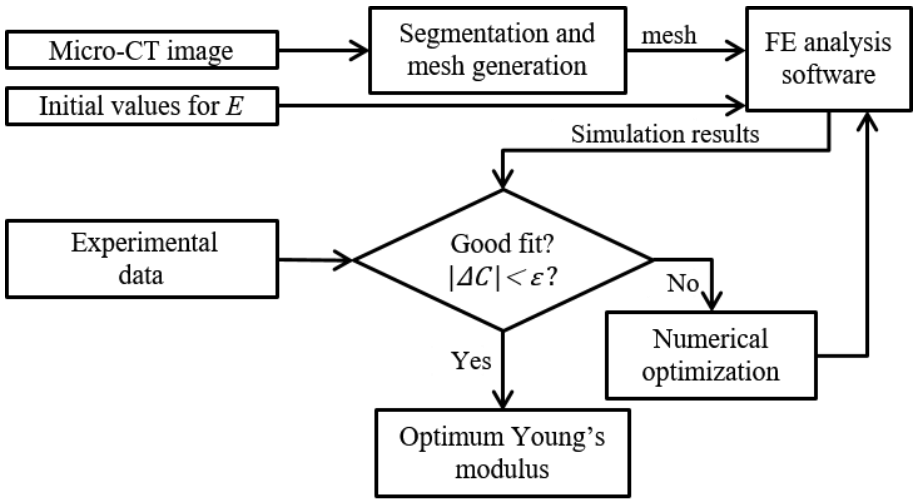

Figure 4-2: Flowchart for estimation algorithm. C is the cost function to be minimized and ε is the optimization convergence parameter.

To assess the quality of the Young's modulus estimates, the simulated TM deformation ($\Delta Z_{x,y}^{FE}$) was computed using the following equation and compared to measured deformation ($\Delta Z_{x,y}^{FTP}$):

$$\Delta Z_{x,y}^{FE} = Z_{x,y}^{FE,P} - Z_{x,y}^{FE,0} \qquad \text{Equation 4.3}$$

In Equation 4.3, $Z_{x,y}^{FE,P}$ is the simulated height of the TM surface at the point (x, y) when pressurized and $Z_{x,y}^{FE,0}$ is the height of the TM surface at the same point (x, y) while the sample is at rest (i.e., unpressurized). When computing $Z_{x,y}^{FE,P}$, optimal Young's modulus values are used. Note that simulated and experimental deformations are compared instead of pressurized shapes to better highlight differences between experiment and model. The differences are small relative to height values and are difficult to discern when viewing pressurized shapes, but become more apparent when viewing deformation patterns.

4.3 Results

The PT Young's modulus values estimated from sample-specific FE models are given in Table 4-1. Varying the initialization only caused less than 1% variation in the results.

Table 4-1: Estimated PT Young's modulus for three types of PT models: uniform, quadrant-based partitioning and ring-based partitioning. All values are in MPa.

		TB1	TB2	TB3
Uniform	E_U	2.2	2.4	2.0
Quadrant-based	E_{AS}	1.1	1.1	1.6
	E_{AI}	1.7	1.1	1.6
	E_{PS}	3.6	1.6	1.2
	E_{PI}	2.8	8.6	3.1
Ring-based	E_{R1}	14.9	1.3	5.8
	E_{R2}	7.0	23.4	1.3
	E_{R3}	1.2	15.6	1.1
	E_{R4}	1.1	1.2	3.7

The measured deformations using the FTP apparatus (ΔZ^{FTP}) are shown in Figure 4-3. As noted in Chapter 3, maximum deformation occurred in the posterior PT and was centred in the infero-superior directions in TB1 and TB2. In TB3, the maximum also occurred in the posterior PT but was located slightly inferior to the locations in TB1 and TB2.

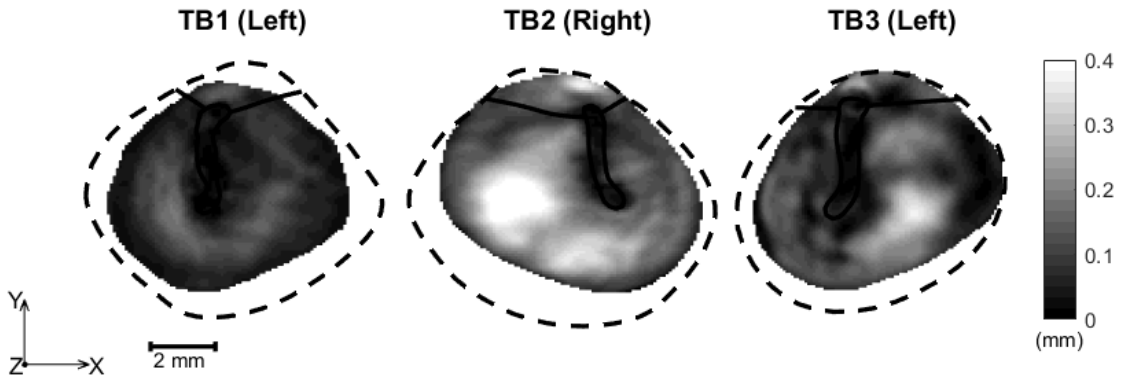

Figure 4-3: Measured deformation of human TM using FTP. Anatomical directions: positive Y axis is superior direction for all three samples. Positive X axis is posterior direction for samples TB1 and TB3 and anterior direction for TB2. The dashed boundary is the annular ring which is not observed using FTP because of the overhanging ear canal. The boundary was found using micro-CT and was used to define the FE models.

The deformation patterns simulated using subject-specific FE models with optimal Young's modulus values are shown in the top row of Figure 4-4 for TB1, Figure 4-5 for TB2 and Figure 4-6 for TB3. For each specimen, deformation patterns were computed using a uniform PT or a spatially-varying PT with either quadrant-based partitioning or

ring-based partitioning. Regardless of the type of partitioning, the simulated deformation patterns agree qualitatively with the corresponding measured pattern (see Figure 4-3) in terms of the general location of the maximum and the shape of the deformation patterns. However, for any given specimen, there are differences in the magnitudes of the deformations depending on the type of non-uniformity considered. To highlight the spatial differences in deformation magnitude, errors maps were computed between the FE-simulated pressurized height ($Z^{FE,P}$) and the FTP measured height ($Z^{FTP,P}$) as $Z^{FE,P} - Z^{FTP,P}$ and are shown in the bottom panel of Figures 4-6 – 4-8.

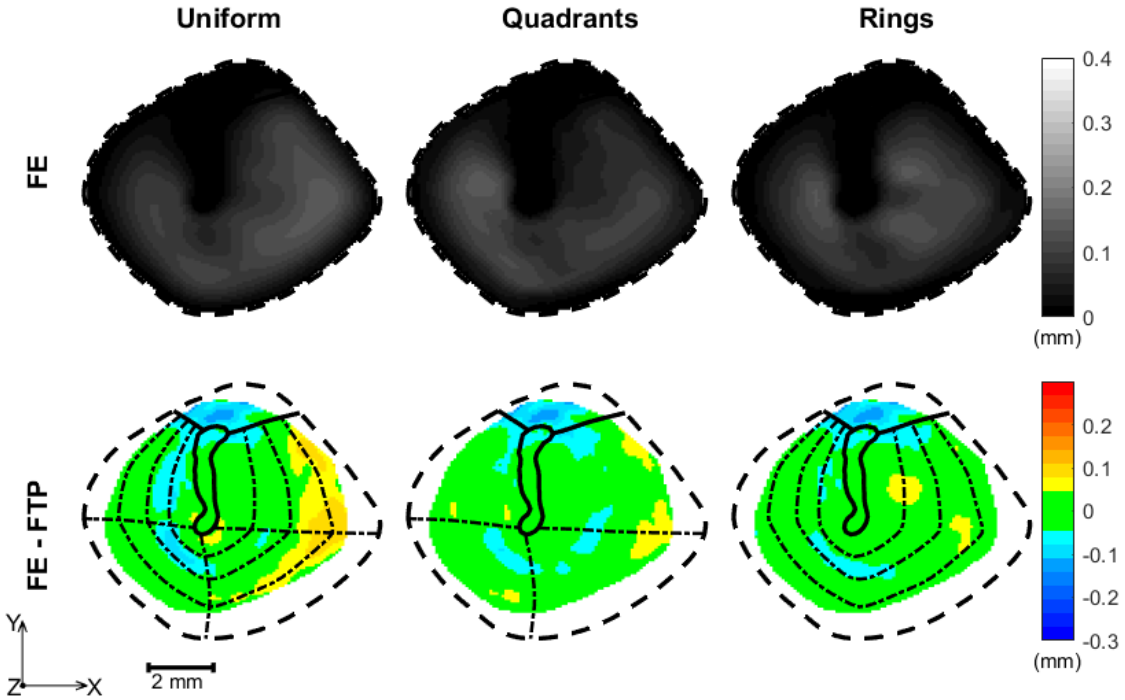

Figure 4-4: Simulated deformation patterns and error maps for sample TB1 for three types of PT partitioning: uniform (i.e., not partitioned), quadrant-based partitioning, and concentric ring-based partitioning. Top row: FE-simulated deformations. Bottom row: Error maps defined as $Z^{FE,P}$ - $Z^{FTP,P}$. Anatomical directions: positive Y axis is superior direction. Positive X axis is posterior direction. The dashed boundary is the annular ring which is not observed using FTP because of the overhanging ear canal. The solid lines demarcate the manubrium and PF, and the dash-dotted lines show the partitions.

Positive errors (yellow and red regions) indicate that the PT deformed more in the FE model than in the experiment, whereas negative errors (blue regions) indicate that the PT deformed less in the FE model than in the experiment. Areas that are green are where the difference is zero or close to it.

Although the spatial distribution of the differences varies in a specimen-specific manner, for all three specimens the error approaches zero over a larger region of the model PT when the PT is partitioned into four sections (either quadrants or concentric rings) as compared to the uniform case; the reduction in difference *magnitude* (i.e., the absolute value of the difference) towards zero is apparent from the increasing amount of green over the surface of the PT as one proceeds from the uniform case to the non-uniform cases.

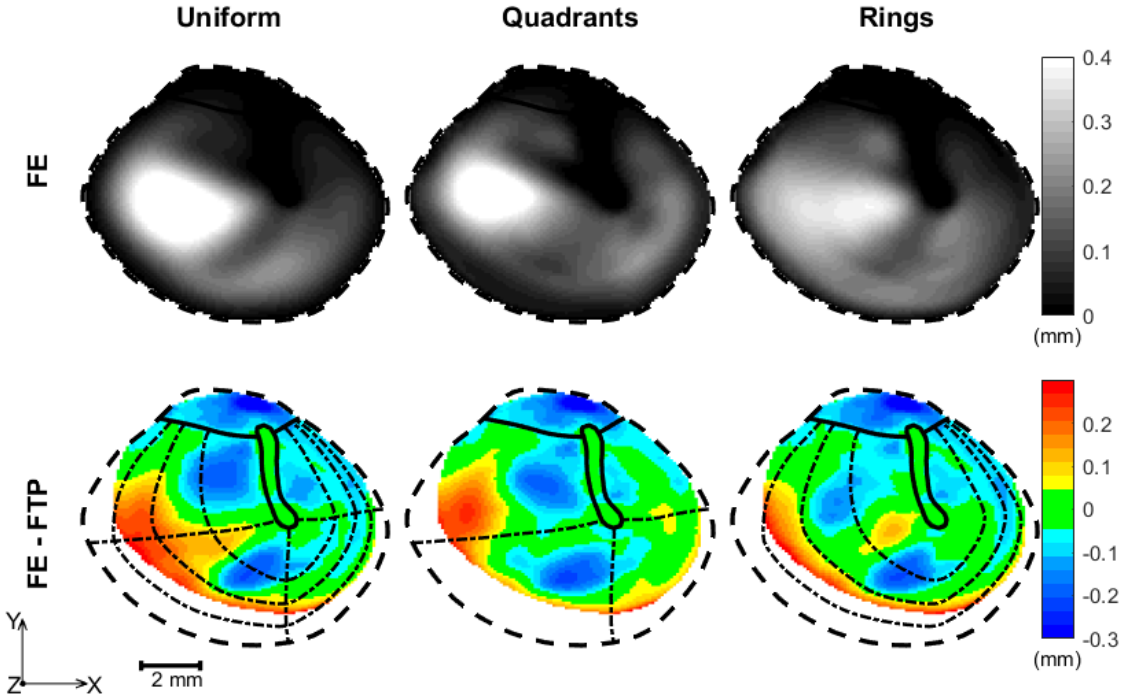

Figure 4-5: Simulated deformation patterns and error maps for sample TB2 for three types of PT partitioning: uniform (i.e., not partitioned), quadrant-based partitioning, and concentric ring-based partitioning. Top row: FE-simulated deformations. Bottom row: Error maps defined as $Z^{FE,P}$ - $Z^{FTP,P}$. Anatomical directions: positive Y axis is superior direction. Positive X axis is anterior direction. The dashed boundary is the annular ring which is not observed using FTP because of the overhanging ear

canal. The solid lines demarcate the manubrium and PF, and the dash-dotted lines show the partitions.

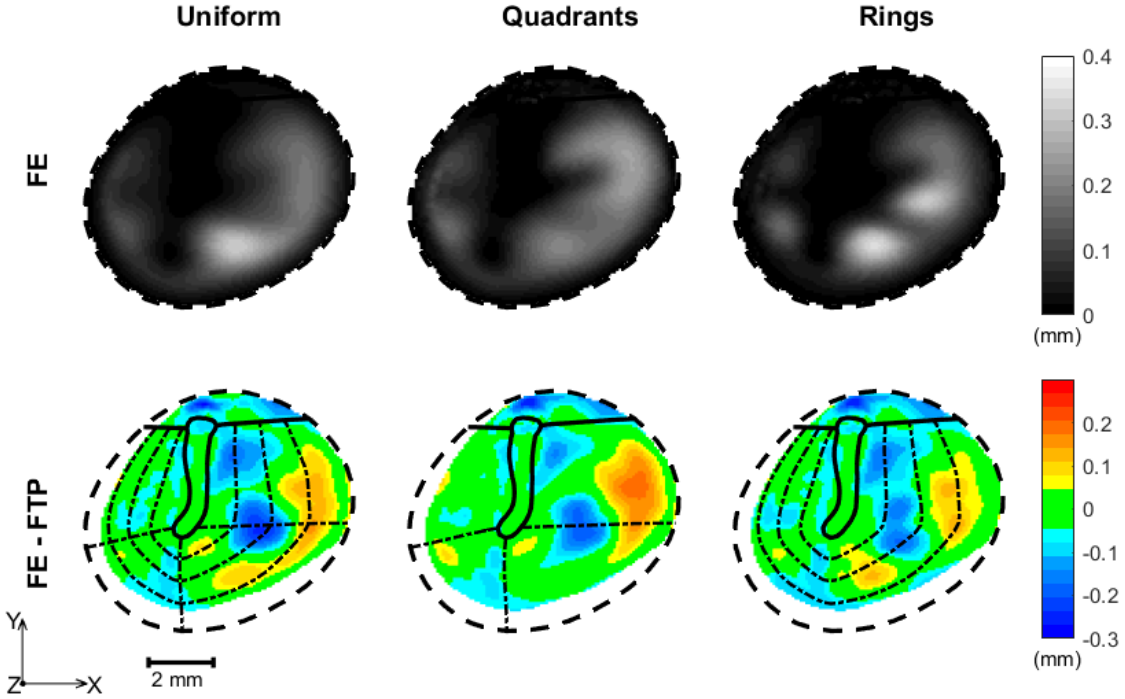

Figure 4-6: Simulated deformation patterns and error maps for sample TB3 for three types of PT partitioning: uniform (i.e., not partitioned), quadrant-based partitioning, and concentric ring-based partitioning. Top row: FE-simulated deformations. Bottom row: Error maps defined as $Z^{FE,P}$ - $Z^{FTP,P}$. Anatomical directions: positive Y axis is superior direction. Positive X axis is posterior direction. The dashed boundary is the annular ring which is not observed using FTP because of the overhanging ear canal. The solid lines demarcate the manubrium and PF, and the dash-dotted lines show the partitions.

In order to quantitatively compare the three types of non-uniformity (uniform, quadrant-based and ring-based partitioning) presented in this work, the corresponding cost function values for Young's moduli are given in Table 4-2. By applying quadrant-based partitioning, the cost function values of TB1, TB2 and TB3 were reduced by 29%, 46% and 59%, respectively, compared to the uniform case. A reduction of the cost function relative to the uniform case was also observed when using ring-based partitioning; the cost function values of TB1, TB2 and TB3 were reduced by 45%, 49% and 63%, respectively. Partitioning into concentric rings provides a greater reduction in difference magnitude

compared to partitioning into quadrants, but this reduction appears to be specimen-specific, being larger in TB1 than in TB2 and TB3.

Table 4-2: Cost function values for three types of PT models: uniform, quadrant-based partitioning and ring-based partitioning.

	TB1	TB2	TB3
Uniform: $C(E_U)$ [mm^2]	1.24	10.32	7.34
Quadrants: $C(E_{AS}, E_{AI}, E_{PS}, E_{PI})$ [mm^2]	0.87	5.58	3.01
Rings: $C(E_{R1}, E_{R2}, E_{R3}, E_{R4})$ [mm^2]	0.67	5.22	2.68

4.4 Discussion

This work represents the first attempt at estimating the PT Young's modulus using an *in situ* inverse FE modeling framework that takes into account spatial non-uniformity. Three types of spatial variations were considered: uniform (i.e., no variation), quadrant-based variation and concentric ring-based variation. The uniform case permits comparison to our past work to ensure that results do not change with a new choice of optimization technique. The average PT Young's modulus estimated in this study is 2.2±0.2 MPa which is identical to that determined in Chapter 3. As noted in that chapter, this estimate compares well with the value of 2.9±1.3 MPa that has recently been reported using quasi-static *in situ* indentation testing and (Aernouts et al., 2012).

The two types of non-uniformity which were studied in this work were selected based on previous experimental observations in the literature. Daphalapurkar *et al*. have reported some variations in the human PT Young's modulus over 4 quadrants based on nanoindentation testing of sections cut from the PT (Daphalapurkar et al., 2009). The authors reported two types of Young's moduli: in-plane Young's modulus tested on 2 samples and out-of-plane Young's modulus tested on 3 samples. The in-plane Young's

modulus refers to the modulus in the tangential plane of the PT. In-plane values averaged over all quadrants were 37.8 ± 0.52 MPa in one specimen and 25.73 ± 2.8 MPa in the other specimen. These values are much larger than those reported in the current work and those reported elsewhere (Aernouts et al., 2012). The larger values arise because Daphalapurkar *et al.* removed the epidermal layer and used a thickness of 60 μm in their model (Daphalapurkar et al., 2009). The small standard deviations reported by Daphalapurkar *et al.* indicate that the in-plane modulus does not vary appreciably from quadrant to quadrant, which contrasts markedly with our study which demonstrates that quadrant-based spatial variation in the PT Young's modulus can improve matching of FE modeling results to experimental data as evidenced by the reduction in the cost function. Daphalapurkar *et al.* used a nanoindentation test to experimentally characterize a point on each PT quadrant. Nanoindentation is a test that is localized to a point, and therefore, should only be used to characterize a material locally. By contrast, the pressurization approach provides a global spatial average over each quadrant. Nanoindentation at multiple locations in each quadrant may have revealed spatial variation more clearly in the work of Daphalapurkar *et al*. The out-of-plane Young's modulus reported by Daphalapurkar *et al.* represents the elasticity when the tissue is compressed by rigid structures acting on both faces of the PT. This is not a physiological situation and is not comparable to our study.

Partitioning into concentric rings, approximately centred around the umbo, was also considered in the current work as electron microscopy observations indicate that collagen fibre packing varies with respect to distance from the TM's annular ring (Lim, 1970). Specifically, the radial fibers become more densely packed as they converge on the manubrium (Lim, 1970). By contrast, the circumferential fibers are most densely packed

near the periphery of the PT and thin out or are even absent closer to the centre (Shimada & Lim, 1971). To date, there is no work estimating the PT Young's modulus after sectioning into rings; nevertheless, this type of spatial non-uniformity has been of incorporated into one FE model (Ferris & Prendergast, 2000). The values in that study are in the range of 10 MPa to 40 MPa and assume orthotropic material properties. The authors based their estimates on the data reported by Kirikae which used dynamic stimuli (Kirikae, 1960). These values are higher than those estimated in the current work and may reflect the trend for increase in Young's moduli with increasing frequency (Luo et al., 2009).

As shown in the error maps in the lower rows of Figures 6 – 8, when the PT is assumed to be uniform, simulated deformations deviate from measured deformations in a spatially varying manner. Intuitively, in order to improve the matching, the Young's modulus of yellow regions (i.e., where $Z^{FE,P} > Z^{FTP,P}$) should be increased to lower the computed deformation. On the other hand, the Young's modulus of blue regions (i.e., where $Z^{FE,P} < Z^{FTP,P}$) should be decreased to increase the computed deformation. Partitioning allows for local variation in Young's modulus, and this can improve the match between simulated and experimental data to some extent. As evidenced from Figures 4-6 – 4-8, central and rightmost columns, complete matching is not possible. This happens because if one partition has both yellow and blue regions in the error map of the uniform case (e.g., posterior-inferior region of TB2 in the lower left-hand corner of Figure 4-7), the multi-parameter optimization algorithm must find a single optimal Young's modulus in the partition that satisfies two contradictory goals: Increasing the Young's modulus to improve the fit in the yellow regions of the partition or decreasing it in the blue regions.

These two goals cannot be achieved using a single parameter, and therefore, further refinement of the partitions is required as this introduces additional parameters for fitting. In the extreme case of refinement, the Young's modulus of each mesh element could be optimized. This would require optimization of a very large number of parameters (e.g., 1701 for the PT mesh for TB1) which is numerically challenging (Samani et al., 2001) and may result in overfitting. In this work, an attempt was made to avoid numerical challenges and to avoid overfitting by constraining Young's modulus variations based on past literature for the quadrant-based case or loosely on the ultrastructure of the PT as in the ring-based case.

4.5 Conclusions

The spatial non-uniformity of Young's modulus of the human pars tensa was investigated for two cases, partitioning into four quadrants and partitioning into four concentric rings. The Young's modulus values were estimated using *in situ* quasi-static pressurization and inverse FE modeling. The results showed some improvements in the matching of FE-simulated deformations to FTP-based deformations measurements in all three samples when partitioning was applied.

4.6 Acknowledgements

Funding for this work was provided by the Natural Sciences and Engineering Research Council of Canada.

4.7 References

Aernouts, J., Aerts, J.R.M. & Dirckx, J.J.J. (2012) Mechanical properties of human tympanic membrane in the quasi-static regime from in situ point indentation measurements. *Hearing Research*. **290**(**1**–**2**), 45–54.

Aernouts, J., Soons, J. a M. & Dirckx, J.J.J. (2010) Quantification of tympanic membrane elasticity parameters from in situ point indentation measurements: Validation and preliminary study. *Hearing Research*. **263**(**1**–**2**), 177–182.

Von Békésy, G. & Wever, E.G. (1960) *Experiments in hearing*, McGraw-Hill New York.

Cheng, T., Dai, C. & Gan, R.Z. (2007) Viscoelastic properties of human tympanic membrane. *Annals of Biomedical Engineering*. **35**(**2**), 305–314.

Daphalapurkar, N.P., Dai, C., Gan, R.Z. & Lu, H. (2009) Characterization of the linearly viscoelastic behavior of human tympanic membrane by nanoindentation. *Journal of the Mechanical Behavior of Biomedical Materials*. **2**(**1**), 82–92.

Decraemer, W., Maes, M. & Vanhuyse, V. (1980) A non-linear viscoelastic constitutive equation for soft biological tissues, based upon a structural model. *Journal of.*

Elkhouri, N., Liu, H. & Funnell, W.R.J. (2006) Low-frequency finite-element modeling of the gerbil middle ear. *Journal of the Association for Research in Otolaryngology*. **7**(**4**), 399–411.

Ferris, P. & Prendergast, P.J. (2000) Middle-ear dynamics before and after ossicular replacement. *Journal of Biomechanics*. **33**(**5**), 581–590.

Funnell, W.R.J. & Laszlo, C.A. (1978) Modeling of the cat eardrum as a thin shell using the finite-element method. *The Journal of the Acoustical Society of America*. **63**(**5**), 1461–1467.

Gan, R.Z., Sun, Q., Dyer, R.K., Chang, K.-H. & Dormer, K.J. (2002) Three-dimensional modeling of middle ear biomechanics and its applications. *Otology & neurotology*. **23**(**3**), 271–280.

Gan, R.Z., Sun, Q., Feng, B. & Wood, M.W. (2006) Acoustic-structural coupled finite element analysis for sound transmission in human ear--pressure distributions. *Medical engineering & physics*. **28**(**5**), 395–404.

Gentil, F., Parente, M., Martins, P., Garbe, C., Jorge, R.N., Ferreira, A. & Tavares, J.M.R.S. (2011) The influence of the mechanical behaviour of the middle ear ligaments: a finite element analysis. *Proceedings of the Institution of Mechanical Engineers. Part H, Journal of engineering in medicine*. **225**(**1**), 68–76.

Ghadarghadar, N., Agrawal, S.K., Samani, A. & Ladak, H.M. (2013) Estimation of the quasi-static Young ' s modulus of the eardrum using a pressurization technique. *Computer Methods and Programs in Biomedicine*. **110**(**3**), 231–239.

Hesabgar, S.M., Marshall, H., Agrawal, S.K., Samani, A. & Ladak, H.M. (2010) Measuring the quasi-static Young's modulus of the eardrum using an indentation technique. *Hearing Research*. **263**(**1**–**2**), 168–176.

Huang, G., Daphalapurkar, N.P., Gan, R.Z. & Lu, H. (2008) A method for measuring linearly viscoelastic properties of human tympanic membrane using nanoindentation. *Journal of biomechanical engineering*. **130**(**1**), 14501.

Kirikae, I. (1960) *The Structure and Function of the Middle Ear*, University of Tokyo Press.

Lee, C.F., Chen, P.R., Lee, W.J., Chou, Y.F., Chen, J.H. & Liu, T.-C. (2010) Computer aided modeling of human mastoid cavity biomechanics using finite element analysis. *Eurasip Journal on Advances in Signal Processing*. **2010**.

Lee, C.L., Hsu, L.P., Chen, P.R. & Lee, C.F. (2006) Computer aided design for three-dimensional visualization and modeling of middle ear biomechanics. *Tzu Chi Medical Journal*. **18**(**6**), 416–422.

Lim, D.J. (1970) Human tympanic membrane: an ultrastructural observation. *Acta Oto-laryngologica*. **70**(**3**), 176–186.

Luo, H., Dai, C., Gan, R.Z. & Lu, H. (2009) Measurement of young's modulus of human tympanic membrane at high strain rates. *Journal of biomechanical engineering*. **131**(**6**), 64501.

Qi, L., Mikhael, C.S. & Funnell, W.R.J. (2004) APPLICATION OF THE TAGUCHI METHOD TO SENSITIVITY ANALYSIS OF A MIDDLE- EAR FINITE-ELEMENT MODEL Figure 1 : Parameters ' main effects on TM volume displacement. , 5–8.

Rohani, S.A., Ghomashchi, S., Umoh, J.U., Holdsworth, D.W., Agrawal, S.K. & Ladak, H.M. (2016) Iodine potassium iodide improves the contrast-to-noise ratio of micro-computed tomography images of the human middle ear. *Journal of Microscopy*. **264**(**3**), 334–338.

Samani, A., Bishop, J. & Plewes, D.B. (2001) A constrained modulus reconstruction technique for breast cancer assessment. *IEEE Transactions on Medical Imaging*. **20**(**9**), 877–885.

Shimada, T. & Lim, D.J. (1971) The fiber arrangement of the human tympanic membrane. scanning electron microscopic observation. *The Annals of otology, rhinology, and laryngology*. **80**(**2**), 210–217.

Sun, Q., Gan, R.Z., Chang, K.H. & Dormer, K.J. (2002) Computer-integrated finite element modeling of human middle ear. *Biomechanics and modeling in mechanobiology*. **1**(**2**), 109–122.

Wen, Y. hsuan, Hsu, L. ping, Chen, P. rong & Lee, C. fone (2006) Design Optimization of Cartilage Myringoplasty using Finite Element Analysis. *Tzu Chi Medical Journal*. **18**(**5**), 370–377.

Zhang, X. & Gan, R.Z. (2011) A comprehensive model of human ear for analysis of implantable hearing devices. *IEEE Transactions on Biomedical Engineering*. **58**(**10 PART 2**), 3024–3027.

Chapter 5:
Summary and Future Directions

5.1 Summary

The prevalence of hearing loss is drastically increasing. Early diagnosis of the hearing loss is a crucial step toward preventing its lifelong consequences. Current clinical audiology techniques could be optimized by the means of finite-element (FE) models. The accuracy of such models depends on the representation of geometry and mechanical properties. In this thesis, the focus was on these two significant aspects of FE modeling of the human middle ear.

5.1.1 Contrast-Enhanced Imaging

In Chapter 2, the effects of using iodine potassium iodide (IKI) as a contrast agent in micro-computed tomography (micro-CT) images of soft tissues of the human middle ear were quantified. In this study, three pairs of cadaveric human temporal bones were used. One bone of each pair was stained using IKI and one was kept unstained before imaging. The samples were imaged using a micro-CT scanner at the Robarts Research Institute (London, ON). The middle-ear soft tissues of interest in FE modeling were segmented in all six samples. Furthermore, the contrast-to-noise ratios (CNRs) of these tissues were calculated and compared. Results from a paired t-test indicated that the CNR was significantly ($p < 0.05$) increased in all of the segmented soft tissues.

5.1.2 Young's Modulus of Pars Tensa

In Chapter 3, a technique for estimating Young's modulus of the human pars tensa (PT) was developed based on inverse engineering and FE modeling. In this study, three cadaveric temporal bones were used. Following sample preparation, the shape of the PT before and after quasi-static pressurization was captured using a Fourier transform profilometer (FTP).

Furthermore, the samples were imaged using a micro-CT scanner in which IKI staining was used to improve the contrast of the tympanic membrane (TM). In the next step, sample-specific FE models were developed which included the TM and malleus. Next, the pressurized FTP data were used to estimate the Young's modulus of the PT for each sample by minimizing a cost function comparing the FTP data with the corresponding FE model. The average Young's modulus value was 2.2 ± 0.2 MPa. This result is comparable to recently published data in the literature.

5.1.3 Spatial Non-Uniformity in Young's Modulus of Pars Tensa

In Chapter 4, the study of Chapter 3 was extended to include spatial non-uniformity of the PT Young's modulus. The effects of two types of spatial non-uniformity on the optimization cost function were investigated in this study. The spatial non-uniformities were based on dividing PT into either four anatomical quadrants (quadrant-based partitioning) or four concentric regions (ring-based partitioning). A multi-parameter optimization technique was used to estimate the Young's modulus of PT in each of the partitioning scenarios. The results indicated reduction of the cost function when partitioning was applied.

5.2 Clinical Application

Accurate FE models of human middle ear could have multiple clinical applications. These applications could be divided into four categories; 1) improvement of understanding normal/diseased hearing mechanism, 2) improvement of clinical diagnostic techniques, 3) development of middle ear prosthesis and 4) improving pre-operative planning for surgeries. Such an accurate FE model requires accurate representation of geometry and mechanical properties of middle ear components.

Experimental understanding of diseased hearing mechanism requires finding identical pathological cases, which may not be feasible. Therefore, an accurate computational model such as an FE model could assist our understanding of the effect of pathologies on hearing. With the flexibility of FE models, simulating middle ear pathologies is not very challenging. For example, otosclerosis (occurs when stapes is immobilized due to excess bone growth around stapes footplate) could be modelled by adjusting the boundary condition of the stapes footplate in an existing FE model. Also, in FE models, multiple pathologies could be simulated and TM-to-cochlea sound transmission of many pathology combinations might be studied and compared with healthy ears.

FE models of the human middle ear may also contribute to improving interpretation of audiological tests. FE models could be used for investigation of the effect of single/multiple pathologies on the results of hearing tests such as tympanometry. This could potentially make the diagnosis of middle ear pathologies easier by providing insight into effect of each particular pathology on the results of tympanometry, i.e., tympanogram. Certain combination of pathologies could cancel their effects on the tympanograms. For example,

the tympanogram of a diseased ear having both otosclerosis and TM pathologies could be normal when tympanometry is performed at 226 Hz (the most common tympanometry frequency). In an FE model, it is possible to compare the effect of such a pathology combination on tympanograms of higher frequencies to search for an alternative frequency.

Similarly, hearing prostheses could also be added to an FE model of middle ear and their effects on the hearing mechanism could be studied. Such a study could be used for designing new prostheses.

Currently, the required ossicular replacement prosthesis are chosen intraoperatively based on exploratory tympanotomy and available prostheses options. The overarching goal for middle ear surgeries could include development of patient-specific FE models from high-resolution imaging modalities and to investigate the effects of prostheses on hearing.

5.3 Future Directions

Some aspects of related future works are suggested in this section.

5.3.1 Middle-Ear Imaging

Imaging is the first step in developing sample-specific FE models. Further contrast enhancement techniques should be investigated for micro-CT imaging, since it is the common imaging modality in this research area. One example could be taking advantage of multi-energy micro-CT imaging procedures [e.g., (Granton et al., 2008)]. Emerging technologies in biomedical imaging also needed to be tested for middle-ear imaging. Synchrotron radiation is a relatively new technique that has become accessible to biomedical engineers, and shown to have exceptional quality in terms of contrast and resolution [e.g., (Ladak et al., 2016)].

In addition to improving image quality, for sample-specific FE modeling, automated segmentation procedures also need to be developed for middle-ear soft tissues. In the current work, semi-automatic segmentation algorithms were used. These approaches are labour intensive, requiring several days of work (4-5 days in our study) to segment and model each structure. One approach to automating the process would be to use Active Shape Models (ASMs) (Cootes et al., 1995), which have been applied to the cochlea (Schuman et al., 2010). In ASMs, the average shape and modes variation of a structure to be segmented are automatically aligned with and warped to match corresponding structures in an image. The deformed ASM then represents the geometry contained in the new image. The incorporation of *a priori* knowledge in the form of shape information serves as a guide to localizing each specific structure in an image.

5.3.2 Middle-Ear Mechanics

Mechanical properties of the middle-ear soft tissues, especially of the TM, are not completely known. There are both experimental and computational studies that could be pursued in the future. In terms of experimental work, extension of the pressurization-based study to pressure levels above 500 Pa (e.g., to 3 kPa which is used in tympanometry) could assist in developing non-linear models for the human TM. Such models could be used for the cases where large deformations are involved. The pressurization technique could also be used to study the viscoelastic properties of the TM, where time-dependent behavior is investigated. Methodologic variables such as pump speed and pressurization direction (ascending or descending) are important in tympanometry and could be optimized using an FE model that is valid for large pressures and incorporates viscoelastic properties.

With regard to the computational aspect, the optimization technique could be improved. An example is by adding constraints to multi-parameter optimization algorithms. Such constraints are for the purpose of guiding the variation of a parameter, such as Young's modulus, over partitions to avoid sharp changes.

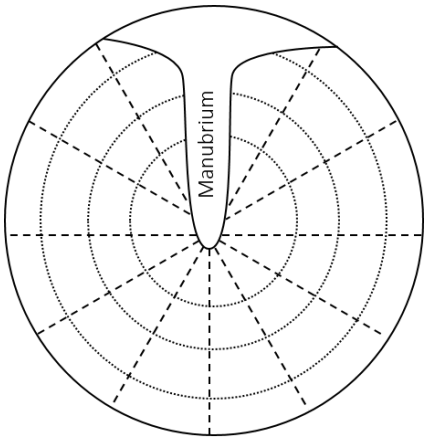

Figure 5-1: Conceptual partitioning for TM.

Also, the partitioning scenarios could be improved. Ideally, partitioning should be based on the ultrastructure of the PT with variation along the radial and circumferential directions with a slight increase in the number of parameters. As shown in the schematic TM diagram in Figure 5-1, by increasing radial and circular lines the number of partitions increases. Consequently, the properties of the TM at the patches would be estimated in a way that the final result be a perfect match of simulated model and experimental data.

5.4 References

Cootes, T., Taylor, C., Cooper, D. & Graham, J. (1995) Active shape models-their training and application. Computer vision and image. 61(1), 38–59.

Granton, P. V., Pollmann, S.I., Ford, N.L., Drangova, M. & Holdsworth, D.W. (2008) Implementation of dual- and triple-energy cone-beam micro-CT for postreconstruction material decomposition. Medical Physics. 35(11), 5030–5042.

Ladak, H.M., Rohani, S.A., Agrawal, S.K. & Zhu, N. (2016) In-Line Phase-Contrast Micro-CT Imaging of The Middle Ear: Improving Soft-Tissue Visualization. In

39th Annual Mid-Winter Meeting of Association for Research on Otolayrngology. San Diego, California, USA.

Schuman, T., Noble, J. & Wright, C. (2010) Anatomic verification of a novel method for precise intrascalar localization of cochlear implant electrodes in adult temporal bones using clinically available computed. The. 120(11), 2277–2283.

Appendix A

Two statistical analysis were performed in Chapter 2. The first test was a Welch's t-test for two sample pools comparing the stained and unstained samples with unequal population variances (n = 24). The second test was a set of 8 paired t-tests comparing each unstained and stained soft tissues of cadaveric heads (n = 3). The significance level of the hypothesis test was 0.05 in both studies ($\alpha = 0.05$).

The statistical powers are calculated using Equations A.1 and A.2.

$$P_{Welch} = \varphi\left(-t_{d'',1-\alpha/2} + \frac{\bar{x}_{stained} - \bar{x}_{unstained}}{\sqrt{\frac{s^2_{stained} + s^2_{unstained}}{n}}}\right) \quad \text{Equation A.1}$$

where:

φ is the cumulative distribution function of the t-test,

d'' is Satterthwaite's method for calculating the degrees of freedom of a t-test with unequal variances,

$\bar{x}$ is the mean of the CNR, and

s is the standard deviation of the CNR.

$$P_{paired\ t-test} = \varphi\left(-t_{n-1,1-\alpha/2} + \frac{\bar{d}}{\sqrt{\frac{s^2_d}{n}}}\right) \quad \text{Equation A.1}$$

where:

φ is the cumulative distribution function of the t-test,

$\bar{d}$ is the mean difference of CNR between stained and unstained soft tissues of the same cadaveric head ($d = CNR_{stained} - CNR_{unstained}$, so $\bar{d} = (d_1 + d_2 + \cdots + d_n)/n$),

s_d is the standard deviation of the CNR calculated from Equation A.3 for n number of matched pairs.

$$s_d = \sqrt{\frac{\left[\sum_{i=1}^{n} d_i^2 - \frac{(\sum_{i=1}^{n} d_i)^2}{n}\right]}{n-1}} \qquad \text{Equation A.3}$$

The results are provided in Table A-1.

Table A-1: Statistical power for Welch's and paired t-tests.

	Soft Tissue	Power
P_{Welch}		0.6455
$P_{paired\ t-test}$	**AML**	0.7408
	IMJ	0.8672
	LML	0.8082
	PIL	0.5411
	SAL	0.5148
	SM	0.6309
	TM	0.9489
	TTM	0.5690

Appendix B

To ensure the cost function used in Chapter 3 is unimodal, its value were calculated for PT Young's modulus in the range of [1 300] MPa. The results are given in Figures B-1 to B-3 for samples TB1, TB2 and TB3, respectively. In all samples, a clearly defined minimum was present.

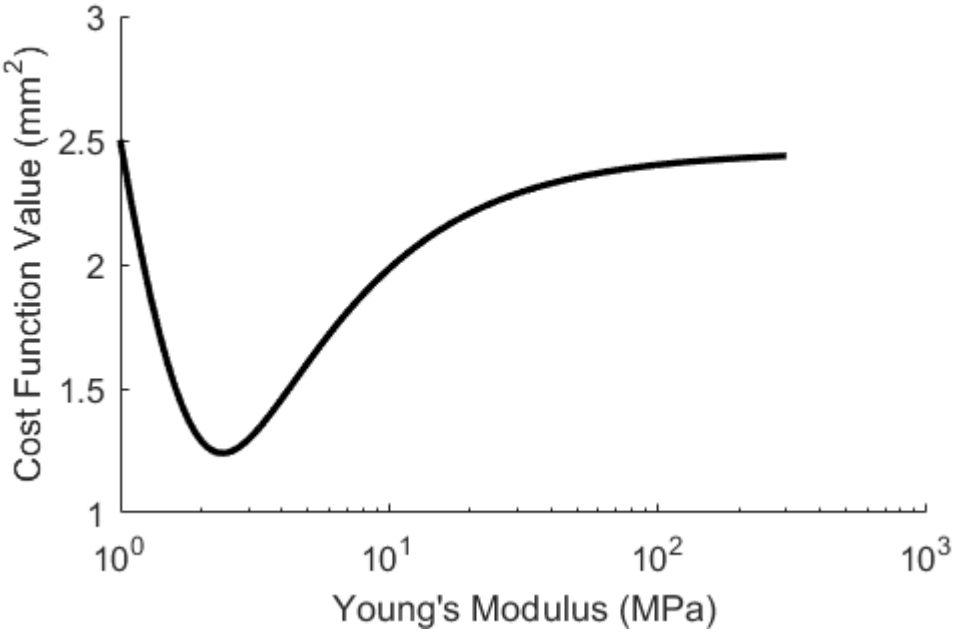

Figure B-1: Graph of cost function as the PT Young's modulus (*E*) is varied for sample TB1.

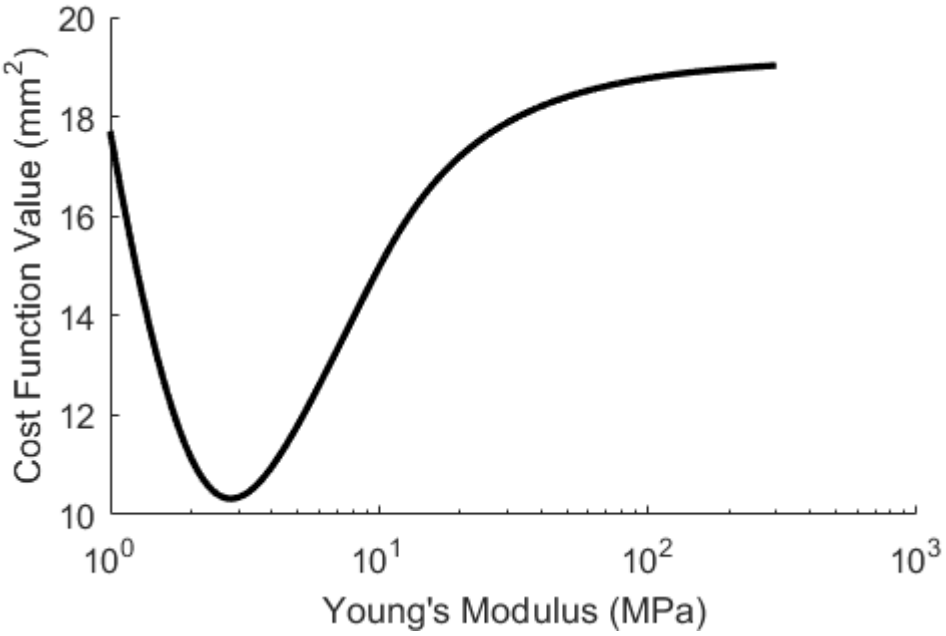

Figure B-2: Graph of cost function as the PT Young's modulus (*E*) is varied for sample TB2.

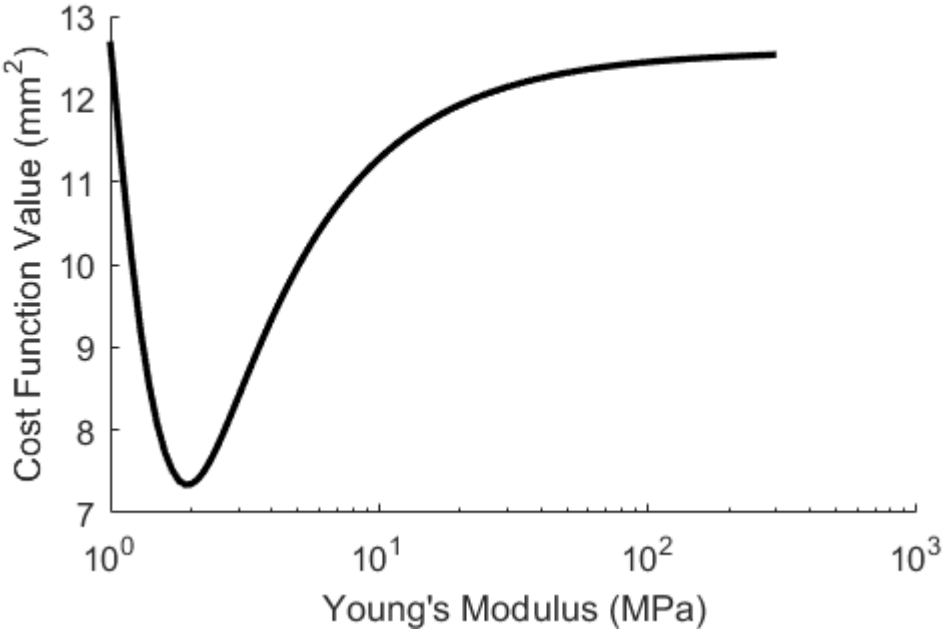

Figure B-3: Graph of cost function as the PT Young's modulus (*E*) is varied for sample TB3.

Appendix C

To ensure the global minimum was achieved in optimizations of Chapter 4, the initialization of the optimization was varied to ensure reaching a global minimum. The results for two cases are reported in this appendix.

Case 1: When the initial simplex of Nelder-Mead optimization for both quadrant-based and ring-based was small and values were around the result of uniform case (e.g., ~2 MPa).

Case 2: When the initial simplex of Nelder-Mead optimization for both quadrant-based and ring-based was rather large. The values were a mixture of values close to the results of uniform case and 10 times of the result of uniform case (e.g., ~20 MPa).

The number of iterations versus cost function values of these two cases are provided in Figures C-1 to C-3.

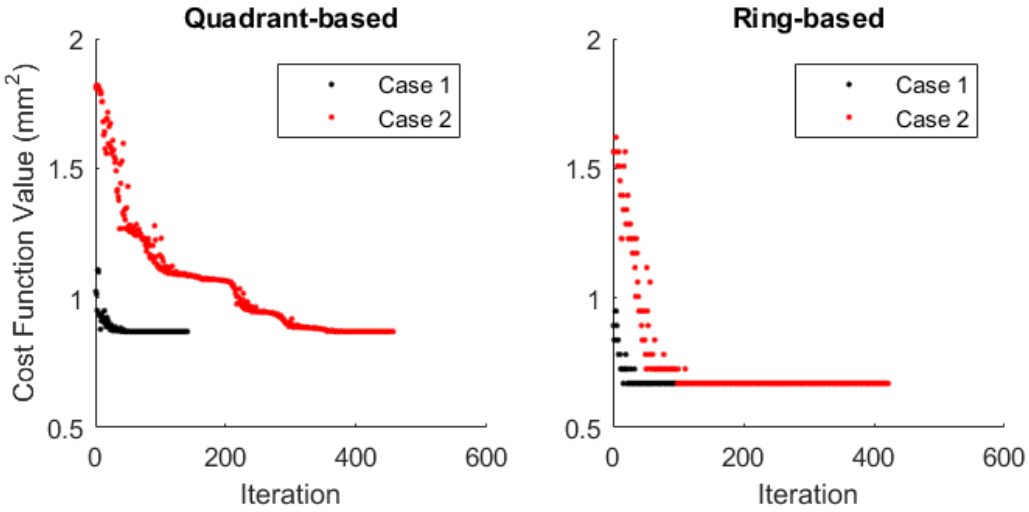

Figure C-1: Graph of cost function for Nelder-Mead optimization iteration of TB1. Two cases of small (Case 1) and relatively large (Case 2) initial simplex were used. In both cases of each type of spatial non-uniformity, the optimization reached a global minimum.

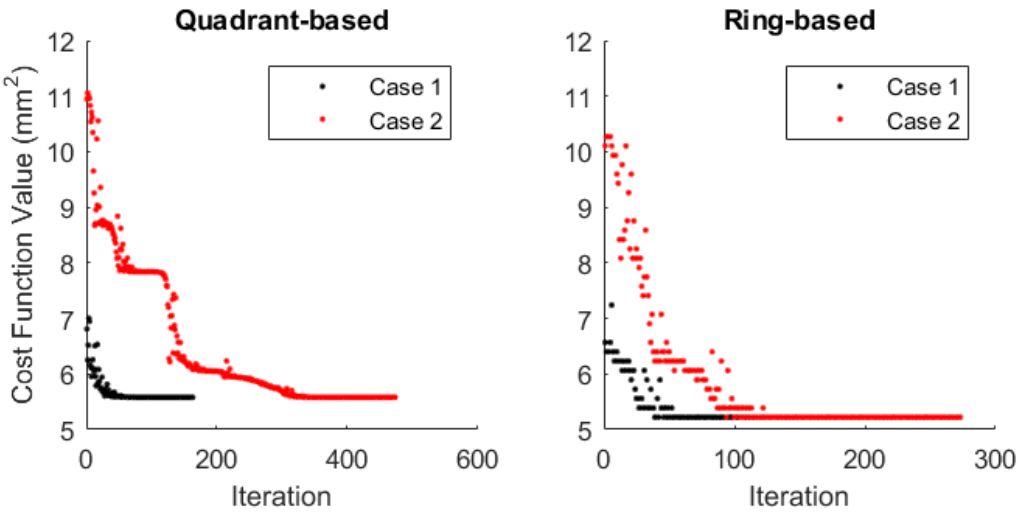

Figure C-2: Graph of cost function for Nelder-Mead optimization iteration of TB2. Two cases of small (Case 1) and relatively large (Case 2) initial simplex were used. In both cases of each type of spatial non-uniformity, the optimization reached a global minimum.

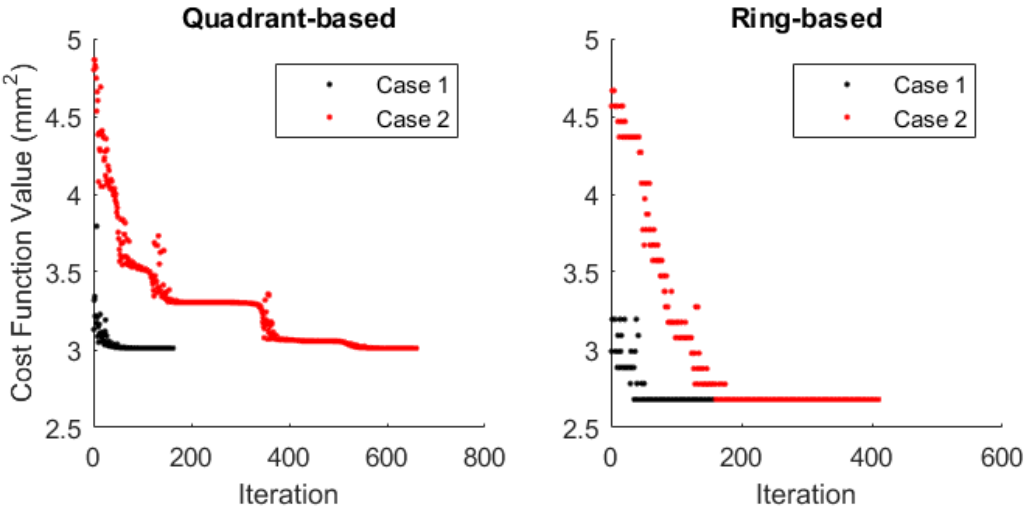

Figure C-3: Graph of cost function for Nelder-Mead optimization iteration of TB3. Two cases of small (Case 1) and relatively large (Case 2) initial simplex were used. In both cases of each type of spatial non-uniformity, the optimization reached a global minimum.

Curriculum Vitae

Education

2011 – Now Ph.D. (Biomedical Engineering)
Western University, London, Canada

2006 – 2011 B.Sc/M.Eng. (Biomedical Engineering)
University of Birmingham, Birmingham, United Kingdom (2009-2011)
Amirkabir University of Technology, Tehran, Iran (2006-2009)

Publications

1- **S.A. Rohani**, S. Ghomashchi, S.K. Agrawal and H.M. Ladak, "Spatial Non-Uniformity in the Young's Modulus of the Human Pars Tensa," *Journal of Biomechanics*, in preparation for submission.

2- M. Elfarnawany, S.R. Alam, **S.A. Rohani**, N. Zhu, S.K. Agrawal and H.M. Ladak, "Micro-CT Versus Synchrotron Radiation Phase Contrast Imaging of Human Cochlea," *Journal of Microscopy*, accepted July 31, 2016 pending revisions (Manuscript ID: JMI-2016-01-01).

3- **S.A. Rohani**, S. Ghomashchi, S.K. Agrawal and H.M. Ladak, "Estimation of the Young's Modulus of the Human Pars Tensa Using In-Situ Pressurization and Inverse Finite-Element Analysis," *Hearing Research* submitted on June 15, 2016, acceptance is pending revisions (Manuscript ID: HEARES_2016_281).

4- **S.A. Rohani**, S. Ghomashchi, J.U. Umoh, D.W. Holdsworth, S.K. Agrawal and H.M. Ladak (2016), "Iodine potassium iodide improves the contrast-to-noise ratio of micro-computed tomography images of the human middle ear," *Journal of Microscopy*, 264(3), 334-338.

5- J.A. Beyea, **S.A. Rohani**, H.M. Ladak and S.K. Agrawal (2013). Laser Doppler Vibrometry measurements of human cadaveric tympanic membrane vibration. *Journal of Otolaryngology-Head and Neck Surgery*, 42(1), 17.

Conference Papers

1- **S.A. Rohani**, S. Ghomashchi, S.K. Agrawal and H.M. Ladak, "Spatial Non-Uniformity in The Young's Modulus of The Human Eardrum," *24th International Congress of Theoretical and Applied Mechanics*, Montréal, QC (Aug 2016).

2- J. Liu, Y. Li; **S.A. Rohani**; S.K. Agrawal, H.M. Ladak and W. Wan, "Fabrication and Acoustic Testing of Electrospun Scaffolds for TM Repair", *39th Annual Mid-Winter Meeting of Association for Research on Otolayrngology*, San Diego, CA (Feb 2016).

3- H.M. Ladak, **S.A. Rohani**, S.K. Agrawal and N. Zhu, "In-Line Phase-Contrast Micro-CT Imaging of The Middle Ear: Improving Soft-Tissue Visualization", *39th Annual Mid-Winter Meeting of Association for Research on Otolayrngology*, San Diego, CA (Feb 2016).

4- **S.A. Rohani**, S. Ghomashchi, S.K. Agrawal and H.M. Ladak, "Estimation of the Young's Modulus of the Human Pars Tensa from In-Situ Pressurization Measurements,"*7th International Symposium on Middle Ear Mechanics in Research and Otology*, Aalborg, Denmark, (Jul 2015).

5- **S.A. Rohani**, J. Liu, J.U. Umoh, D.W. Holdsworth, S.K. Agrawal and H.M. Ladak, "Contrast-Enhanced Micro-CT of the Human Middle Ear," *Canadian Medical and Biological Engineering Conference*, Vancouver, BC (May 2014).

6- E. Salamati, **S.A. Rohani**, S.K. Agrawal, A. Samani and H.M. Ladak, "Estimation of the Orthotropic Elastic Properties of the Eardrum Using a Pressurization Technique," *36th Annual Mid-Winter Meeting of Association for Research on Otolayrngology*, Baltimore, MD (Feb 2013).

Scholarships

- Mitacs Accelerate graduate internship (Sept 2015 – Aug 2016)
- Western Graduate Research Scholarship (WGRS) (Sept 2011 – Aug 2015)
- NSERC CREATE Program in Computer-Assisted Medical Interventions (CAMI) (Sept 2012 – Sept 2014)

Teaching and Supervisory Activities

Aug 2015 – Apr 2016	**Supervisor**, Medical Biophysics 4th Year Project; supervising and training undergraduate student, Western University, London, ON
Jan 2015 – Apr 2015	**Teaching Assistant**, System Modeling and Control MME 3350, Western University, London, ON
Sep 2014 – Dec 2014	**Teaching Assistant**, Materials Selection and Manufacturing Processes MSE 3301, Western University, London, ON
Jan 2014 – Apr 2014	**Teaching Assistant**, Finite-Element Method in Mechanical Engineering MME 3360, Western University, London, ON
Sep 2013 – Dec 2013	**Teaching Assistant**, Materials Selection and Manufacturing Processes MSE 3301, Western University, London, ON
Jan 2013 – Apr 2013	**Teaching Assistant**, Robotics and Manufacturing Automation MME 4452, Western University, London, ON
Feb 2012 – Jun 2012	**Supervisor**, Partners in Experiential Learning (PEL); supervising and training high school student, Western University, London, ON
Jan 2012 – Apr 2012	**Teaching Assistant**, Robotics and Manufacturing Automation MME 4452, Western University, London, ON